Technische Universität München

Physik Department

MPQ

# A Quantum-Logic Gate between Optical Photons Based on Cavity Rydberg Blockade

**Thomas Eugen Stolz**

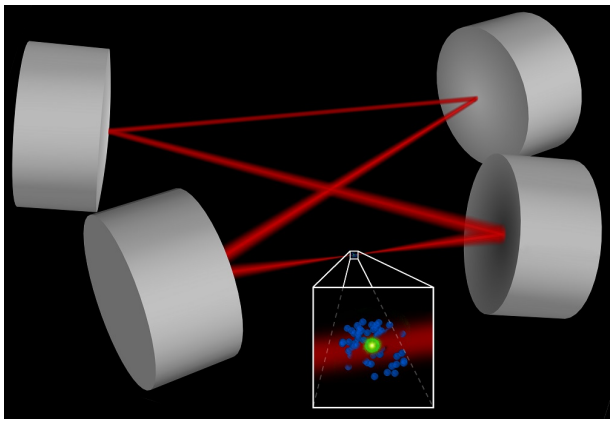

**Dissertation**

Max-Planck-Institut für Quantenoptik, Garching
and Physik Department, Technische Universität München

October 2023

**Cover illustration:** The title cover displays an artist's view of the coupled atom-cavity system.

Technische Universität München
TUM School of Natural Sciences

# A Quantum-Logic Gate between Optical Photons Based on Cavity Rydberg Blockade

Thomas Eugen Stolz

Vollständiger Abdruck der von der TUM School of Natural Sciences der Technischen Universität München zur Erlangung eines

**Doktors der Naturwissenschaften (Dr. rer. nat.)**

genehmigten Dissertation.

Vorsitz: Prof. Dr. Michael Knap

Prüfer*innen der Dissertation:

1. Hon.-Prof. Dr. Gerhard Rempe
2. Prof. Dr. Peter Fierlinger

Die Dissertation wurde am 26.04.2023 bei der Technischen Universität München eingereicht und durch die TUM School of Natural Sciences am 06.10.2023 angenommen.

# Abstract

This thesis reports on the experimental realization of a quantum-logic gate between optical qubits. The physical mechanism of this gate relies on electromagnetically induced transparency and Rydberg blockade in an ultracold ensemble of $^{87}$Rb atoms, which are trapped inside a moderate-finesse bow-tie resonator. For the first time, the efficiency achieved with a quantum nonlinear system surpasses the state-of-the-art in linear optical quantum computing.

The qubits are implemented in the polarization degrees of freedom of individual photons. A spatial dual-rail setup directs these photons either onto the resonator or into a bypass rail and subsequently recombines the two paths. The temporal gate protocol consists of three steps. First, a control photon is reversibly stored inside the atomic ensemble as a Rydberg excitation. In the second step, a target photon is reflected from the resonator during the storage time. If a control excitation is present, Rydberg blockade induces a conditional $\pi$ phase shift. In the third step, the control photon is retrieved.

This gate is characterized by an average efficiency of 41.7(5)% and a postselected process fidelity of 81(2)%. Polarization-entangled Bell states are produced with postselected fidelities between 78(3)% and 82(2)%. An extension of the gate to multiple target photons is demonstrated, resulting in the production of Greenberger-Horne-Zeilinger states of 3, 4, and 5 photons with fidelities of 62.3(4)%, 54.6(1.4)%, and 54.8(5.3)%, respectively.

# Zusammenfassung

Im Rahmen dieser Arbeit wurde ein Quantenlogikgatter zwischen optischen Qubits experimentell realisiert. Der physikalische Mechanismus dieses Gatters beruht auf elektromagnetisch induzierter Transparenz und Rydberg-Blockade in einem ultrakalten Ensemble von $^{87}$Rb-Atomen, die in einem Bow-Tie-Resonator mit moderater Finesse gefangen sind. Zum ersten Mal übertrifft die mit einem nichtlinearen Quantensystem erreichte Effizienz den Stand der Technik im linearen, optischen Quantencomputing.

Die Qubits sind in den Polarisationsfreiheitsgraden von Photonen implementiert. Ein räumlicher Dual-Rail-Aufbau lenkt diese Photonen entweder auf den Resonator oder in einen Bypass-Pfad und rekombiniert anschließend die beiden Pfade. Der zeitliche Ablauf des Gatters besteht aus drei Schritten. Zunächst wird ein Control-Photon als Rydberg-Anregung reversibel im atomaren Ensemble abgespeichert. Im zweiten Schritt wird während der Speicherzeit ein Target-Photon am Resonator reflektiert. Wenn eine Control-Anregung vorhanden ist, führt Rydberg-Blockade zu einer $\pi$-Phasenverschiebung. Im dritten Schritt wird das Control-Photon wieder ausgelesen.

Das Gatter zeichnet sich durch eine durchschnittliche Effizienz von 41.7(5)% und eine postselektierte Prozessfidelity von 81(2)% aus. Polarisationsverschränkte Bell-Zustände werden mit einer postselektierten Fidelity zwischen 78(3)% und 82(2)% erzeugt. Eine Erweiterung des Schemas auf mehrere Target-Photonen ermöglicht die Herstellung von Greenberger-Horne-Zeilinger-Zuständen mit 3, 4 und 5 Photonen bei Fidelities von 62.3(4)%, 54.6(1.4)% und 54.8(5.3)%.

# Contents

# Chapter 1

# Introduction

Optical qubits are attractive information carriers for future quantum technologies because they uniquely combine information transfer and processing capabilities. Optical fiber technology makes photons well suited for transmitting quantum information in a future quantum internet [76, 165] or between processing units of a distributed quantum computer [17, 19, 124]. Even the intriguing prospect of an all-optical quantum computer [107] has seen remarkable progress in recent years, culminating in the demonstration of quantum computational advantage for a specific mathematical problem in the framework of Gaussian boson sampling [175]. However, performing arbitrary computations, such as Shor's algorithm [140], requires universal quantum computing schemes [104].

A popular such scheme is the circuit model of quantum computation, in which a sequence of quantum-logic gates is applied to a number of quantum bits (qubits). Mathematically, a gate is represented by a unitary transform that is applied to the quantum state of the system. An arbitrary computation becomes possible once a universal gate set is available. One example of such a universal gate set consists of single-qubit unitaries along with a two-qubit controlled NOT (CNOT) gate [104].

According to DiVincenzo's criteria [24], a central requirement for a practical implementation is the ability to apply these unitary transforms in a well controlled way. If optical photons are used as qubits, constructing single-qubit unitaries is relatively simple. For example, when choosing a polarization encoding, any single-qubit unitary can be realized as a sequence of at most three waveplates [142]. In contrast, implementing optical CNOT gates is a significant challenge. This is because if one intends to follow the obvious idea of implementing the gate based on an optical nonlinearity, then this nonlinearity must be large at the single-photon level. Over the past 20 years, several strategies have been pursued toward optical CNOT gates but apart from linear optical quantum computing (LOQC) schemes, which are inherently probabilistic, only two proof-of-principle demonstrations using a quantum nonlinear system have been reported. Moreover, the low efficiency of all previous experimental implementations is still a major issue in the field of optical quantum information processing. In the following Secs. 1.1 – 1.3, the quest for efficient optical CNOT gates is outlined. As an aside, it is noted that there has also been progress with photon-photon gates in the microwave domain recently, see Ref. [122].

In spite of these challenges, optical CNOT gates are extremely attractive devices. Not only are they crucial building blocks of all-optical quantum computers. They could also boost the efficiency of optical Bell-state detection, which has a fundamental efficiency limit of 50% if only linear optical components are used [14]. A high-efficiency Bell-state

analyzer would be useful for quantum repeaters [51], which will probably be required to realize long-distance quantum communication [11] and a quantum internet [76, 165].

## 1.1 Linear Optical Quantum Computing

A well established approach toward optical CNOT gates is LOQC. Here, effective nonlinearities are induced by measurements. In 2003, the authors of Ref. [106] demonstrated the first two-photon quantum gate with this approach. In their experiment, two photonic input qubits are sent into a linear optical setup, which consists only of beam splitters and wave plates. This setup has four possible exit points, two of which are the outputs of the gate. If one photon is detected at each of the two output ports, the gate was successful and a CNOT operation is obtained. Ideally, this happens with a probability of 1/9. Although Ref. [106] does not give a number for the experimentally achieved efficiency, we may speculate that it came close to the theoretical limit, because the few components required for the optical setup are commercially available at good quality and low loss. It was later shown theoretically that 1/9 is, in fact, a rigorous upper bound for the efficiency of such a scheme [74], if only linear optics and postselection are used.

Despite its elegance and simplicity, this scheme is not immediately useful for quantum computation. If a quantum circuit is constructed by simply cascading probabilistic LOQC gates, the success probability of the circuit becomes exponentially small with the number of gates. Hence, an exponential amount of time or resources would be required, eradicating any potential speed-up compared to a classical device. This issue was solved by the seminal work of Knill, Laflamme, and Milburn in 2001 [78], which is known as the KLM protocol. It theoretically shows how scalable LOQC can be achieved by combining several key ideas. The first idea is to generate entangled states of several photons by repeatedly attempting probabilistic gates until success. In the KLM scheme, such states are prepared as auxiliary resource states and stored in a quantum memory until they are needed for the computation. The second idea is known as the teleportation trick [49], which is to construct a CNOT gate by using Bell measurements, conditional single-qubit operations, and an entangled resource state prepared as described above. This leaves the problem that deterministic Bell measurements are impossible using just linear optics [14, 93]. However, KLM came up with a teleportation scheme that allows for an arbitrarily small error probability when a sufficiently large resource state, prepared as described above, is used. In addition to purely linear optical components, this technique requires photon number resolving detectors and classical feedforward, i.e. conditional switching of components in the optical circuit. Finally, the KLM scheme proposes to alleviate the small remaining failure probability by using error correcting codes, which ensure the scalability of the protocol.

Over the course of the years, improvements to the KLM scheme have been theoretically developed which decrease the resource requirements to some extent [55, 79, 107, 117]. Some of these fall into the category of measurement based quantum computation and dispense entirely with the use of CNOT gates [13, 103, 118, 172]. Instead, the experimental challenge is shifted to the preparation of a large entangled cluster state which is required as an input for the computation. Cluster states of up to 12 polarization-entangled photons have been realized so far [66, 90, 147].

While the KLM protocol shows *theoretically* that high efficiency CNOT gates can be built using linear optics, this turns out to be very difficult *in practice*. Although some advanced CNOT gate schemes have been experimentally demonstrated over the last 20 years [86], their efficiency stayed below the threshold of about 11% originally achieved in Ref. [106]. In contrast to the efficiency, the postselected process fidelity of a CNOT gate achieved in LOQC has been improved over the course of the years, starting from 87% in Ref. [105] to e.g. 98.85% in Ref. [115]. A likely explanation why it is difficult to improve the efficiency are the resource requirements. For example, implementing a single CNOT gate with a success probability above 95% requires on the order of $10^4$ physical operations in the KLM protocol [55, 79]. Along with this, a large number of ancillary single-photon input states are needed, which have to be generated using high-quality single-photon sources. In front of this backdrop, Ref. [79] concluded that "the physical resources for the original KLM protocol, albeit scalable, are daunting. For linear optical quantum computing to become a viable technology, we need more efficient quantum gates."

Current research pursues this goal with essentially two approaches. On one hand, integrated photonics [75, 112] may render the resource requirements of probabilistic LOQC protocols more manageable. On the other hand, advancing quantum nonlinear systems may lead to optical CNOT gates that are not inherently probabilistic. For the remainder of this introduction, we focus on the latter approach, which has seen remarkable progress in recent years.

## 1.2 Quantum-Nonlinear Systems

As Maxwell's equations in vacuum are linear, photons do not interact with each other in vacuum.[1] A nonlinear medium offers a potential solution to this issue. Already in the late 1980s, Refs. [97, 169] proposed to implement logic gates between photons using cross-phase modulation in a nonlinear crystal. Based on the Kerr effect, it was imagined that the presence of a single control photon induces a refractive index change in the crystal that leads to a phase shift for another photon. Such a *conditional phase shift* may be regarded as originating from an effective photon-photon interaction, which is mediated by light-matter coupling. By placing the crystal inside a spatial dual-rail setup [79], a controlled-phase gate [104] between two polarization qubits can be realized. If the phase shift is $\pi$, a controlled-$\pi$-phase (CPHASE) gate is obtained, which turns into a CNOT gate when combined with appropriate single-qubit unitaries. Unfortunately, typical Kerr nonlinearities are tiny at the single photon-level [79]. In optical fibers, conditional phase shifts on the order of $10^{-7}$ rad per photon were reported [95]. Ref. [107] concluded in 2007 that "no known or foreseen material has an optical nonlinearity strong enough to implement this conditional phase shift".

This perspective has changed dramatically. Over the past 20 years, several *quantum-nonlinear systems* have been developed, which can produce large conditional phase shifts

[1] For completeness, it bears mentioning that quantum electrodynamics predicts an interaction between photons when the photon energy is large enough such that spontaneous formation of electron-positron pairs becomes significant. This was first recognized by Euler and Kockel [30]. However, this effect is far too weak for optical photons to make use of it under realistic conditions.

at the single photon level. Already in 1995, Ref. [157] achieved a conditional phase shift of $\pi/10$ per photon using the nonlinearity of a single atom enhanced by a high-finesse cavity. Conditional phase shifts of a similar size have been observed with a single quantum dot coupled to a photonic crystal nanocavity in 2008 [40]. Using a single atom coupled to a fiber-based whispering gallery mode resonator, a conditional $\pi$ phase shift was demonstrated in 2014 [161]. A different strategy is to use electromagnetically induced transparency (EIT) [35] in an ultracold atomic gas in free-space. With this technique, measured single-photon phase shifts have reached roughly $10^{-5}$ rad [31, 89, 138]. Extensions to a double-$\Lambda$ system [88] or to a resonator-enhanced scheme [9] achieved conditional phase shifts per photon of $\pi/8$ and $\pi/3$, respectively. Combining EIT with atomic Rydberg states, conditional phase shifts up to $\pi$ [152] have been demonstrated in our laboratory, as highlighted in the next section.

A usually unwanted side effect in all the above systems is the nonzero photon-loss probability. For certain parameters, the presence or absence of a single photon may even *change* the loss probability for another photon. We refer to this difference in the loss probability as *conditional loss*. This effect may be utilized to realize a single-photon switch, which has been demonstrated with an ultracold atomic ensemble in a high-finesse cavity [16], a single atom coupled to a silica microsphere resonator [139] and also with a single atom coupled to a photonic crystal nanocavity [153]. The same can be achieved using Rydberg EIT, see Sec. 1.3.

If a system exhibits conditional loss, this can be converted into a conditional $\pi$ phase shift by placing the system inside a one-sided optical resonator. This was recognized by Hofmann [60] as well as Duan and Kimble [26], who proposed to implement optical CNOT gates based on this idea. As an experimental platform, they envisioned a single atom inside a high-finesse optical resonator. Once full control over the atom is attained, such a system becomes a toolbox for the preparation and manipulation of nonclassical states of light and matter, opening up a plethora of possibilities for quantum information processing and quantum networks [121]. These prospects have sparked tremendous experimental progress. As a consequence, these systems have reached a level of maturity that resulted in the first implementation of an optical CNOT gate based on a quantum-nonlinear system in 2016 [53].

In this implementation, the photon-photon gate is decomposed into two atom-photon gates, single-qubit operations, a projective measurement, and classical feedback conditioned on the measurement outcome. Two photons are successively reflected from a high-finesse Fabry-Pérot cavity, state rotations are performed on the atom, and finally a conditional state rotation is applied to the first photon, depending on the outcome of a state measurement on the atom. Hypothetically, there is no fundamental limit to the efficiency of this scheme. However, the experimentally achieved value of $< 5\%$ was lower than the LOQC record of 11%. This is explained by several technical issues. First, the empty high-finesse cavity reflects only about 70% of the photons due to mirror imperfections. A similar reflection probability is obtained, when an atom is coupled to the cavity because the achievable cooperativity in this cavity is limited. Finally, the scheme requires storing the first photon for several microseconds until the atomic state detection is completed. A long fiber with about 40% transmission was used as a storage device, through which

both photons had to pass. These issues might be overcome in the future by technical improvements.

Another CNOT gate based on a quantum-nonlinear system was demonstrated in our laboratory in 2019 based on Rydberg EIT with an ultracold atomic ensemble in free space [151]. This result is one of many recent highlights from the field of Rydberg quantum photonics, which is the topic of the next section.

## 1.3 Rydberg Quantum Photonics

The field of Rydberg quantum photonics is in many ways inspired by the possibility to implement quantum gates between neutral atoms using Rydberg interactions, which was proposed in Ref. [67] and first demonstrated in 2010 [65, 167]. This Rydberg-atom based quantum computing platform has attracted growing interest in recent years because it promises to combine high-fidelity quantum gates [85] with the flexibility and scalability provided by individual atoms trapped in reconfigurable tweezer arrays [6, 29] or in optical lattices [130]. Two review articles about this platform can be found in Refs. [1, 128].

The strong and long-range interactions between Rydberg atoms can be mapped onto optical photons by using Rydberg EIT in an ultracold atomic ensemble, as first proposed in Ref. [39]. When photons enter such a medium, they turn into quasi-particles termed Rydberg polaritons [47] which are composed of a propagating photon and an atomic Rydberg excitation. Hence, they inherit the strong and long-range interactions between atomic Rydberg states. This provides a fascinating way to observe interacting photons. These interactions can be tailored, resulting in attractive [33], repulsive [15] or dissipative [111] character. At suitable parameters, interesting many-particle states of light are predicted to emerge [108].

A central concept in this field is Rydberg blockade, which was first observed in Ref. [155]. Once a Rydberg excitation is created in an atomic ensemble, the strong and long-range Rydberg-Rydberg interaction inhibits the formation of a second Rydberg excitation in its vicinity. In resonant Rydberg EIT this leads to a reduced transparency at high input photon rates [114]. The range of this blockade effect is characterized by the Rydberg blockade radius, which is typically around 10 µm. An interesting regime of operation emerges when the size of the atomic ensemble becomes smaller than the blockade radius. In this situation, the atomic ensemble becomes an effective two-level system because only one Rydberg excitation can be created. Such a system is called a superatom [128].

The first experiments on Rydberg EIT were performed with a single light field passing through the atomic ensemble. However, the versatility of this platform can be greatly enhanced by employing techniques for the storage and retrieval of light [34, 48]. For instance, strong antibunching of the retrieved light has been observed when using high lying atomic Rydberg states for storage [27]. Sending a second light field through the ensemble during the dark time between storage and retrieval, large conditional loss [7, 45, 150] and conditional phase shifts of $\pi/2$ [148] and $\pi$ [152, 160] have been realized.

Over the past 20 years, there have been many proposal for optical two-qubit gates using Rydberg EIT in free space [39, 47, 56, 73, 82, 100, 102, 109]. Recently, such a scheme was finally realized in our laboratory [151]. The average efficiency achieved in this experiment

was $< 3\%$. As with the single atom in a high-finesse resonator, this efficiency is lower than the LOQC record of 11%. The dominant limitation in this experiment originates from dephasing induced by interactions between Rydberg and ground-state atoms [7, 98, 133] at the required high atomic density.

## 1.4 This Work

This work reports on the experimental demonstration of a CNOT gate between optical photons based on a Rydberg superatom inside a moderate-finesse bow-tie resonator. As proposed in Refs. [22, 54, 101, 162], the cavity makes it possible to harvest the nonlinearity of Rydberg EIT more efficiently. The resulting cavity Rydberg EIT system combines the atom-cavity approach and the Rydberg EIT approach in an advantageous way. Thanks to the cavity enhancement, high atomic densities which are detrimental to Rydberg coherence are not required. Thanks to the collective atomic enhancement, a moderate-finesse cavity is sufficient and some technical difficulties associated with high-finesse cavities can be avoided.

The protocol of this experiment consists of three steps. In the first step, a control photon is transferred into a collective Rydberg excitation of the superatom using an EIT-based storage protocol. In the second step, a target photon is reflected from the cavity. In the third step, the control photon is retrieved. Overall, this realizes a conditional $\pi$ phase shift. A spatial dual-rail scheme is used to obtain a CPHASE gate for polarization qubits based on this mechanism. It is shown that this strategy indeed leads to considerably higher efficiency than all previous implementations of optical CNOT gates.

Our two-photon CNOT gate has a straightforward generalization to a CNOT gate with multiple target qubits [104]. Based on this generalization, we create Greenberger-Horne-Zeilinger (GHZ) states of presently up to 5 photons. This demonstrates that the drastically improved performance of the gate makes a different class of experiments possible, which with previous optical gates could not have been performed in a realistic data acquisition time. Our work does not set a new record for the photon number in entangled many-photon states. In our experiment, this number is mainly limited by the unfavorable photon statistics of the coherent input states that we use to characterize the gate. If, for instance, a deterministic single-photon source was used instead, it should be possible to generate much larger entangled states. In front of this backdrop, it is remarkable that among the previous experiments [136, 147, 164, 170, 171, 174], which produced entangled states of more than 4 photons, there is not a single one which relies on a CNOT gate for photons. They all employed alternative techniques. Ref. [66] combined a probabilistic entangling gate with a single-photon source but still did not achieve entanglement of more than 4 photons. In this sense, our work does set a new record.

This work is organized as follows. Chapter 2 presents an extensive theory model of the system, which is used to identify an optimal parameter regime for the gate. Based on these insights, a new experimental setup was designed which is described in chapter 3. This new design required implementing various techniques for cooling and trapping atoms inside the optical resonator, which is the subject of chapter 4. Characterization measurements of the cavity Rydberg EIT system are shown in chapter 5 and set the

stage for chapter 6, which presents results on the optical CNOT gate. This includes the preparation of entangled Bell states and an extensive characterization of the gate operation using quantum process tomography. Finally, we prepare entangled GHZ states of several photons as a first demonstration of the improved capabilities provided by our efficient scheme. Chapter 7 discusses potential future directions and possibilities for further improving the gate.

# Chapter 2

# Theory

This chapter presents theoretical concepts which are particularly relevant for this work. The optical resonator, Rydberg states, and electromagnetically induced transparency (EIT) constitute the basic ingredients of the experiment and are discussed in the first three sections 2.1, 2.2, and 2.3. Combining these concepts leads to a variety of interesting physical phenomena. Using methods described in Sec. 2.4, an incoming photon can be stored reversibly inside the resonator. While a photon is stored, cavity Rydberg blockade is obtained for subsequent photons as described in Sec. 2.5. Based on this effect, a photon-photon quantum gate can be realized by choosing suitable experimental parameters and by using a spatial dual rail scheme, see Sec. 2.6. Finally, section 2.7 deals with the nontrivial question of how to optimize the gate performance in the presence of experimental imperfections.

Most of chapter 2 summarizes models and results from the literature [8, 22, 36, 43, 54, 141]. However, parts of Secs. 2.5 and 2.7 are original work developed in the course of this thesis.

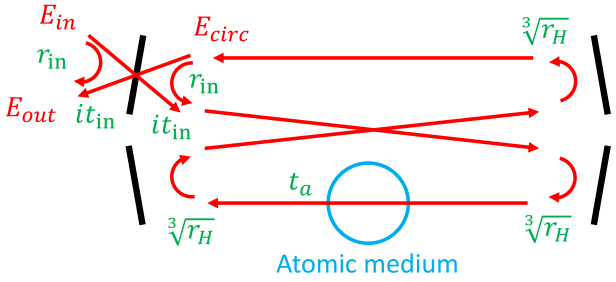


**Figure 2.1:** Model of the optical resonator. The outgoing field amplitude $E_{\mathrm{out}}$ results from interference at the I/O coupler between the reflected incoming field $E_{\mathrm{in}}$ and the transmitted intracavity field $E_{\mathrm{circ}}$. Propagation, transmission and reflection of light fields are indicated by red arrows and result in a change of the field amplitude and phase. This is accounted for by multiplying field amplitudes with complex coefficients (green). The transmission through the atomic medium (blue) is given by the coefficient $t_a$.

## 2.1 Optical Resonator

We consider an optical ring resonator inside which we place an atomic medium. Figure 2.1 shows an example configuration with four mirrors. A classical, monochromatic signal light field $\boldsymbol{E}_{\mathbf{in}} = \frac{1}{2}E_{\mathrm{in}}\boldsymbol{\epsilon}\exp(-i\omega t) + \mathrm{c.c.}$ with angular frequency $\omega$, complex amplitude $E_{\mathrm{in}}$, time $t$, and complex polarization vector $\boldsymbol{\epsilon}$ is reflected from the input/output (I/O) coupling mirror of the resonator. We assume that all optical elements are linear and conserve the light polarization vector $\boldsymbol{\epsilon}$. Moreover, we assume perfect transverse mode matching and a lossless I/O coupler.

The amplitudes of the outgoing light field $E_{\mathrm{out}}$ and the light field circulating inside the resonator $E_{\mathrm{circ}}$ can be calculated from $E_{\mathrm{in}}$ in a straightforward fashion using methods from classical optics, cf. Ref. [141]. In essence, light field amplitudes are propagated between points in space by multiplication with complex numbers.

The intracavity field is

$$E_{\mathrm{circ}} = \frac{it_{\mathrm{in}}r_H t_a e^{i\phi}}{1 - r_{\mathrm{in}}r_H t_a e^{i\phi}} E_{\mathrm{in}} \tag{2.1}$$

and the outgoing field is[1] $E_{\mathrm{out}} = -\mathcal{R}E_{\mathrm{in}}$ with the cavity reflection coefficient

$$\mathcal{R} = \frac{t_a r_H e^{i\phi} - r_{\mathrm{in}}}{1 - r_{\mathrm{in}}r_H t_a e^{i\phi}}. \tag{2.2}$$

Here, $r_{\mathrm{in}}$ ($it_{\mathrm{in}}$) is the complex coefficient for reflection from (transmission through) the I/O coupler, $r_H$ is the product of the complex coefficients for reflection from all highly reflecting (HR) cavity mirrors, and $t_a$ is the complex coefficient for the transmission of the electric field amplitude through the atomic medium, relative to free space propagation. Without loss of generality, we use a phase convention with $r_{\mathrm{in}} > 0$, $t_{\mathrm{in}} > 0$ and $r_H > 0$, such that the phase of $\mathcal{R}$ matches Refs. [22, 46, 54]. A lossless I/O coupler fulfills $r_{\mathrm{in}}^2 + t_{\mathrm{in}}^2 = 1$.

The evolution of the field amplitude in one cavity round trip is described by $r_{\mathrm{in}}r_H t_a e^{i\phi}$ with the empty-cavity round-trip phase $\phi$ which has the property

$$e^{i\phi} = \exp\left(2\pi i \frac{\Delta_c}{\Delta\omega_{\mathrm{ax}}}\right). \tag{2.3}$$

Here, $\Delta_c = \omega - \omega_c$ denotes the detuning of the signal light from a given empty-cavity resonance with frequency $\omega_c$. Two neighboring axial empty-cavity modes are separated in $\omega$ by the axial mode spacing $\Delta\omega_{\mathrm{ax}} = 2\pi/t_{\mathrm{rt}}$, where $t_{\mathrm{rt}} = L_c/c$ is the round-trip time, where $c$ is the vacuum speed of light, and where $L_c$ is the round-trip cavity length.

We introduce the loss-rate coefficients $\kappa_{\mathrm{in}}$, $\kappa_H$, and $\kappa = \kappa_{\mathrm{in}} + \kappa_H$ for the intracavity field amplitude caused by $r_{\mathrm{in}} = \exp(-\kappa_{\mathrm{in}}t_{\mathrm{rt}})$, $r_H = \exp(-\kappa_H t_{\mathrm{rt}})$, and $r_{\mathrm{in}}r_H = \exp(-\kappa t_{\mathrm{rt}})$. We abbreviate

$$\mathcal{F}_{\mathrm{in}} = \frac{\Delta\omega_{\mathrm{ax}}}{2\kappa_{\mathrm{in}}} = \frac{-\pi}{\ln(r_{\mathrm{in}})}, \tag{2.4}$$

$$\mathcal{F}_H = \frac{\Delta\omega_{\mathrm{ax}}}{2\kappa_H} = \frac{-\pi}{\ln(r_H)}, \tag{2.5}$$

[1] The minus sign is a matter of convention. For instance, moving the reference plane in space at which $E_{\mathrm{out}}$ is defined by half a wavelength would alter the sign of $E_{\mathrm{out}}$.

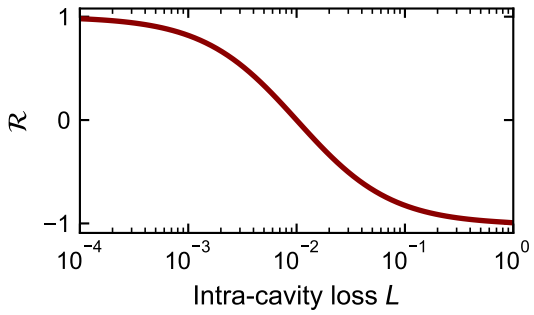


**Figure 2.2:** Resonant cavity reflectivity $\mathcal{R}$ as a function of intra-cavity loss $L$ for $r_{\mathrm{in}} = \sqrt{0.99}$, $t_a = \sqrt{1-L}$ and $r_H = 1$. The sign of $\mathcal{R}$ flips at the impedance-matching point $t_a = r_{\mathrm{in}}$. $|\mathcal{R}|$ approaches unity only if losses are either very large or very small.

$$\mathcal{F} = \frac{\Delta\omega_{\mathrm{ax}}}{2\kappa} = \frac{-\pi}{\ln(r_{\mathrm{in}} r_H)}. \tag{2.6}$$

Hence, in the absence of atoms, an intracavity photon has a branching ratio of

$$\beta = \frac{\kappa_{\mathrm{in}}}{\kappa_{\mathrm{in}} + \kappa_H} = \frac{\mathcal{F}_H}{\mathcal{F}_H + \mathcal{F}_{\mathrm{in}}} \tag{2.7}$$

for decay through the I/O coupler as opposed to loss from an imperfect HR mirror. Assuming $\mathcal{F} \gg 1$, the half width at half maximum (HWHM) linewidth of the empty-cavity resonance in the intracavity field energy as a function of $\omega$ is $\kappa = \kappa_{\mathrm{in}}/\beta$. The empty-cavity finesse is $\mathcal{F} = \beta\mathcal{F}_{\mathrm{in}}$.

A key idea of this work is that by modifying $t_a$ the cavity reflectivity $\mathcal{R}$ can be changed. This idea is also illustrated in Fig. 2.2. We temporarily assume $\Delta_c = 0$. For a critical value $t_a = r_{\mathrm{in}}/r_H$ we find $\mathcal{R} = 0$. Smaller (larger) values of $t_a$ yield an undercoupled (overcoupled) situation with $\mathcal{R} < 0$ ($\mathcal{R} > 0$). Hence, switching from an overcoupled to an undercoupled cavity leads to a $\pi$ phase difference of the outgoing signal light field. This idea was used in Refs. [26, 60] to propose phase switching using the quantum state of a single-atom in a cavity.

## 2.2 Rydberg States

### 2.2.1 General Properties

A Rydberg state is an atomic state in which one electron is promoted to a large principal quantum number $n$. The wave function of the Rydberg electron has an enormous size compared to the atomic ground state. Here, we consider Rydberg states of the single valence electron of $^{87}$Rb which has a nuclear spin $I = \frac{3}{2}$. The core only weakly influences the Rydberg electron, resulting in a small hyperfine splitting of less than 0.5 MHz for $S$ states with $n > 45$ [87] and a hydrogen-like level structure. We therefore characterize

the Rydberg states by $n$, $\ell$, $s = \frac{1}{2}$, $j$, and $m_j$, where $\ell$ is the orbital angular momentum quantum number, $s$ is the electron spin quantum number, and $j$ and $m_j$ are fine structure quantum numbers. The binding energy of Rydberg states can be calculated using [8, 41]

$$E_{n,\ell,j} = \frac{-hcR_y}{(n - \delta_{n,\ell,j})^2} \tag{2.8}$$

where $h$ is the Planck constant, $c$ is the speed of light, $R_y = R_\infty M/(M + m_e)$, $R_\infty = 10\,973\,731.6\,\mathrm{m}^{-1}$, M is the mass of the atomic core, $m_e$ is the mass of the electron, and $\delta_{n,\ell,j}$ is the quantum defect. Properties of Rydberg states often scale with a power law of the effective principal quantum number $n^* = n - \delta_{n,\ell,j}$ [8].

Calculating approximate Rydberg wave functions for not too small radii is possible with the method explained in Refs. [8, 10]. An implementation of this method is, for instance, found in the open-source software package ARC (Alkali Rydberg Calculator, version 3.0.0) [125]. From these wave functions, radial parts of the electric dipole matrix elements between Rydberg states can be obtained.

Due to the weak binding of the electron, Rydberg atoms are easily polarized by an external electric field $\boldsymbol{E}$. For small electric fields, the energy shift compared to zero field can be expressed as

$$\Delta E_{\mathrm{Stark}} = -\frac{1}{2}\alpha_0 \boldsymbol{E}^2 \tag{2.9}$$

with the static electric polarizability $\alpha_0$ which depends on the quantum numbers of the Rydberg state. A practical method for determining Stark shifts of Rydberg states by diagonalizing the Stark Hamiltonian within a subspace of the Rydberg manifold is described in Ref. [176]. Again, we use the implementation of this method in Ref. [125], which determines $\alpha_0$ from a quadratic fit to the energy shift as a function of the electric field.

### 2.2.2 Electrically Tuned Förster Resonance

In this section, the concept of an electrically tuned Förster resonance is briefly introduced and important consequences of our choice of quantum numbers are explained. Further details and a more general overview of Förster resonances in rubidium can be found in Refs. [43, 44, 110], which pioneered studies of an electrically tuned Förster resonance at these quantum numbers experimentally.

We consider two Rydberg atoms at an internuclear distance $R$. The electrostatic interaction between the two Rydberg atoms is to leading order described by a dipole-dipole coupling [8, 120, 163][2]

$$V_{dd}(R) = \frac{1}{4\pi\epsilon_0}\frac{\boldsymbol{d}_1 \cdot \boldsymbol{d}_2 - 3d_{1,z}d_{2,z}}{R^3}, \tag{2.10}$$

where $\epsilon_0$ is the dielectric constant and $\boldsymbol{d}_1$ and $\boldsymbol{d}_2$ are the electric dipole moments of atoms 1 and 2. The $z$-axis points along the internuclear axis.

The quantum state of the atom pair is characterized by $|\gamma_1,m_{j1},\gamma_2,m_{j2}\rangle$, where the $k$th atom has quantum numbers $|\gamma_k\rangle = |n_k, \ell_k, s_k, j_k\rangle$ and where $m_{jk}$ is the Zeeman quantum

[2] The prefactor $1/4\pi\epsilon_0$ is omitted in Refs. [8, 120, 163] which use atomic units.

number associated with $j_k$. $V_{dd}$ couples $|\gamma_1,m_{j1},\gamma_2,m_{j2}\rangle$ to other pair states, which we denote with primed quantum numbers $|\gamma_1',m_{j1}',\gamma_2',m_{j2}'\rangle$ in an analogous way. The structure of $V_{dd}$ leads to the selection rules $\Delta\ell = (\ell_k' - \ell_k) \in \{-1, +1\}$, $\Delta j = (j_k' - j_k) \in \{-1, 0, +1\}$, and $\Delta m_j = (m_{jk}' - m_{jk}) \in \{-1, 0, +1\}$ for $k = 1$ and $k = 2$ [8]. We treat the problem in a coupled basis $|\gamma_1, \gamma_2, J, M\rangle$, where $J$ and $M$ are the quantum numbers corresponding to the total angular momentum $\boldsymbol{J} = \boldsymbol{j_1} + \boldsymbol{j_2}$. This is advantageous because $M = m_{j1} + m_{j2}$ is a conserved quantity for the atom pair [8]. We abbreviate $|\gamma_1, \gamma_2, J, M\rangle = |\gamma, J, M\rangle$ and $|\gamma_1',\gamma_2',J',M'\rangle = |\gamma', J',M'\rangle$.

We are interested in how $V_{dd}$ influences the atom-pair state $|\gamma, J, M\rangle$. Due to the selection rule for $\Delta\ell$, the diagonal matrix elements of $V_{dd}$ vanish. The off-diagonal coupling to atom-pair states $|\gamma', J', M'\rangle$ leads to new eigenstates of the system. The energy difference between two coupled atom-pair states $\Delta E_F = E_{\gamma'} - E_\gamma$ is called the Förster defect. If all off-diagonal matrix elements are much smaller than their respective Förster defects, which is typically the case for large $R$, then second-order perturbation theory yields the van der Waals interaction [120, 163]

$$\Delta E_{\mathrm{vdW}} = -\frac{C_6}{R^6}, \tag{2.11}$$

which is the energy shift of the perturbed eigenstate associated with $|\gamma, J, M\rangle$. This energy shift comes along with small admixtures of coupled states $|\gamma', J', M'\rangle$.

A Förster resonance [37] occurs, if one Förster defect is small compared to the associated coupling matrix element. In this situation, we assume that the interaction with all other pair states is negligible.[3] If everything else is fixed, decreasing $|\Delta E_F|$ increases the magnitude of the energy shift near a Förster resonance. In other words, the interaction is enhanced. For $\Delta E_F = 0$, the new eigenstates are equal superpositions

$$\frac{1}{\sqrt{2}}\left(|\gamma, J, M\rangle \pm |\gamma', J', M'\rangle\right) \tag{2.12}$$

with energy shifts

$$\Delta E_{dd} = \pm\frac{C_3}{R^3}. \tag{2.13}$$

For reasons discussed in Sec. 2.7, we choose the quantum numbers $48^2S_{1/2}$ and $50^2S_{1/2}$ also studied in Refs. [43, 44] for the experiment.[4] As both atoms are in $S$ states, a direct coupling only exists for atom-pair states in which both atoms are in $P$ states. The smallest Förster defect at zero electric field $\Delta E_F(0) = h \times 103\,\mathrm{MHz}$ is found for the combination of $48^2P_{1/2}$ with $49^2P_{1/2}$. Hence, we consider

$$|\gamma\rangle = |48^2S_{1/2},50^2S_{1/2}\rangle, \qquad |\gamma'\rangle = |48^2P_{1/2},49^2P_{1/2}\rangle. \tag{2.14}$$

[3] This approximation is justified if the Förster defect is sufficiently small. For somewhat larger Förster defects, it typically suffices to include only a few other pair states. There are two reasons, why this works. First, basic quantum mechanics tells us that far detuned couplings have only a small impact onto the dynamics of the system. Second, pair states with a large energy difference typically also feature a large difference in at least one of the two principal quantum numbers. This reduces the radial wave function overlap and therefore the interaction matrix elements. See Refs. [8, 43] for details.

[4] There is a sequence of electrically-tuned Förster resonances in $^{87}$Rb with $\ell_1 = \ell_2 = 0$, $j_1' = j_2' = 1/2$, $n_2 = n_1 + 2$, $n_1 = (49,48,47,\dots)$, $\Delta E_F(0)/h = (30,103,190,\dots)$ MHz, $\mathcal{E} = (0.37,0.73,1.07,\dots)$ V/cm, and $C_3/h = (1.28,1.17,1.07,\dots)$ GHz µm$^3$

A special feature of our particular choice of quantum numbers is that we have $j_1 = j_2 = j_1' = j_2' = \frac{1}{2}$ for all relevant pair states, which implies $|m_{j1}| = |m_{j2}| = \left|m_{j1}'\right| = \left|m_{j2}'\right| = \frac{1}{2}$. As a consequence, the Zeeman degeneracy of the states $|\gamma, J, M\rangle$ and $|\gamma', J', M'\rangle$ is not lifted if an electric field is applied. Hence, the direction of the electric field vector becomes irrelevant. If this was not the case, the Zeeman states of $|\gamma', J', M'\rangle$ would cause Förster resonances at different electric fields, see Refs. [43, 44, 110].

Using Ref. [125], we find the following static electric polarizabilities

$$\alpha_{48S_{1/2}} = h \times 38.01\,\mathrm{MHz\,cm^2\,V^{-2}}, \qquad \alpha_{50S_{1/2}} = h \times 50.59\,\mathrm{MHz\,cm^2\,V^{-2}}, \tag{2.15}$$

$$\alpha_{48P_{1/2}} = h \times 219.95\,\mathrm{MHz\,cm^2\,V^{-2}}, \qquad \alpha_{49P_{1/2}} = h \times 255.70\,\mathrm{MHz\,cm^2\,V^{-2}}. \tag{2.16}$$

The Förster defect in the presence of an electric field of magnitude $\mathcal{E}$ is

$$\Delta E_F(\mathcal{E}) = \Delta E_F(0) - \frac{1}{2}\Delta\alpha\mathcal{E}^2, \tag{2.17}$$

where $\Delta\alpha = \alpha_{48P_{1/2}} + \alpha_{49P_{1/2}} - \alpha_{48S_{1/2}} - \alpha_{50S_{1/2}}$. Hence, the Förster resonance is located at

$$\mathcal{E} = \sqrt{\frac{2\Delta E_F(0)}{\Delta\alpha}} = 0.73\,\frac{\mathrm{V}}{\mathrm{cm}}. \tag{2.18}$$

Note that this technique of electrically tuning a Förster resonance requires the signs of $\Delta E_F(0)$ and $\Delta\alpha$ to be equal.

We now turn to calculating the matrix elements of $V_{dd}$ with respect to $|\gamma, J, M\rangle$ and $|\gamma', J', M'\rangle$. For the states of interest, the only possible combinations are $J = 0$ and $M = 0$ or $J = 1$ and $M \in \{0, \pm 1\}$. This leads to six nonzero matrix elements given by[5]

$$\langle\gamma', 1, -1|V_{dd}|\gamma, 1, -1\rangle = \langle\gamma', 1, 1|V_{dd}|\gamma, 1, 1\rangle = -\frac{C_3}{R^3}, \tag{2.19}$$

$$\langle\gamma', 1, 0|V_{dd}|\gamma, 1, 0\rangle = \frac{2C_3}{R^3} \tag{2.20}$$

and their complex conjugates, with the dipole-dipole coefficient

$$C_3 = \frac{e^2}{4\pi\epsilon_0} \cdot R^{n_1,\ell_1,j_1}_{n_1',\ell_1',j_1'} \cdot R^{n_2,\ell_2,j_2}_{n_2',\ell_2',j_2'} \cdot \frac{2}{9}. \tag{2.21}$$

Here, $e$ is the elementary charge, $R^{n_1,\ell_1,j_1}_{n_1',\ell_1',j_1'}$ and $R^{n_2,\ell_2,j_2}_{n_2',\ell_2',j_2'}$ are radial matrix elements of atom 1 and 2, and the factor $\frac{2}{9}$ is the result for the angular part, see App. A for details. The other 58 matrix elements vanish. The fact that the moduli of the matrix elements in Eqs. (2.19) and (2.20) differ by a factor of two implies that the interaction is anisotropic.[6]

[5] By choosing different phases for the angular parts of the basis states $|\gamma, J, M\rangle$ and $|\gamma', J, M\rangle$, the phases of the matrix elements in Eqs. (2.19) and (2.20) can be changed. Hence, these phases have little physical relevance. We use the same phase convention as Ref. [28].

[6] To illustrate the effect of the anisotropy, we consider the example of an initial state in the $|\gamma\rangle$ manifold together with vanishing Förster defect and time-independent interatomic distance. Because of the anisotropy, the expectation value of $\boldsymbol{J}$ precesses around the internuclear axis. In addition, the population oscillation between the $|\gamma\rangle$ and $|\gamma'\rangle$ manifolds [119] may contain more than one frequency component because of the anisotropy.

Without loss of generality, the global phases of the radial wave functions are chosen such that all radial matrix elements become real. We find using Ref. [125]

$$R^{48S_{1/2}}_{48P_{1/2}} = 2340\ ea_0, \qquad R^{50S_{1/2}}_{49P_{1/2}} = 2304\ ea_0, \tag{2.22}$$

where $a_0$ is the Bohr radius, and

$$C_3 = h \times 1.168\,\mathrm{GHz}\,\mu\mathrm{m}^3. \tag{2.23}$$

Finally, we define the atom-pair states with exchanged quantum numbers[7]

$$|\gamma_{\mathrm{ex}}\rangle = |50^2S_{1/2}, 48^2S_{1/2}\rangle, \qquad |\gamma'_{\mathrm{ex}}\rangle = |49^2P_{1/2}, 48^2P_{1/2}\rangle, \tag{2.24}$$

Matrix elements of the form $\langle\gamma'_{\mathrm{ex}}|V_{dd}|\gamma\rangle$ or $\langle\gamma'|V_{dd}|\gamma_{\mathrm{ex}}\rangle$ are evaluated using

$$R^{48S_{1/2}}_{49P_{1/2}} = -278\ ea_0, \qquad R^{50S_{1/2}}_{48P_{1/2}} = -325\ ea_0, \tag{2.25}$$

and

$$C_3^{\mathrm{ex}} = h \times 1.960 \times 10^{-2}\,\mathrm{GHz}\,\mu\mathrm{m}^3. \tag{2.26}$$

For $M = M' = \pm 1$ we obtain a coupling scheme

$$\begin{array}{ccc} |\gamma\rangle & \xleftrightarrow{C_3} & |\gamma'\rangle \\ \updownarrow{\scriptstyle C_3^{\mathrm{ex}}} & & \updownarrow{\scriptstyle C_3^{\mathrm{ex}}} \\ |\gamma'_{\mathrm{ex}}\rangle & \xleftrightarrow{C_3} & |\gamma_{\mathrm{ex}}\rangle. \end{array} \tag{2.27}$$

For $M = M' = 0$, the scheme is similar with a factor of $-2$ in front of $C_3$ and $C_3^{\mathrm{ex}}$. In principle, these couplings can give rise to population transfer from $|\gamma\rangle$ to $|\gamma_{\mathrm{ex}}\rangle$. This is also referred to as excitation hopping or exchange interaction in the literature [110, 148].[8] However, as we have

$$C_3^{\mathrm{ex}} \approx \frac{C_3}{59.6}, \tag{2.28}$$

hopping is strongly suppressed for our quantum numbers. For this reason, we consider only the coupling of $|\gamma\rangle$ to $|\gamma'\rangle$.

[7] In Ref. [8], bosonically symmetrized states of the form $\sqrt{\frac{1}{2}}(|\gamma\rangle + |\gamma_{\mathrm{ex}}\rangle)$ are used. As our atomic ensemble is far above the critical temperature for Bose-Einstein condensation, the spatial wave functions of the atoms have very little overlap. Hence, Bose-Einstein statistics is practically irrelevant and we can pretend that the atoms are distinguishable.

[8] Ref. [148] used an atom-pair state composed of an $S$ and a $P$ state, resulting in a direct coupling from $|\gamma\rangle$ to $|\gamma_{\mathrm{ex}}\rangle$. Ref. [119] used identical $D$ states in $|\gamma\rangle$ such that $|\gamma\rangle = |\gamma_{\mathrm{ex}}\rangle$.

## 2.3 Cavity Rydberg EIT

We consider electromagnetically induced transparency (EIT) with an ensemble of three-level atoms inside an optical resonator. Cavity EIT was first studied theoretically in Ref. [91] and observed experimentally in Refs. [59, 168]. Following the general approach of Ref. [91] and building upon results from Refs. [8, 36], we briefly derive the optical response of a cavity Rydberg EIT system in the weak-signal limit. In the context of our gate protocol, we use these results to calculate the pulse shape of the target photon after reflection from the cavity.

We consider an atomic three-level system consisting of a ground state $|g\rangle$, an excited state $|e\rangle$ with $1/e$ lifetime for population decay $1/\Gamma_e$, and a Rydberg state $|r\rangle$ with $1/e$ lifetime for population decay $1/\Gamma_r$, in order of ascending energies. The signal transition $|g\rangle \leftrightarrow |e\rangle$ (coupling transition $|e\rangle \leftrightarrow |r\rangle$) with dipole matrix element $d_{ge}$ ($d_{er}$) and resonance frequency $\omega_{ge}$ ($\omega_{er}$) is driven by a monochromatic light field with complex electric field amplitude $E_{0,s}$ ($E_{0,\mathrm{co}}$), Rabi frequency $\Omega_s = -d_{ge}^* E_{0,s}/\hbar$ ($\Omega_{\mathrm{co}} = -d_{er}^* E_{0,\mathrm{co}}/\hbar$), and angular frequency $\omega$ ($\omega_{\mathrm{co}}$).

The linear electric susceptibility[9] $\chi$ of an ultracold ensemble of such three-level atoms with density $\varrho$ is obtained from a quantum master equation treatment [36], similar to App. B. This includes decay of the density matrix element $\rho_{rg}$ according to $\partial_t \rho_{rg} = -\frac{1}{2}\gamma_{rg}\rho_{rg}$, where $\gamma_{rg} = \Gamma_r + \gamma_{r\mathrm{deph}}$ with a dephasing rate $\gamma_{r\mathrm{deph}}$. The result is [8]

$$\chi = \chi_0 \frac{i\Gamma_e}{\Gamma_e - 2i\Delta_s + \frac{|\Omega_{\mathrm{co}}|^2}{\gamma_{rg} - 2i(\Delta_s + \Delta_{\mathrm{co}})}} \tag{2.29}$$

with the signal (coupling) detuning $\Delta_s = \omega - \omega_{ge}$ ($\Delta_{\mathrm{co}} = \omega_{\mathrm{co}} - \omega_{er}$) and

$$\chi_0 = \frac{2\varrho\,|d_{ge}|^2}{\epsilon_0 \hbar \Gamma_e}. \tag{2.30}$$

The electric susceptibility is related to the refractive index by [36] $n = \sqrt{1+\chi} \approx 1 + \frac{1}{2}\chi$, where the approximation is typically quite good in our experiments because the atomic density is relatively low. Assuming a transversely homogeneous medium of length $L_m$, the amplitude transmission coefficient relative to free space propagation is $t_a = \exp(i\frac{\omega}{2c}\chi L_m)$ so that

$$t_a = \exp\left(-\frac{d_t \Gamma_e/2}{\Gamma_e - 2i\Delta_s + \frac{|\Omega_{\mathrm{co}}|^2}{\gamma_{rg} - 2i(\Delta_{\mathrm{co}} + \Delta_s)}}\right) \tag{2.31}$$

with the resonant optical depth $d_t = L_m \varrho \sigma_{\mathrm{abs}}$ and with the absoption cross section $\sigma_{\mathrm{abs}} = 2\omega\,|d_{ge}|^2 / (\epsilon_0 \hbar c \Gamma_e)$.

The reflectivity of a cavity Rydberg EIT system in the weak-signal limit is obtained by inserting Eq. (2.31) into Eq. (2.2). Under the assumptions $d_t \ll 1$, $\mathcal{F} \gg 1$, and

[9] We neglect the nonlinear optical response [32, 137] caused by the Rydberg-Rydberg interaction here. In our experiments, the incoming photon rate of the signal light field is typically very low. Hence, the probability for having more than one signal photon inside the medium at the same time is small. The nonlinearity required for the quantum gate emerges from the modification to the linear optical response in the presence of a previously stored control excitation, see Sec. 2.5.

$|\Delta_c| \ll \Delta\omega_{\mathrm{ax}}$, the reflectivity simplifies to

$$\mathcal{R} = -1 + \frac{2\beta}{1 + C_{\mathrm{eff}} - i\Delta_c/\kappa}, \tag{2.32}$$

where we introduced the complex effective cooperativity

$$C_{\mathrm{eff}} = -\frac{\mathcal{F}}{\pi} \ln t_a. \tag{2.33}$$

Fig. 5.2 in Sec. 5.2 presents cavity Rydberg EIT spectra which are well described by a model based on Eq. (2.32).

Note that equivalent results are obtained from a fully quantized model [22] based on cavity input-output theory, when the Hilbert space is restricted to quantum states that contain at most a single excitation. The quantized model assumes a single longitudinal cavity mode, which is justified for $d_t \ll 1$, $\mathcal{F} \gg 1$, and $|\Delta_c| \ll \Delta\omega_{\mathrm{ax}}$. One considers $N$ atoms at positions $\boldsymbol{r}_\ell$, each of which is coupled to the cavity mode by the coupling constant $g_\ell = g \cdot m(\boldsymbol{r}_\ell)/m(\boldsymbol{0})$. Here, $m(\boldsymbol{r}_\ell)$ is the transverse mode function of the cavity, see Sec. 3.2, and

$$g = \sqrt{\frac{\omega \left|d_{ge}\right|^2 \Delta\omega_{\mathrm{ax}}}{2\pi^2 w_c^2 \epsilon_0 \hbar c}} \tag{2.34}$$

is half the vacuum Rabi frequency at the center of the cavity mode waist with $1/e^2$ radius of intensity $w_c$. The equivalence of the two models can be observed by setting $\Omega_{\mathrm{co}} = 0$ and $\Delta_c = \Delta_s = 0$ for all atoms. In this situation, $C_{\mathrm{eff}}$ in Eq. (2.32) becomes the collective cooperativity [156]

$$C = \frac{d_t \mathcal{F}}{2\pi} \tag{2.35}$$

and the model from Ref. [22] reproduces Eq. (2.32) with

$$C = C_1 N_{\mathrm{eff}}, \tag{2.36}$$

where $C$ is real and positive, $N_{\mathrm{eff}} = \sum_\ell \left|g_\ell\right|^2 / g^2$ is the effective number of maximally coupled atoms, and $C_1 = \frac{g^2}{\kappa\Gamma_e/2}$ is the cooperativity of a single, maximally coupled atom.

Alternatively, one can assume that all atoms are placed at the center of the cavity mode waist such that $g_\ell = g$, which contradicts our previous assumption of a transversely homogeneous medium. In this situation, we find

$$C = \frac{d_{t,\mathrm{eff}} \mathcal{F}}{2\pi} = \frac{g^2 N}{\kappa\Gamma_e/2} \tag{2.37}$$

with an effective optical depth

$$d_{t,\mathrm{eff}} = N \frac{2\sigma_{\mathrm{abs}}}{\pi w_c^2}. \tag{2.38}$$

The fact that both models produce consistent results is not surprising. For instance, it is well known that "vacuum-Rabi splitting due to atom-cavity coupling can be understood both quantum mechanically, in terms of dressed states of an atom-cavity system, as well

as classically, in the context of a modified index of refraction, for a single atom as well as for large $N$" [156], see also Refs. [2, 145]. For cavity EIT, the origin of the equivalence is the same, see also a related discussion in Ref. [46].

While the treatment so far assumed monochromatic signal light, we now consider pulsed signal light. Assuming that the incoming target pulse has a slowly varying temporal envelope $u_t(t)$, we want to calculate the slowly varying temporal envelope $u_{\mathcal{R}}(t)$ of the light which is reflected from the cavity. To this end, we introduce the frequency domain versions

$$\widetilde{u}_t(\omega) = \frac{1}{\sqrt{2\pi}} \int_{-\infty}^{+\infty} u_t(t) \exp(i\omega t) dt \tag{2.39}$$

and similarly $\widetilde{u}_{\mathcal{R}}(\omega)$. The incoming pulse is normalized according to

$$\int_{-\infty}^{+\infty} |u_t(t)|^2 \, dt = \int_{-\infty}^{+\infty} |\widetilde{u}_t(\omega)|^2 \, d\omega = 1. \tag{2.40}$$

As we consider the weak-driving limit, the cavity Rydberg EIT system is linear, so that the response to a pulse can be obtained by a simple superposition of monochromatic components. Hence

$$\widetilde{u}_{\mathcal{R}}(\omega) = \mathcal{R}(\omega)\widetilde{u}_t(\omega). \tag{2.41}$$

As $u_{\mathcal{R}}(t)$ follows from this relation by applying an inverse Fourier transformation, the normalization of $u_{\mathcal{R}}(t)$ typically differs from Eq. (2.40). This reduced norm represents loss of photons inside the cavity caused by spontaneous emission or by imperfect HR cavity mirrors.

For $\gamma_{rg} = 0$, $\Delta_{\mathrm{co}} = 0$, $\beta = 1$, and for atom-cavity resonance $\omega_c = \omega_{ge}$, which implies $\Delta_c = \Delta_s$, we expand $\mathcal{R} = 1 + i\frac{2}{\kappa_F}\Delta_s + O(\Delta_s^2)$, which we rewrite as

$$\mathcal{R}(\Delta_s) = \exp\left(i\frac{2}{\kappa_F}\Delta_s\right) + O(\Delta_s^2) \tag{2.42}$$

with the cavity EIT linewidth

$$\kappa_F = \left(\frac{1}{\kappa} + \frac{2C\Gamma_e}{|\Omega_{\mathrm{co}}|^2}\right)^{-1}. \tag{2.43}$$

If the input signal pulse envelope varies sufficiently slowly such that its Fourier spectrum is narrow compared to $\kappa_F$, deformations of the output pulse are negligible and the dominant effect is a pulse delay[10]

$$t_d = \frac{2}{\kappa_F}. \tag{2.44}$$

[10] This immediately follows from Eq. (2.42) together with the Fourier transform property $u_t(t - t_d) = \frac{1}{\sqrt{2\pi}} \int_{-\infty}^{+\infty} \widetilde{u}_t(\omega) \exp(i\omega t_d) \exp(-i\omega t) d\omega$.

## 2.4 Storage and Retrieval of Photons

We now extend the above-discussed situation of cavity Rydberg EIT to a time-dependent coupling light field. As discussed in Ref. [46], coherent storage and retrieval of signal light pulses can be achieved by employing appropriately shaped coupling light pulses. In our gate protocol, this technique is applied to the control photon.

The dynamics of the system are governed by the Heisenberg equations of motion [46]

$$\mathcal{E}_{\text{out}}(t) = \sqrt{2\kappa_{\text{in}}}\mathcal{E}(t) - \mathcal{E}_{\text{in}}(t), \tag{2.45}$$

$$\partial_t \mathcal{E} = \left(i\Delta_c - \kappa_{\text{in}} - \kappa_H\right)\mathcal{E} + i\sqrt{\frac{1}{2}\kappa\Gamma_e C}P + \sqrt{2\kappa_{\text{in}}}\mathcal{E}_{\text{in}}, \tag{2.46}$$

$$\partial_t P = \left(i\Delta_s - \frac{\Gamma_e}{2}\right)P + i\sqrt{\frac{1}{2}\kappa\Gamma_e C}\mathcal{E} + i\frac{\Omega_{\text{co}}}{2}S, \tag{2.47}$$

$$\partial_t S = \left(i\Delta_{\text{co}} + i\Delta_s - \frac{\gamma_{rg}}{2}\right)S + i\frac{\Omega_{\text{co}}^*}{2}P. \tag{2.48}$$

Here, $\mathcal{E}_{\text{in}}$ is the quantized incoming signal field, $\mathcal{E}_{\text{out}}$ is the quantized outgoing signal field, $\mathcal{E}$ is the quantized intra-cavity field, $P$ is the annihilation operator for one Dicke-state excitation in $|e\rangle$, and $S$ is the annihilation operator for one Dicke-state excitation in $|r\rangle$. In principle, the fact that decay terms are included in these Heisenberg equations of motion would require Langevin noise terms. However, for the purpose of calculating efficiencies and for suitable initial conditions [46], one can simply take the expectation value of the original Heisenberg equations and finds that the noise terms vanish. Hence, for practical purposes the operators in Eqs. (2.45)–(2.48) can be replaced by complex numbers.

Our model is a minor extension of Ref. [46] insofar as it contains more detunings and it contains the term $-\kappa_H\mathcal{E}$ in Eq. (2.46), which describes decay of the intracavity field through the HR cavity mirrors. In the steady state $\partial_t\mathcal{E} = \partial_t P = \partial_t S = 0$ and with the ansatz $\mathcal{E}_{\text{out}}(t) = \mathcal{R}\mathcal{E}_{\text{in}}(t)$, this model reproduces Eqs. (2.31)–(2.33).

We introduce the smooth envelope $u_c(t)$ of the incoming signal light pulse by $\mathcal{E}_{\text{in}}(t) \propto u_c(t)$ with the normalization condition from Eq. (2.40) and the property $u_c(t) = 0$ for $t < 0$ or $t > T_c$, where $T_c$ is the duration of the pulse. We assume that the desired outgoing signal envelope is identical to the incoming pulse shape and has the form $\mathcal{E}_{\text{out}}(t + t_r) \propto u_c(t)$, where $t_r$ is the time at which the retrieval begins. In the dark time $t_{\text{dark}} = t_r - T_c$ between storage and retrieval, we assume $\mathcal{E}_{\text{in}}(t) = 0$ and $\Omega_{\text{co}} = 0$. For a given temporal envelope $\Omega_{\text{co}}(t)$ of the coupling Rabi frequency, we numerically solve Eqs. (2.45)–(2.48). The combined efficiency of storage and retrieval $\eta_{sr}$ is the ratio of the energy in the output pulse to the energy in the input pulse.

Calculating the temporal envelope $\Omega_{\text{co}}(t)$ of the coupling Rabi frequency which maximizes the storage efficiency $\eta_s$ is a nonlinear optimal control problem, solving which is generally nontrivial. To obtain analytic results, we follow Ref. [46] and adiabatically eliminate $\mathcal{E}$ and $P$ from the model by setting $\partial_t\mathcal{E} = \partial_t P = 0$. This is justified, e.g. if we assume the bad-cavity limit $\sqrt{C\Gamma_e/2\kappa} \ll 1$ and if we assume that the normalized control pulse envelope $u_c(t)$ varies slowly.

Assuming resonant light fields $\Delta_c = \Delta_s = \Delta_{\mathrm{co}} = 0$, we calculate the storage efficiency in this adiabatic limit along the lines of Ref. [46] and find

$$\eta_{s,\mathrm{ad}} = \beta \frac{C}{C+1} e^{-\gamma_{rg} T_c} \int_0^{T_c} dt e^{\gamma_{rg} t} \left| u_c(t) \right|^2 \tag{2.49}$$

along with the optimal storage coupling pulse

$$\Omega_{\mathrm{co}}(t) = -\sqrt{\Gamma_e (C+1)} \frac{e^{\gamma_{rg} t/2} u_c(t)}{\sqrt{\int_0^t dt' e^{\gamma_{rg} t} \left| u_c(t) \right|^2}}. \tag{2.50}$$

Similarly, we calculate the retrieval efficiency in this adiabatic limit

$$\eta_{r,\mathrm{ad}} = \beta \frac{C}{C+1} \left( \int_0^{T_c} dt e^{\gamma_{rg} t} \left| u_c(t) \right|^2 \right)^{-1} \tag{2.51}$$

along with the optimal coupling pulse for retrieval with envelope $u_c(t)$

$$\Omega_{\mathrm{co}}\left(t + t_r\right) = -\sqrt{\Gamma_e (C+1)} \frac{e^{\gamma_{rg} t/2} u_c(t)}{\sqrt{\int_t^{T_c} dt' e^{\gamma_{rg} t} \left| u_c(t) \right|^2}}. \tag{2.52}$$

The solution of Eq. (2.48) during the dark time leads to an additional decay of the retrieval signal according to

$$\eta_{\mathrm{dark}} = e^{-\gamma_{rg} t_{\mathrm{dark}}}. \tag{2.53}$$

Hence, the overall write-read efficiency in this adiabatic limit is

$$\eta_{sr,\mathrm{ad}} = \eta_{s,\mathrm{ad}} \eta_{r,\mathrm{ad}} \eta_{\mathrm{dark}} = \left( \beta \frac{C}{C+1} \right)^2 e^{-\gamma_{rg} (T_c + t_{\mathrm{dark}})}. \tag{2.54}$$

Note that the integrals appearing in Eqs. (2.49) and (2.51) canceled here. The appearance of the exponential factor in Eq. (2.54) is plausible because each temporal component of the pulse is delayed by $T_c + t_{\mathrm{dark}}$ and experienced dephasing during this time.

## 2.5 Cavity Rydberg Blockade

Next, we consider cavity Rydberg EIT similar to Sec. 2.3, but with the important difference that a stationary Rydberg excitation in state $|r'\rangle$ was previously created in the atomic ensemble. In this setting, the excitation $|r'\rangle$ suppresses the formation of a second excitation $|r\rangle$ due to the long-range Rydberg-Rydberg interaction. This effect is called Rydberg blockade [155]. Ref. [22] developed a cavity model for such a blockade situation. This model consists of two steps; first, the cavity reflection coefficient $\mathcal{R}_k(\omega)$ for the target light is calculated under the hypothetical assumption that the control photon is stored in the $k$th atom; second, the outgoing target wave packet is calculated taking into account that the control photon is actually stored in a Dicke state and that the experimental data are postselected upon detection of a retrieved control photon.

In the first step, Ref. [22] assumes that the Rydberg-Rydberg interaction is well approximated as a van der Waals interaction. As our experiment is operated near a Förster resonance, this calculation of $\mathcal{R}_k(\omega)$ requires a generalization, which we discuss in Sec. 2.5.1. Among other things, this generalization leads us to an expression for the blockade radius in Sec. 2.5.2, which serves as a guideline as to the kind of cloud radii, for which a superatom model is a good approximation.

The second step of the calculation in Ref. [22], however, applies to our experiment without any changes except that the expression for $\mathcal{R}_k(\omega)$ is different. We summarize this calculation in Sec. 2.5.3.

### 2.5.1 Cavity Reflection Coefficient Assuming Storage in a Particular Atom

Under the hypothetical assumption that the control photon is stored in the $k$th atom, we can define a cavity reflection coefficient $\mathcal{R}_k(\omega)$ for monochromatic target light with angular frequency $\omega$ in analogy to Eq. (2.41). Ref. [22] calculated $\mathcal{R}_k(\omega)$ assuming a van der Waals interaction. We generalize this calculation to the presence of a Förster resonance. This is discussed in detail in App. B. The central result for $\mathcal{R}_k(\omega)$ is found in Eqs. (B.19), (B.25), and (B.23).

### 2.5.2 Blockade Radius

In a superatom geometry, the calculation simplifies drastically because Eq. (B.19) reduces to $\alpha_{k\ell} = \alpha_{\text{2level}}$, which is independent of $k$ and $\ell$. Here $\alpha_{\text{2level}}(\omega)$ of Eq. (B.30) is the dynamic polarizability of a two-level atom and $\alpha_{k\ell}(\omega)$ is the dynamic polarizability of the $\ell$th atom illuminated with target light, given that the control photon is stored in the $k$th atom. Hence, it is an interesting question how large the spatial extension of the atom cloud can be for the superatom model to be a good approximation.

To answer this question, one defines a blockade radius. It describes the distance between the $k$th and $l$th atoms over which the blockade effect loses its strength. This blockade strength has to be expressed in terms of some figure of merit. If we use the dynamic polarizability $\alpha_{k\ell}$ as the figure of merit, we find a blockade radius of, see Eq. (B.31)

$$R_b = \left| \left( \frac{2C_3}{\hbar \Omega_{\text{co}}} \right)^2 \frac{\Gamma_e - 2i\Delta_s}{\gamma_F - 2i\Delta_F} \right|^{1/6}, \tag{2.55}$$

where $\gamma_F$ is a dephasing rate associated with the Förster-resonant atom-pair states $|\gamma'\rangle$.

The above-defined blockade radius is a quantity which depends only on the properties of an atom pair. The optical response of the cavity Rydberg EIT system, however, additionally depends on the number of atoms $N$ and the properties of the cavity. One can incorporate this dependence in the definition of an alternative quantity, for which we use $\mathcal{R}_k(\omega)$ as the figure of merit. This yields a quantity which we call the collective blockade radius $R_{\text{coll}}$. According to Eq. (B.36), it is given by

$$R_{\text{coll}} = R_b C^{1/6}, \tag{2.56}$$

where $R_b$ is the blockade radius of Eq. (2.55) and $C$ is the collective cooperativity. As $C$ is proportional to the number of atoms, this represents a collective enhancement of $R_b$, which otherwise depends only on $C_3$ and single-atom properties.

### 2.5.3 Outgoing Target Wave Packet

We now calculate the outgoing target wave packet, taking into account that the control photon is actually stored in a Dicke state and that the experimental data are postselected upon detection of a retrieved control photon. To this end, we start from the quantum state of the atomic ensemble after storage of the control photon. Ideally, it is a Dicke state of the form [21, 133]

$$|S\rangle = \sum_{k=1}^{N} \alpha_k |g^{N-1}, r'_k\rangle \tag{2.57}$$

where the complex coefficients $\alpha_k$ fulfill $\sum_{k=1}^{N} |\alpha_k|^2 = 1$ and where $|g^{N-1}, r'_k\rangle$ denotes a state of the atomic ensemble, in which the $k$th atom carries the excitation $|r'\rangle$ and the other $N-1$ atoms are in the ground state $|g\rangle$.

After the target photon has been sent onto the cavity, the combined quantum state of the atomic ensemble and the target photon is

$$|\Psi_{\mathrm{S}}\rangle = c_{\mathrm{refl}} |\Psi_{\mathrm{refl}}\rangle + c_{\mathrm{loss}} |\Psi^{(1)}_{\mathrm{loss}}\rangle. \tag{2.58}$$

Here, $c_{\mathrm{refl}}$ and $c_{\mathrm{loss}}$ are complex coefficients which fulfill $|c_{\mathrm{refl}}|^2 + |c_{\mathrm{loss}}|^2 = 1$, the normalized state $|\Psi_{\mathrm{refl}}\rangle$ represents the possibility that the target photon is reflected from the cavity, and the normalized state $|\Psi^{(1)}_{\mathrm{loss}}\rangle$ represents the possibility that the target photon is lost due to atomic spontaneous emission or imperfect cavity mirrors. The state of the incoming target photon is

$$\int_{-\infty}^{+\infty} d\omega \widetilde{u}_t(\omega) a^\dagger_\omega e^{-i\omega t} |\varnothing\rangle. \tag{2.59}$$

Here, $|\varnothing\rangle$ is the vacuum of all optical modes and $a^\dagger_\omega$ is a bosonic creation operator for a target photon with angular frequency $\omega$ in the outgoing spatial mode. Combining this with Eq. (2.41) yields

$$c_{\mathrm{refl}} |\Psi_{\mathrm{refl}}\rangle = \sum_{k=1}^{N} \alpha_k |g^{N-1}, r'_k\rangle \otimes \int_{-\infty}^{+\infty} d\omega \mathcal{R}_k(\omega) \widetilde{u}_t(\omega) a^\dagger_\omega e^{-i\omega t} |\varnothing\rangle, \tag{2.60}$$

see also Eq. (S44) in Ref. [21]. Note that the state in Eq. (2.60) features entanglement between the reflected target pulse and the atomic state, because $\mathcal{R}_k(\omega)$ depends on $k$ and $\omega$ simultaneously.

In our gate experiment, we attempt to store and retrieve the control photon. In the absence of a target photon, the combined probability for storage and retrieval of the control photon is $\eta_{sr}$. In the rest of Sec. 2.5, we assume that $\eta_{sr}$ is solely due to the values of $\beta$ and $C$ according to Eqs. (2.49) and (2.51) and we neglect any contribution from dephasing of $|S\rangle$ during the storage time.

To calculate the state of the system after the retrieval attempt in the presence of a target photon, we need the scalar product between $|\Psi_\mathrm{S}\rangle$ and the initial Dicke state $|S\rangle$, because atomic states orthogonal to $|S\rangle$ are not coupled to the control output mode [21, 133]. If retrieval is successful, the final state of the atoms is $|g^N\rangle$ and the retrieved control photon is in a normalized quantum state, which we denote as $|\phi_c\rangle$. From Eq. (2.58), we find

$$|\Psi_\mathrm{final}\rangle = \sqrt{1-p_\mathrm{2ph}}|\Psi^{(2)}_\mathrm{loss}\rangle + \sqrt{\eta_{sr}}|\phi_c\rangle \otimes |g^N\rangle\langle S|c_\mathrm{refl}|\Psi_\mathrm{refl}\rangle, \tag{2.61}$$

where $p_\mathrm{2ph}$ is the probability that none of the two photons is lost and the normalized state $|\Psi^{(2)}_\mathrm{loss}\rangle$ represents the possibility that at least one photon is lost. Combining Eqs. (2.58) and (2.60), we obtain

$$\langle S|c_\mathrm{refl}|\Psi_\mathrm{refl}\rangle = \int_{-\infty}^{+\infty} d\omega \widetilde{u}_b(\omega) a^\dagger_\omega e^{-i\omega t}|\varnothing\rangle, \tag{2.62}$$

in analogy to Eq. (2.59), where we abbreviated

$$\widetilde{u}_b(\omega) = \widetilde{u}_t(\omega)\sum_{k=1}^{N}|\alpha_k|^2\,\mathcal{R}_k(\omega). \tag{2.63}$$

Note that the lossless component of Eq. (2.61) is a product state. The entanglement that was present in Eq. (2.60) is automatically absorbed in $|\Psi^{(2)}_\mathrm{loss}\rangle$ when postselecting upon survival of both photons.

In the limit of a perfect superatom geometry, $\mathcal{R}_k(\omega)$ is independent of $k$. Hence, we can write $\mathcal{R}_b(\omega)$ instead of $\mathcal{R}_k(\omega)$, and Eq. (2.63) simplifies to

$$\widetilde{u}_b(\omega) = \mathcal{R}_b(\omega)\widetilde{u}_t(\omega), \tag{2.64}$$

which is analogous to Eq. (2.41) for $\widetilde{u}_\mathcal{R}(\omega)$ without blockade. Hence, storing the control photon changes the properties of the reflected target photon. This is the origin of the conditional $\pi$-phase shift, on which the gate is built. Note, however, that the target photon leaves the retrieval efficiency $\eta_{sr}$ of the control photon unchanged in this case.

Without such a perfect superatom geometry, however, the fact that a *target* photon was reflected from the cavity does change the retrieval efficiency of the *control* photon, which is due to the $k$-dependence of $\mathcal{R}_k$. This $k$-dependence effectively modifies the amplitudes and phases of the summands in $|\Psi_\mathrm{refl}\rangle$ such that the overlap with the Dicke state $|S\rangle$ decreases. This yields a combined storage and retrieval efficiency $\eta_{sr,t}(\omega)$ that is by definition postselected upon successful reflection of a target photon, i.e. the target photon is not lost.[11] Without deriving an expression for $\eta_{sr,t}(\omega)$, we can generalize the above definition of $\mathcal{R}_b(\omega)$ to non-superatom geometries by setting

$$\widetilde{u}_b(\omega) = \sqrt{\frac{\eta_{sr,t}(\omega)}{\eta_{sr}}}\mathcal{R}_b(\omega)\widetilde{u}_t(\omega). \tag{2.65}$$

[11] A non-postselected version of $\eta_{sr,t}(\omega)$ cannot be obtained by considering only $\widetilde{u}_b(\omega)$ because that misses those components of $|\Psi_\mathrm{final}\rangle$ in Eq. (2.61), in which the control photon is retrieved while the target photon is lost. The dependence of $\eta_{sr,t}(\omega)$ on the angular frequency $\omega$ of the target photon is plausible because far detuned target light should have a negligible effect.

While this decomposition of $\widetilde{u}_b(\omega)$ into $\sqrt{\eta_{sr,t}(\omega)}$ and $\mathcal{R}_b(\omega)$ clarifies the underlying physical concepts, this decomposition is of little relevance for our experiment because that only relies on $\widetilde{u}_b(\omega)$. Hence, experimental or theoretical studies of $\eta_{sr,t}(\omega)$ are beyond the scope of the present work.

## 2.6 Photon-Photon Gate

### 2.6.1 Protocol

This section explains how a quantum-logic gate between two photons can be implemented using the above-described techniques. Our scheme is a minor modification of the proposal in Ref. [22]. The key idea is that a cavity converts conditional loss into a conditional $\pi$ phase shift, see also Fig. 2.2. Using Rydberg blockade to create intra-cavity loss conditioned on the presence of a previously stored control photon, we obtain a CPHASE gate for the photon number states $|0\rangle$ and $|1\rangle$ of the control and target photon.

Using the spatial dual-rail setup shown in Fig. 2.3, we map between incoming and outgoing polarization qubits and internal dual-rail qubits. Polarizing beam splitters (PBSs) at the input and output of the gate transmit (reflect) the horizontally (vertically) polarized $|H\rangle$ ($|V\rangle$) component of the qubits. Hence, it is only for the component $|HV\rangle = |H\rangle \otimes |V\rangle$ of the two-photon input state that both qubits interact with the cavity. In our notation for a two-photon state such as $|HV\rangle$, the control photon is always listed first. The resulting quantum-logic gate is ideally characterized by a linear map from pure states onto pure states, defined by

$$\begin{array}{rcl} |HH\rangle & \mapsto & |HH\rangle \\ |HV\rangle & \mapsto & e^{i\pi}\,|HV\rangle \\ |VH\rangle & \mapsto & |VH\rangle \\ |VV\rangle & \mapsto & |VV\rangle. \end{array} \tag{2.66}$$

Note that some optical elements, such as waveplates and lenses, are not drawn in Fig. 2.3. For a definition of our polarization conventions, including diagonal $|D\rangle$, anti-diagonal $|A\rangle$, left-handed circular $|L\rangle$, and right-handed circular $|R\rangle$, see App. D.

The timing sequence of the gate operation consists of three steps. In the first step, a light pulse containing the control photon is sent into the system. A PBS maps the incoming polarization qubit onto a dual-rail qubit. One rail bypasses the cavity, the other impinges onto the cavity, where the photon is stored using the techniques described in Sec. 2.4. In the second step, a light pulse containing the target photon enters the system. A PBS maps the incoming polarization qubit onto a dual-rail qubit. One rail bypasses the cavity, the other is reflected from the cavity, acquiring the conditional $\pi$ phase shift. The two components are recombined on a PBS, which converts the dual-rail qubit back into a polarization qubit. In the third step, the stored component of the control photon is retrieved from the cavity and recombined with the bypass component at the output PBS, which converts the dual-rail qubit back into a polarization qubit. To match the delay caused by storage and retrieval, the bypass contains a long fiber that causes a corresponding delay.

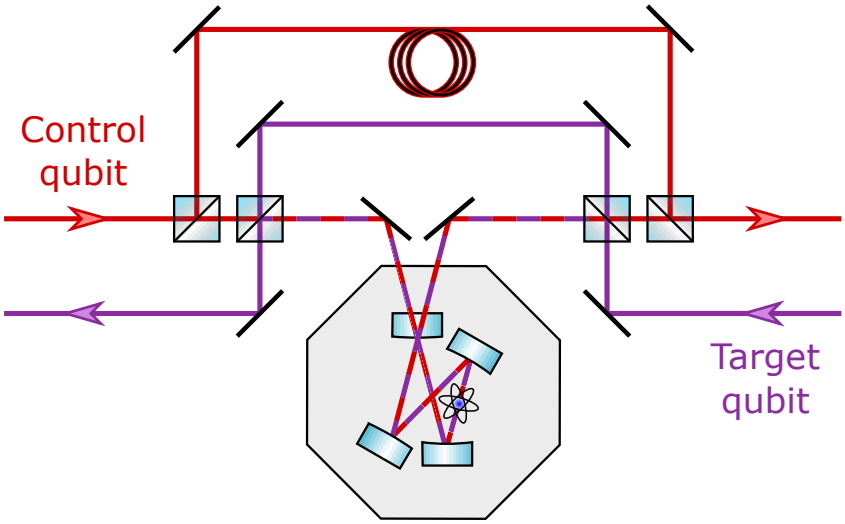


**Figure 2.3:** Scheme of the gate. The control (target) photon travels through the setup from left to right (right to left). Polarizing beam splitters (blue squares) map between incoming and outgoing polarization qubits and internal dual-rail qubits. One rail of each qubit impinges onto the cavity, the other rail bypasses the cavity. If the control qubit impinges onto the cavity, it is stored in a Rydberg state. Subsequently, the target photon enters the system. A conditional $\pi$ phase shift is experienced if both qubits are in their cavity rails. After the interaction with the target photon, the control photon is retrieved. The bypass rail of the control qubit is delayed in an optical fiber to match the delay resulting from storage. The octagon represents the vacuum chamber.

### 2.6.2 Fidelity and Efficiency

To quantify how closely the implementation of the gate resembles the ideal $\pi$ phase gate in Eq. (2.66), Ref. [22] studied the Choi-Jamiolkowski process fidelity $F_{\mathrm{CJ}}$ [42] and a second version of the fidelity $F_{\mathrm{swap}}P_{\mathrm{suc}}$ which is relevant for entanglement swapping based on Bell-state detection. For our experiment, we also consider the state fidelity obtained when trying to produce a maximally entangled Bell state. Within the assumptions of our model the Bell-state fidelity is equivalent to the process fidelity from Ref. [22], as shown in App. C.

Ideally, a maximally entangled output state is obtained, if each qubit is in a 50:50 superposition of the basis states $|H\rangle$ and $|V\rangle$. We consider the input state

$$|\psi_{\mathrm{in}}\rangle = |DD\rangle, \tag{2.67}$$

for which Eq. (2.66) predicts the output state $|\psi_{\mathrm{Bell}}\rangle = \frac{1}{\sqrt{2}}(|HA\rangle + |VD\rangle)$. The actual output state of this entangling gate operation is described by a density matrix $\rho_{\mathrm{out}}$ and the fidelity with which this state matches the ideal output state is the Bell-state fidelity [42, 71]

$$F = \langle\psi_{\mathrm{Bell}}|\rho_{\mathrm{out}}|\psi_{\mathrm{Bell}}\rangle. \tag{2.68}$$

If the output state is a pure state, then $\rho_{\text{out}} = |\psi_{\text{out}}\rangle\langle\psi_{\text{out}}|$ and Eq. (2.68) simplifies to

$$F = |\langle \psi_{\text{Bell}}| \psi_{\text{out}}\rangle|^2 . \tag{2.69}$$

We apply this to the scheme in Fig. 2.3 for a monochromatic target light field with angular frequency $\omega$. We obtain

$$F(\omega) = \left| \frac{c_H t_H - c_H t_V \sum_{k=1}^{N} |\alpha_k|^2 \mathcal{R}_k(\omega) + c_V t_H + c_V t_V \mathcal{R}(\omega)}{4} \right|^2 , \tag{2.70}$$

where $c_H$, $c_V$, $t_H$, and $t_V$ are positive numbers. $c_j^2$ ($t_j^2$) with $j \in \{H, V\}$ is the probability that the control photon is not lost (the target photon is not lost outside the cavity), if this photon is in state $|j\rangle$. If we assume that all beam splitters, waveplates, and mirrors outside the cavity are lossless, then we obtain $c_H = \sqrt{\eta_{sr}}$, $c_V = \sqrt{\eta_{\text{delay}}}$, and $t_H = t_V = 1$, where $\eta_{\text{delay}}$ is the transmission through the delay fiber.

So far we neglected that the light fields are pulsed. In App. C, two options are discussed how Eq. (2.70) can be generalized for pulsed light fields. These options differ with respect to how much emphasis is put on the envelope of the outgoing light pulses. Here, we consider only the version of the fidelity that we measure in our experiments. According to App. C, we can express this fidelity as

$$F = \int_{-\infty}^{+\infty} d\omega \, |\widetilde{u}_t(\omega)|^2 \, F_p(\omega) \tag{2.71}$$

with

$$F_p(\omega) = \frac{|Q(\omega)|^2 + |Q_b(\omega)|^2}{16} + \frac{\mathcal{C}_c Q^*(\omega) Q_b(\omega) + \text{ c.c.}}{16}, \tag{2.72}$$

where we abbreviated

$$Q(\omega) = c_V t_H + c_V t_V \mathcal{R}(\omega), \tag{2.73}$$

$$Q_b(\omega) = c_H t_H + c_H t_V \sum_{k=1}^{N} |\alpha_k|^2 \mathcal{R}_k(\omega), \tag{2.74}$$

$$\mathcal{C}_c = \int_{-\infty}^{\infty} u^*_{\text{delay}}(t) u_{\text{retr}}(t) dt. \tag{2.75}$$

Here, $u_{\text{delay}}(t)$ is the outgoing envelope of the part of the control light pulse that is transmitted through the delay fiber, while $u_{\text{retr}}(t)$ is the outgoing envelope of the control pulse retrieved from the cavity. Both envelopes are normalized according to Eq. (2.40).

The frequency integral in Eq. (2.71) mainly accounts for a reduction of the fidelity due to a conditional delay of the target pulse. To see this, consider the delay in the cavity EIT situation from Eq. (2.44). This delay is absent for strong cavity Rydberg blockade, because the intra-cavity field is strongly suppressed in that situation and the target pulse is essentially just reflected from the I/O coupler. As a result, the temporal overlap between the components $|H\rangle$ and $|V\rangle$ of the target pulse is reduced. This leads to a reduction

of the fidelity. As this delay is conditioned on the qubit value of the control photon, it cannot simply be compensated by local modifications to the outgoing target pulse envelope. Note that this conditional pulse delay can become arbitrarily small by making $\kappa$ and $\Omega_{\mathrm{co}}$ large according to Eq. (2.43). Hence, this does not set a fundamental limit on the gate performance.

Beyond this conditional delay, loss of photons is often a much more relevant source of imperfections. Hence, it is advantageous to postselect results upon detection of both photons. The efficiency $\eta$ of the gate is the probability that none of the two input photons is lost. According to App. C, it can be written as

$$\eta = \int_{-\infty}^{+\infty} d\omega \, |\widetilde{u}_t(\omega)|^2 \, \eta(\omega) \tag{2.76}$$

with

$$\eta(\omega) = \frac{|c_H t_H|^2 + \left|c_H t_V \sum_{k=1}^{N} |\alpha_k|^2 \mathcal{R}_k(\omega)\right|^2 + |c_V t_H|^2 + |c_V t_V \mathcal{R}(\omega)|^2}{4}. \tag{2.77}$$

For the fidelity in the postselected subensemble, we obtain

$$F_{\mathrm{post}} = \frac{F}{\eta}, \tag{2.78}$$

see App. C. It turns out that $F_{\mathrm{post}}$ and $\eta$ are identical to $F_{\mathrm{swap}}$ and $P_{\mathrm{suc}}$ in Ref. [22].

## 2.7 Optimal Parameters for the Experiment

The proposals [22, 54] mostly concentrated on developing a mathematical framework for modeling the proposed scheme and analyzing the effect of a finite strength of the Rydberg-Rydberg interaction. In addition, they estimated the performance of the gate, predicting a fidelity of $F > 99\%$ in Ref. [54] and a postselected fidelity of $F > 99\%$, an additional error due to finite bandwidth below 2%, and a combined storage and retrieval efficiency of 90% in Ref. [22].

Here, we include dephasing, lack of adiabaticity during storage and retrieval, and photon loss in optical components into the model of Ref. [22]. As a result, the question of how to choose experimental parameter values to maximize the fidelity of the gate becomes nontrivial. We discuss this optimization procedure below and find that even in the presence of these experimental imperfections, a fidelity of the entangling gate operation of $F > 50\%$ can be achieved with moderate effort and $F > 90\%$ seems possible in the long run.

Note that some experimental imperfections are beyond the present scope. Examples of such imperfections are laser phase noise, atom number fluctuations, and the imperfect single-qubit visibility, which was observed in Ref. [133] without clearly identifying its physical origin.

### 2.7.1 Simplifications to the Model

Studying how the gate performance depends on the pulse shape of the photons is beyond the scope of this work. Hence, we choose a specific envelope $u_c(t) = u_s(t, T_c)$ for the control and $u_t(t) = u_s(t - T_c, T_t)$ for the target pulse, where $u_s(t, T)$ is a single-cycle sinusoid of the form

$$u_s(t,T) = \sqrt{\frac{2}{T}} \sin\left(\frac{\pi}{T}t\right) \times \begin{cases} 1, & 0 \leq t \leq T \\ 0, & \text{otherwise.} \end{cases} \tag{2.79}$$

This looks very similar to a Gaussian near the peak but, in contrast, does not have infinitely long tails, which would be problematic as we require finite length pulses.

For the purpose of the calculation, we would like to simplify our model of Rydberg blockade from App. B. To this end, we note that atoms outside the blockaded region still contribute to the overall optical depth of the medium, increasing the conditional pulse delay and making it harder to achieve high cavity EIT reflectivity $|\mathcal{R}|^2$. Hence, a superatom geometry is advantageous, in which all atoms experience perfect blockade regardless of which atom carries the Rydberg excitation. This is fulfilled if the size of the atomic ensemble is smaller than the blockade radius such that $R_{k\ell} < R_b$ for all atoms. In this situation, Eq. (B.29) yields $\alpha_{k\ell} \approx \alpha_{\text{2level}}$. Using Eqs. (B.23), (B.24), and (B.30), we find

$$\mathcal{R}_b = \sum_{k=1}^{N} |\alpha_k|^2 \mathcal{R}_k = -1 + \frac{2\beta}{1 + C_{\text{eff,b}} - i\Delta_c/\kappa} \tag{2.80}$$

with

$$C_{\text{eff,b}} = C \frac{\Gamma_e}{\Gamma_e - 2i\Delta_s}. \tag{2.81}$$

As another simplification, we assume resonant light fields $\Delta_c = \Delta_s = \Delta_{\text{co}} = 0$. We note that it is possible to choose nonzero detunings and still obtain a $\pi$ phase shift between Eqs. (2.80) and (2.32). Therefore, assuming resonant light fields is not strictly required to obtain a quantum-logic gate. However, lifting this assumption in our numerical optimization did not lead to a clearly improved fidelity but made the system more susceptible to variations in the number of atoms.

### 2.7.2 Choice of Free Parameters

The goal of our numerical calculation is to find experimental parameters which maximize the fidelity $F$ from Eq. (2.71). To this end, we choose a set of fixed parameters and vary all remaining input parameters. In essence, the four free parameters for this optimization are the duration $T_c$ and $T_t$ of the control and target light pulses, the reflectivity of the I/O coupler characterized by $\mathcal{F}_{\text{in}}$, and the resonant optical depth of the atomic medium $d_t$. This choice of free parameters is motivated by the following three major trade-offs.

- The decay of the control retrieval efficiency according to Eq. (2.54) favors short light pulses, while long light pulses are desirable to avoid a reduction of the storage and retrieval efficiency due to non-adiabatic effects and to avoid a reduction of $F$ due to the conditional target pulse delay.

- Low cooperativity $C \propto d_t \mathcal{F}_{\text{in}}$ enables high cavity EIT reflectivity $|\mathcal{R}|^2$ and small target pulse delay, while high cooperativity is desirable to achieve high reflectivity $|\mathcal{R}_b|^2$ in the presence of Rydberg blockade.
- Low cavity finesse $\mathcal{F}_{\text{in}}$ reduces the impact of imperfect HR cavity mirrors, while high cavity finesse reduces losses when the cavity is blockaded.

### 2.7.3 Fixed Parameters

For the choice of the cavity parameters $\mathcal{F}_H$ and $\Delta\omega_{\text{ax}}$, two considerations are particularly important. First, to avoid losses at the HR cavity mirrors, these should have the highest possible reflectivity, such that $\mathcal{F}_H \gg \mathcal{F}_{\text{in}}$. Second, a large cavity EIT linewidth $\kappa_F$ is desirable, because the incoming light pulses need to spectrally fit into this linewidth to avoid a reduction of the storage and retrieval efficiency due to non-adiabatic effects and to keep the conditional target pulse delay small. According to Eq. (2.43), the cavity linewidth $\kappa$ constitutes an upper bound for $\kappa_F$, so $\kappa$ should be large. At a given finesse $\mathcal{F}_{\text{in}}$, this implies making $\Delta\omega_{\text{ax}}$ as large as possible. For technical reasons discussed in Sec. 3.2, we achieve the numbers in Tab. 2.1.

When aiming at large $\kappa_F$, one should also make $\Omega_{\text{co}}$ large according to Eq. (2.43). Technical limitations such as available laser power make a value of $\Omega_{\text{co,max}}/2\pi = 20\,\text{MHz}$ seem realistic, as achieved in Ref. [152]. Hence, we choose $|\Omega_{\text{co}}| = \Omega_{\text{co,max}}$ for the target photon. For the control photon, it is a known problem that $\Omega_{\text{co}}(t)$ from Eqs. (2.50) and (2.52) diverges at the beginning of storage and at the end of retrieval [46]. Hence, we clip $|\Omega_{\text{co}}(t)|$ to a maximum value $|\Omega_{\text{co}}(t)| \leq \Omega_{\text{co,max}}$. This turns out to have little effect on the achieved storage and retrieval efficiency, just as in Ref. [46].

The transmission $\eta_{\text{delay}}$ through the delay fiber depends on the length of the fiber and the required delay. At a signal light wavelength of 780 nm, optical fibers with a loss of $-4.3\,\frac{\text{dB}}{\text{km}}$ are commercially available. This corresponds to $\eta_{\text{delay}} = \exp(-\alpha_f L_f)$ where $L_f$ is the length of the delay fiber and where the attenuation coefficient is $\alpha_f = \frac{1}{10}\ln(10) \times 4.3\,\text{km}^{-1}$. With a refractive index of $n_f = 1.5$ in the delay fiber, the fiber length must correspond to the total delay $T_c + T_t$. Hence $L_f = (T_c + T_t)c/n_f$ and

$$\eta_{\text{delay}} = e^{-\gamma_f (T_c + T_t)} \tag{2.82}$$

with $\gamma_f = \alpha_f c/n_f = 1/(5.0\,\mu\text{s})$. Compared to the delay fiber, losses at the remaining optical elements outside the cavity, such as beam splitters, waveplates, and mirrors, are expected to be negligible. Hence, we use $c_H = \sqrt{\eta_{sr}}$, $c_V = \sqrt{\eta_{\text{delay}}}$, and $t_H = t_V = 1$.

The dephasing rate $\gamma_{rg}$ causes exponential decay of the overall write-read efficiency during the dark time $t_{\text{dark}}$ according to Eq. (2.53). Hence, $t_{\text{dark}}$ should be kept as short as possible. This implies $t_{\text{dark}} = T_t$. Similarly, the coherence time $1/\gamma_{rg}$ between the atomic ground and Rydberg states should be as long as possible. To achieve this, the temperature of the atomic ensemble has to be low and the optical dipole trap should either be operated at suitable parameters or it should be turned off completely during the experiment [133]. Moreover, the atomic density should not be too high because otherwise increased dephasing may occur, originating from the interaction between the Rydberg electron and nearby ground-state atoms [7, 98]. As a reference point, Ref. [133] found experimentally that this

| | | |
|---|---|---|
| **Fixed input parameters:** | | |
| $1/\Gamma_e = 26\,\mathrm{ns}$ | $1/\gamma_{rg} = 30\,\mu\mathrm{s}$ | $1/\gamma_f = 5\,\mu\mathrm{s}$ |
| $\Delta\omega_{\mathrm{ax}}/2\pi = 1.5\,\mathrm{GHz}$ | $\Omega_{\mathrm{co,max}}/2\pi = 20\,\mathrm{MHz}$ | $\mathcal{F}_H = 2 \times 10^4$ |
| **Main optimization results:** | | |
| $F = 0.64$ | $F_{\mathrm{post}} = 0.94$ | $\eta = 0.68$ |
| **Optimized free input parameters:** | | |
| $\mathcal{F}_{\mathrm{in}} = 230$ | $T_c = 0.5\,\mu\mathrm{s}$ | $T_t = 1.0\,\mu\mathrm{s}$ |
| **Other parameters at the optimum:** | | |
| $C = 11$ | $\beta = 0.989$ | $\mathcal{C}_c = 0.993$ |
| $\lvert\mathcal{R}\rvert^2 = 0.95$ | $\lvert\mathcal{R}_b\rvert^2 = 0.69$ | $\eta_{sr} = 0.76$ |
| $\eta_{sr,\mathrm{ad}} = 0.81$ | $\eta_{\mathrm{dark}} = 0.999$ | $\eta_{\mathrm{delay}} = 0.74$ |

**Table 2.1:** Input parameters and results of the numerical optimization. The values of $|\mathcal{R}|^2$ and $|\mathcal{R}_b|^2$ quoted here are for monochromatic resonant light.

kind of dephasing vanishes in $^{87}$Rb below a peak density on the order of $\varrho = 1 \times 10^{11}\,\mathrm{cm}^{-3}$ for principal quantum numbers below 80, resulting in a coherence time of $1/\gamma_{rg} = 30\,\mu\mathrm{s}$ at a temperature of $0.2\,\mu\mathrm{K}$. To avoid limitations on the achievable optical depth at low atomic density, it is advantageous to use an atomic transition that features a large absorption cross section $\sigma_{\mathrm{abs}}$. In $^{87}$Rb, an obvious choice is the cycling transition on the $D_2$ line at 780 nm with $1/\Gamma_e = 26\,\mathrm{ns}$ and $\sigma_{\mathrm{abs}} = 2.9 \times 10^{-9}\,\mathrm{cm}^2$.

In addition to using low density, one can reduce the probability of ground-state atoms interacting with the Rydberg electron by using Rydberg states with relatively low principal quantum numbers, for which the wave function of the Rydberg electron extends over a smaller volume compared to high principal quantum numbers. To obtain a large Rydberg-Rydberg interaction at low principal quantum numbers, it is advantageous to employ a Rydberg state pair that features a Förster resonance, such as the pair $|48^2S_{1/2},50^2S_{1/2}\rangle$ introduced in Sec. 2.2.

### 2.7.4 Numerical Optimization

We use the following approach to calculate the fidelity $F$ as a function of the free parameters $T_c$, $T_t$, $\mathcal{F}_{\mathrm{in}}$, and $d_t$. First, we numerically solve Eqs. (2.45)–(2.48), (2.50), and (2.52) with $t_{\mathrm{dark}} = T_t$ to obtain $\eta_{sr}$ and $\mathcal{C}_c$. Next, we use Eqs. (2.31), (2.2), (2.80), (2.81), (2.82), (2.72)–(2.74), and (2.77) to calculate $t_a$, $\mathcal{R}$, $\mathcal{R}_b$, $\eta_{\mathrm{delay}}$, $F_p(\omega)$, and $\eta(\omega)$. Finally, we numerically solve the integrals in Eqs. (2.71) and (2.76) to obtain $F$ and $\eta$.

A frequent problem with this strategy is that the optimal value for the optical depth $d_t$ is typically not much smaller than unity but rather somewhere above 2. This is problematic for two reasons. First, the model of Eqs. (2.45)–(2.48) becomes a poor approximation and, second, the high optical depth will tend to increase dephasing due to the required higher atomic density. For these reasons, we typically restrict the optical depth in the numerical optimization to $d_t \leq 0.3$ and unsurprisingly find that the maximum of $F$ subject to this

constraint is found at

$$d_t = 0.3. \tag{2.83}$$

Tab. 2.1 shows the results of the numeric optimization. Before discussing the origin of the infidelity, we first note that $\sqrt{C\Gamma_e/2\kappa} = 6.4$ shows that this parameter regime is not in the bad-cavity limit. Nonetheless, in Tab. 2.1, $\eta_{sr}$ deviates only moderately from $\eta_{sr,\mathrm{ad}}$ and $\mathcal{C}_c$ hardly deviates from 1. From this, we conclude that using the control coupling envelopes from Eqs. (2.50) and (2.52) is still a good approximation to the optimal control problem, despite some lack of adiabaticity.

We now discuss the origin of the infidelity. First, we note that $\mathcal{C}_c \approx 1$, which means that $F_p(\omega)$ in Eq. (2.71) is well approximated by $F(\omega)$ in Eq. (2.70). Next, we note that $\eta_{sr}$ and $\eta_{\mathrm{delay}}$ happen to be almost identical. Hence, $\eta_{sr} \approx \eta_{\mathrm{delay}}$ can be factored out of $F(\omega)$ in Eq. (2.70) and out of $\eta(\omega)$ in Eq. (2.77). Hence, $\eta_{sr}$ and $\eta_{\mathrm{delay}}$ in Tab. 2.1 are easily identified as the largest sources of the infidelity because all remaining effects together contribute only a factor 0.85 to $F$ and 0.91 to $\eta$.

To understand what limits $\eta_{sr}$, we note that $\eta_{sr}$ does not deviate much from $\eta_{sr,\mathrm{ad}}$ and consider the decomposition of $\eta_{sr}$ in Eq. (2.54). As $\eta_{\mathrm{dark}}$ is negligible, the dominant problem lies in the fact that $C$ is not larger.

It is a natural question to ask why the optimization does not find a better overall performance at larger $C$, which at fixed $d_t$ and $\mathcal{F}_H$ is equivalent to larger $\mathcal{F}_{\mathrm{in}}$. The answer is that while this would obviously increase $\eta_{sr,\mathrm{ad}}$ and according to Eqs. (2.80) and (2.81) also $\mathcal{R}_b$, such an increase in $C$ would also decrease the ratio $\eta_{sr}/\eta_{sr,\mathrm{ad}}$ and it would decrease the cavity EIT bandwidth $\kappa_F$ so that the unwanted conditional target pulse delay would be increased. This would result in an overall decrease of $F$.

It turns out that higher fidelity at larger $C$ is possible, if longer pulses are used such that non-adiabatic effects and conditional pulse delay become less severe. This requires a longer coherence time $1/\gamma_{rg}$. If dephasing can be overcome, the ultimate limit for $\gamma_{rg}$ is set by the radiative $1/e$ lifetime of the Rydberg states. For example, for a principal quantum number around 70 in rubidium in a room-temperature environment, this yields $\gamma_{rg} \approx 140\,\mu\mathrm{s}$, see e.g. Ref. [150]. Along with this, we assume that the delay fiber is replaced by storage and retrieval in a copy of the atom-cavity system. This copy, however, serves only as a quantum memory without any need for Rydberg blockade. Hence, one can realize much larger $C$ simply by increasing the length of the medium, without increasing its density. Hence, we approximate this quantum memory as $\eta_{\mathrm{delay}} = 1$. We also remove the constraint on $d_t$. All other parameters in Tab. 2.1 are left unchanged. A numerical optimization of $F$ yields $d_t = 5$, $\mathcal{F}_{\mathrm{in}} = 100$, $T_c = 3\,\mu\mathrm{s}$, $T_t = 14\,\mu\mathrm{s}$, $F = 0.935$, and $\eta = 0.941$. If these numbers can be achieved in the future, this would be a tremendous step forward for optical quantum information processing.

# Chapter 3

# Experimental Setup

The experiments in this work were performed at the Max Planck Institute of Quantum Optics in a laboratory, which was previously used for experiments with Bose-Einstein condensates (BECs) [94, 135]. In recent years, ultracold atomic ensembles above the critical BEC temperature were employed to study Rydberg EIT at the single-photon level [8, 132, 149]. As a consequence, substantial parts of the setup required for this work, such as laser systems and experiment control software and hardware, were already present in the lab. However, the previous vacuum chamber did not offer enough room to house the cavity, so a new vacuum system had to be installed along with the optical resonator. As a consequence, new setups for preparation and characterization of the atomic ensemble had to be designed and implemented. This required removing most of the components on the main part of the optical table, see Fig. 3.1.

This chapter starts with an overview of the new setup in Sec. 3.1. Subsequently, the design of the optical resonator is discussed in Sec. 3.2. Sec. 3.3 describes the vacuum chamber along with the viewports and the bake-out process. The electric field control and particle detection capabilities of the new setup are covered in Secs. 3.4 and 3.5. Sec. 3.6 gives an overview of the laser systems. Finally, Sec. 3.7 explains how the optical setup required for the scheme in Fig. 2.3 is implemented in the experiment.

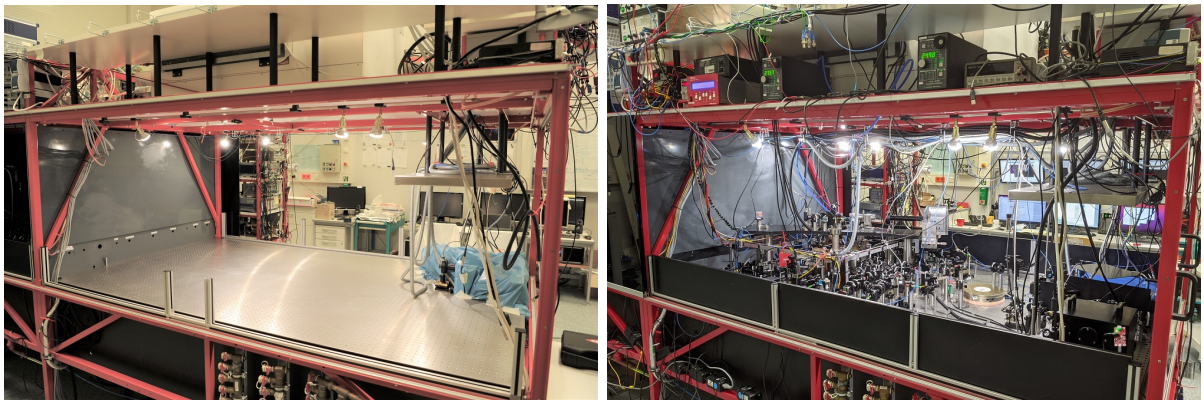

**Figure 3.1:** Photos of the main part of the optical table taken in April 2020 (left) and in June 2021 (right).

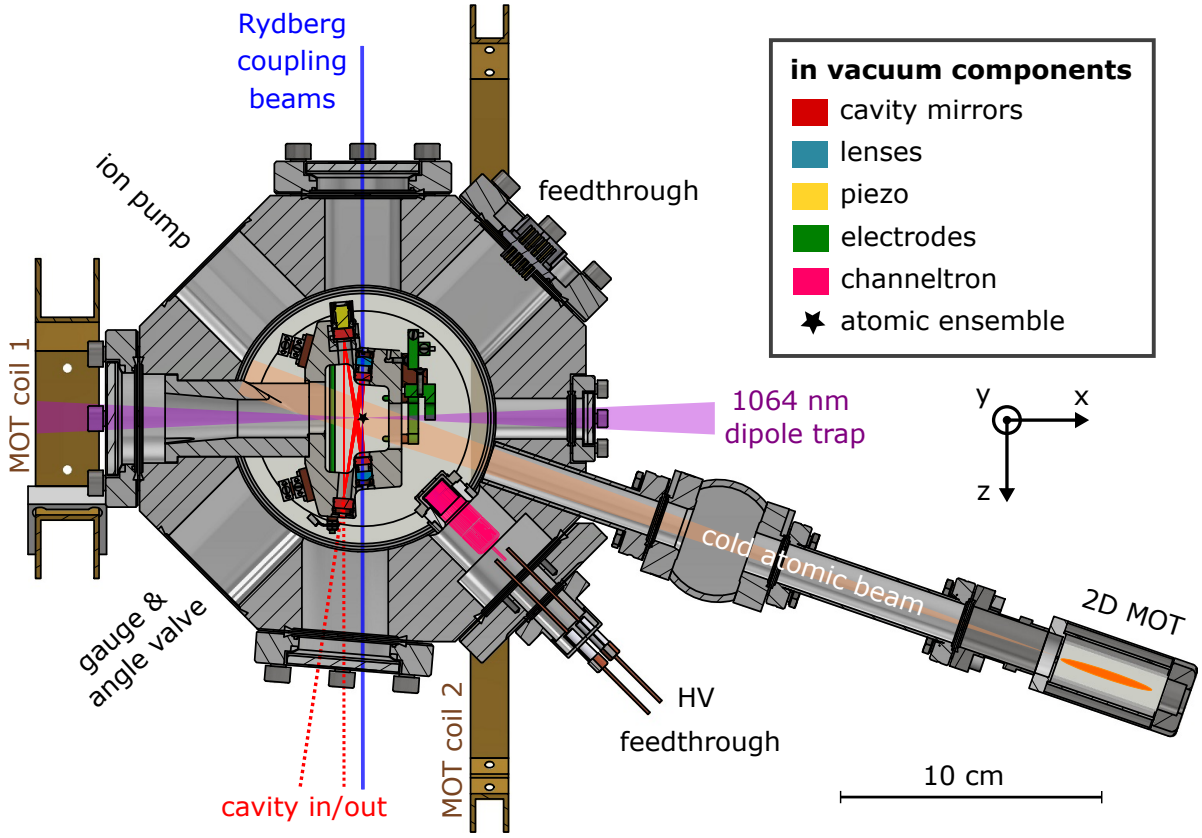


**Figure 3.2:** Schematic overview of the experimental setup. The drawing is a horizontal cut through the CAD design of the vacuum chamber in the atomic plane. The ion pump and vacuum components connecting the chamber to a vacuum gauge and to an angle valve for initial evacuation are omitted. Further details are provided in the text.

## 3.1 Overview

Fig. 3.2 shows a horizontal cut through the vacuum system. The following key ideas motivated this design. First, we wanted to decrease the cycle time for the preparation of an atomic ensemble compared to the previous setup by using a two-dimensional magneto-optical trap (2D MOT) [23] and by employing a fast laser-cooling method [159] instead of comparatively slow evaporative cooling in a magnetic trap. Second, high $^{87}$Rb vapor pressure in the main chamber is avoided in order to obtain long trapping times and to rule out deposition of $^{87}$Rb on the cavity mirrors. Third, a compact main vacuum chamber combined with large DN100CF viewports at the top and bottom allow for relatively good optical access.

Preparation of an atomic ensemble starts with a 2D MOT in a commercial cell (Cold Quanta, CASC-1000-RB) which contains two rubidium dispensers. Four permanent magnet rods (not drawn) generate the magnetic field gradient required for the 2D MOT. The cell is connected to the main chamber via an all-metal gate valve (VAT Vakuumventile, 48124-CE01, custom made with magnetic permeability below 1.05), such that the cell

can be exchanged while keeping the rest of the system under vacuum, avoiding a full bake-out. The cold atomic beam emerging from the 2D MOT passes through a small vacuum aperture with a diameter of 0.75 mm, which prevents excessive entry of $^{87}$Rb into the main chamber and which is integrated into the 2D MOT cell. Subsequently, atoms are collected in a standard three-dimensional MOT (3D MOT) at the center of the main chamber, which coincides with the mode waist of the optical resonator and is located approximately 30 cm from the 2D MOT. Atoms that are not captured in the 3D MOT can pass through a hole in the resonator mount toward the ion pump. This avoids accumulation of atoms inside the resonator mount where they could potentially end up on the cavity mirrors. Two water cooled coils outside the vacuum generate the magnetic field gradient required for the 3D MOT.

The 3D MOT overlaps with a crossed-beam optical dipole trap (ODT) with a wavelength of 1064 nm, into which atoms are continuously cooled by the MOT. Only one of the two ODT beams is drawn in Fig. 3.2, the other beam is perpendicular to the drawing plane. The atom number of the atomic ensemble in the ODT is optimized by a final 3D MOT cooling stage with reduced repumping power. Next, the magnetic field is switched off and polarization gradient cooling reduces the atomic temperature. Subsequently, the MOT light is switched off and further cooling in the ODT is achieved using the first two stages of Raman cooling described in Ref. [159] but in a crossed-beam ODT. Lowering the power of the ODT after the Raman cooling further reduces the atomic temperature, yielding a suitably prepared ensemble for the experiment. The atomic ensemble can be imaged along the vertical axis using an absorption imaging system described in Ref. [126].

The light fields containing the control and the target photon are coupled into the resonator through a DN40CF viewport at the side of the vacuum chamber. The resonator mirrors are held in a monolithic titanium mount, which is firmly attached to the wall of the chamber via an aluminum bridge. One of the mirrors is glued to a piezoelectric actuator (piezo) which is used to adjust the cavity resonance frequency.

The Rydberg coupling light at 480 nm exits from a fiber coupler (Schäfter+Kirchhoff, 60FC-4-M12-33) with a spot size of approximately 750 µm. The control (target) coupling light passes through a PBS for polarization cleaning and through a telescope consisting of two spherical singlet lenses with focal lengths of 150 mm and −50 mm (−100 mm), before it enters the vacuum chamber. To focus the coupling light onto the atomic ensemble, plano-convex lenses (Newport, KPX016AR.14), which are AR coated for 430 nm to 700 nm and have a focal length of 19 mm, are positioned behind the concave cavity mirrors, as shown in Figs. 3.2 and 3.6. Initial alignment of the coupling beams is achieved by coupling resonant signal light into the cavity and then superimposing the coupling beam with the signal light transmitted through one of the concave cavity mirrors. The spot size of the coupling light at the atomic position is fine-adjusted by translating one of the lenses along the optical axis such that a large EIT Rabi frequency is observed in the EIT spectra in Sec. 5.2.

To provide electric field control capabilities, the resonator mount contains several electrodes, which are insulated from the cavity mount with Vespel parts. Kapton insulated wires, which are not drawn in Fig. 3.2, connect the electrodes to an electric feed-through flange. By applying an electric field, Rydberg atoms can be ionized and the resulting ions or electrons can be detected using a channel electron multiplier (channeltron). To avoid

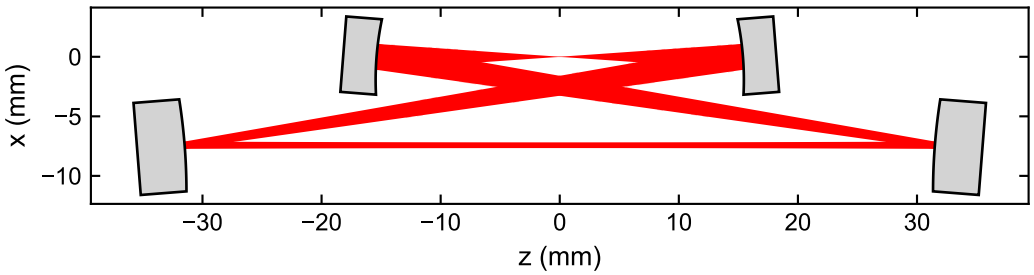


**Figure 3.3:** Calculated fundamental cavity mode (red) in the tangential plane. The colored area contains 99.999% of the power. The design is symmetric with respect to the $x$-axis. The distance between the concave (convex) cavity mirrors is 30.75 mm (63.00 mm) and their radius of curvature is −25 mm (50 mm). The angle of incidence is 4.5°. All mirror centers lie in the $(x,z)$-plane. The round-trip length of the resonator is 188.7 mm, resulting in an axial mode spacing of 1.59 GHz. The cavity waist $w_c = 8.5\,\mu\text{m}$ and the atomic ensemble are located at $(x,z) = (0,0)$. For the D2 line of $^{87}$Rb, this yields an atom-cavity coupling constant of $g/2\pi = 1.0\,\text{MHz}$ according to Eq. (2.34). The cavity mode has an additional waist midway between the convex mirrors which is slightly astigmatic and has a spot size of 0.10 mm (0.12 mm) in the tangential (sagittal) plane.

stray electric fields from the required high voltage (HV) and to avoid compromising optical access, the channeltron does not have a direct line-of-sight to the atomic position. Hence, ions or electrons have to be steered towards the channeltron by an additional deflection electrode. More details are provided in Sec. 3.4.

## 3.2 Optical Resonator Design

The optical resonator constitutes the core of the experimental setup. Modifying it becomes difficult once the vacuum system is closed, so careful design is critical. As discussed in Sec. 2.7, high gate performance requires low intra-cavity loss and a large axial mode spacing. These requirements are reflected in many of the design choices discussed below.

### 3.2.1 Resonator Geometry

We first explain, why a bow-tie resonator geometry is favorable. As discussed in Refs. [8, 68, 133, 173], the thermal atomic motion causes a decay of the retrieval efficiency of the stored control photon according to

$$\eta_{sr} \propto \exp(-t^2/\tau_R^2), \qquad \tau_R = \frac{1}{k_R \sigma_v}, \qquad \sigma_v = \sqrt{k_B T/m}, \tag{3.1}$$

where $k_B$ is the Boltzmann constant, $T$ is the atomic temperature, $m$ is the atomic mass, and $\hbar k_R$ is the net photon recoil transferred during storage of the control photon. In

order to obtain long coherence time, $k_R$ should be minimal. In our atomic excitation scheme, this is achieved for counter-propagating signal and coupling light fields. This requirement rules out the use of a standing-wave resonator, such as a Fabry-Pérot cavity, in which there are two counter-propagating components of the signal light field. While one can achieve minimal $k_R$ for one of these components, the other component would always have maximal $k_R$, yielding fast decay of the retrieval efficiency. Hence, we use a traveling-wave cavity, i.e. a ring resonator. In principle, a configuration with three instead of four mirrors might seem like a good choice because every mirror introduces additional intra-cavity loss. However, such a three-mirror resonator does not allow for a small angle of incidence, which is favorable because this reduces astigmatism and facilitates a small polarization mode splitting. The latter is because differential reflection phase shifts between s- and p-polarization tend to be smaller for a small angle of incidence. Hence, we chose a bow-tie geometry and send the coupling light through the concave cavity mirrors to achieve minimal $k_R$, see Fig. 3.2.

We experimentally tested several different geometries in order to find a configuration that simultaneously yields small mode waist, low intra-cavity loss, and small polarization mode splitting. A small mode waist is beneficial because this increases $g$ according to Eq. (2.34), which decreases the number of atoms required to reach a given collective cooperativity. Some of the early geometries and details about the methods used for designing and characterizing these resonators can be found in Ref. [64]. Fig. 3.3 shows the geometry of the final resonator, which is installed in our vacuum chamber, along with the calculated fundamental resonator eigenmode. For a planar resonator, the transverse resonator eigenmode can be separated into two components: the transverse component that lies in the resonator plane (tangential plane) and the transverse component perpendicular to the resonator plane (sagittal plane). For each of these components, the eigenmode is defined as the mode that reproduces itself after one round trip through the resonator. If such a mode exists for both components, the resonator is stable, see chapter 19 in Ref. [141]. Details about how to calculate resonator eigenmodes using the ABCD or ray-transfer matrix formalism can be found in Refs. [38, 64, 141].

Our design represents a compromise between a small angle of incidence and avoiding mode clipping. Clipping can occur due to the finite aperture of the concave mirrors or at the side of the concave mirror substrates when the beam travels between the concave and convex mirrors. While the use of concave mirrors is necessary to obtain a stable resonator, the additional use of two convex mirrors allows for a shorter cavity, which increases $\Delta\omega_{\mathrm{ax}}$.

As pointed out in the supplement of Ref. [69], which uses a similar resonator design, it is important to keep a distance on the order of 10 mm between the atomic position and the nearest surface. This reduces uncontrolled stray electric fields presumably resulting from patch charges on surfaces, which could otherwise cause an increased dephasing rate $\gamma_{rg}$. Hence, we chose a radius of curvature of $-25$ mm for the concave mirrors, which leads to a distance of approximately 15 mm between the atoms and the nearest mirror surface.

### 3.2.2 Mirrors

To obtain low intra-cavity loss, high-quality mirrors are required. Our cavity mirrors were manufactured and coated by LAYERTEC, polished to a specified root mean square (RMS) surface roughness below 0.3 nm.

The design goal for the HR cavity mirror coatings was a reflectivity of $> 99.99\%$, a transmission of 10 ppm, and a differential phase shift between the reflected s- and p-polarized components of $\Delta\varphi_{s-p} < 0.1°$ (zero-phase mirror). Unless otherwise noted, the stated numbers refer to a wavelength of 780 nm under 4.5° angle of incidence. A ring-down measurement with four HR mirrors from the same coating run yielded a decay time of 2.0 µs, corresponding to a finesse of $\mathcal{F}_H = 2 \times 10^4$ which translates to a reflectivity of 99.992% per mirror. To achieve these numbers, it was crucial to clean the reflecting mirror surfaces before mounting the substrates. The best cleaning results were obtained with a cleaning polymer (Mountain Photonics, FirstContact). Regularly verifying the results under a dark-field microscope was helpful to optimize the cleaning technique.

While the achieved numbers are sufficient for the experiment, it should be noted that state-of-the-art HR mirrors achieve reflectivities above 99.999%. This becomes possible by manufacturing extremely precise mirror surfaces, using e.g. superpolishing. Although this is difficult on substrates with a small radius of curvature, Ref. [158] recently demonstrated just that. The authors report on a near-concentric Fabry-Pérot cavity consisting of two mirrors with 10 mm radius of curvature, an RMS microroughness of 0.10 nm, and losses of 5 ppm at 1064 nm. This promises significant potential for future improvements of $\mathcal{F}_H$ in our gate scheme.

The coating design for the I/O coupler has a reflectivity of 98.2% and a differential reflection phase shift of $\Delta\varphi_{s-p} = 0.1°$. We decided against a zero-phase mirror because this would have increased the tolerances on the reflectivity according to the manufacturer. Assuming perfect HR mirrors, these numbers result in an expected finesse of $\mathcal{F} = 349$, a full width at half maximum (FWHM) linewidth of $2\kappa = 4.6\,\mathrm{MHz}$ and an expected splitting between the polarization eigenmodes of the resonator of $\Delta\omega_{\mathrm{pol}} = \Delta\omega_{\mathrm{ax}}\Delta\varphi_{s-p}/2\pi = 2\pi \times 0.4\,\mathrm{MHz} \ll 2\kappa$.

The backsides of all mirror substrates are plane polished and anti-reflection (AR) coated for 780 nm and 480 nm. This avoids etalon effects for the coupling light at 480 nm, which has to pass through the concave mirrors, see Fig. 3.2. At 480 nm, the HR coatings have a reflectivity of 10%, while the I/O coupler coating is designed for a reflectivity below 1%. This suppresses a cavity mode at this wavelength.

### 3.2.3 Alignment

The four cavity mirrors need to be positioned in space according to the design in Fig. 3.3. To get an impression of the required positioning accuracy, we study the effect of mirror displacements in the $x$-, $y$-, and $z$-direction onto the resulting cavity eigenmode.

First, we consider the position of the optical axis of the cavity eigenmode. The optical axis is a ray defined by the requirement that it reproduces itself after one round trip through the resonator, governed by reflections at each mirror surface according to Snell's law. Ideally, the optical axis touches the center of each mirror. However, displacing or

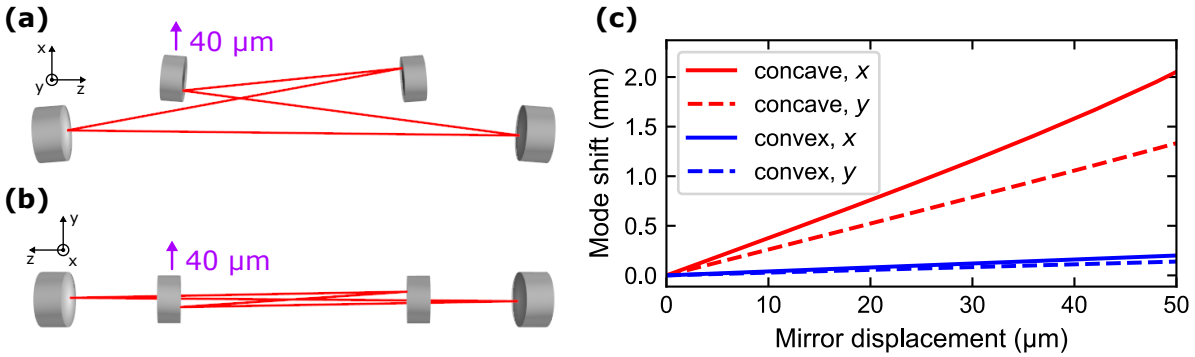


**Figure 3.4:** Impact of mirror displacement onto cavity eigenmode position. Moving one of the concave mirrors by just 40 µm in the $x$- (a) or $y$-direction (b) leads to a large shift of the optical axis (red) of the cavity eigenmode. (c) plot of the mode shift, defined as the distance between the center of one of the concave mirrors and the point at which the optical axis touches the mirror surface. The shift is large if one of the concave mirrors is displaced (red) and small for a displacement of the convex mirrors (blue). For each type of mirror, displacements along the $x$-axis (solid) have a larger impact than along the $y$-axis (dashed).

tilting one of the mirrors shifts the optical axis toward the mirror edges. We numerically calculate this shift using geometric ray tracing. As an example, we study the effect of mirror displacements in Fig. 3.4. Parts (a) and (b) illustrate the mode shift for a displacement of one of the concave mirrors along the $x$- and $y$-direction. Note that the optical axis stays in the $x$-$z$-plane in (a) but follows a nonplanar path in (b).[1] As shown in Fig. 3.4 (c) shifting a concave mirror has a much larger effect than shifting a convex mirror. In comparison, shifts below 50 µm along the $z$-direction have a negligible effect for all mirrors.

However, larger shifts along the $z$-direction can lead to strong astigmatism or even an unstable resonator. To study this, we consider changes of the distance between the two concave or convex mirrors, while keeping the alignment ideal and the angle of incidence constant. This is illustrated in Fig. 3.5. Again, the requirements for the concave mirrors are more stringent than for the convex mirrors. The region of stability has a width of about 0.9 mm and 16.6 mm, respectively. Close to the edge of the stable region, the mode becomes highly astigmatic.

Fig. 3.6 shows how the resonator mirrors are aligned in the experimental setup. Three of the mirrors are positioned in fitting holes inside a monolithic titanium mount. Titanium is chosen as a material because it is nonmagnetic and compatible with ultra-high vacuum. The resonator mount was manufactured using a five-axis CNC milling machine that typically achieves a precision of 20 µm. The features relevant for positioning the cavity mirrors were milled in a single setup. The fourth resonator mirror is glued[2] onto a piezo

[1] In Fig. 3.4 (a), the mode shift is along the $x$-axis because the mode cannot leave the $x$-$z$-plane for reasons of symmetry. Although we did not find a similar argument for (b), our calculation shows that the mode shift is predominantly along the $y$-axis in this case.

[2] We picked a high-temperature epoxy (Thorlabs, 353NDPK) for glueing, using a temperature ramp with 25 °C steps of 20 min each from 25 °C to 150 °C and back.

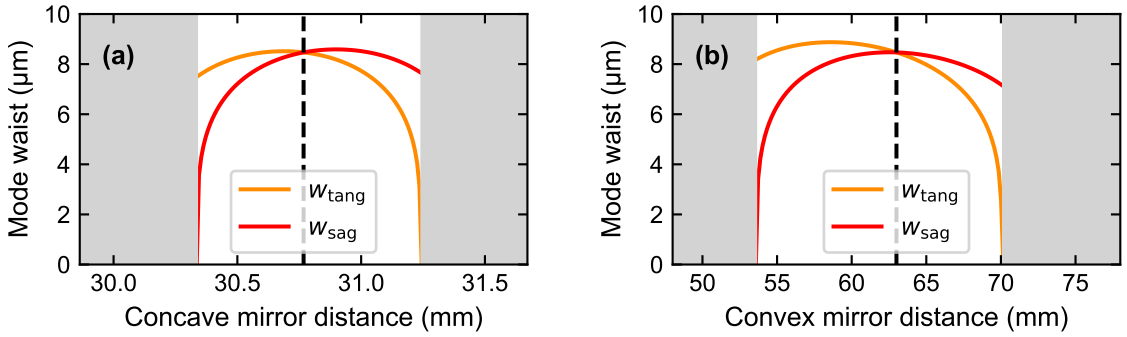


**Figure 3.5:** Stability of the optical resonator design. The plots show the calculated mode waist in the sagittal and tangential plane as a function of the distance between the concave (a) and convex (b) cavity mirrors. In the gray shaded regions, the resonator is unstable. Vertical dashed lines mark our target design.

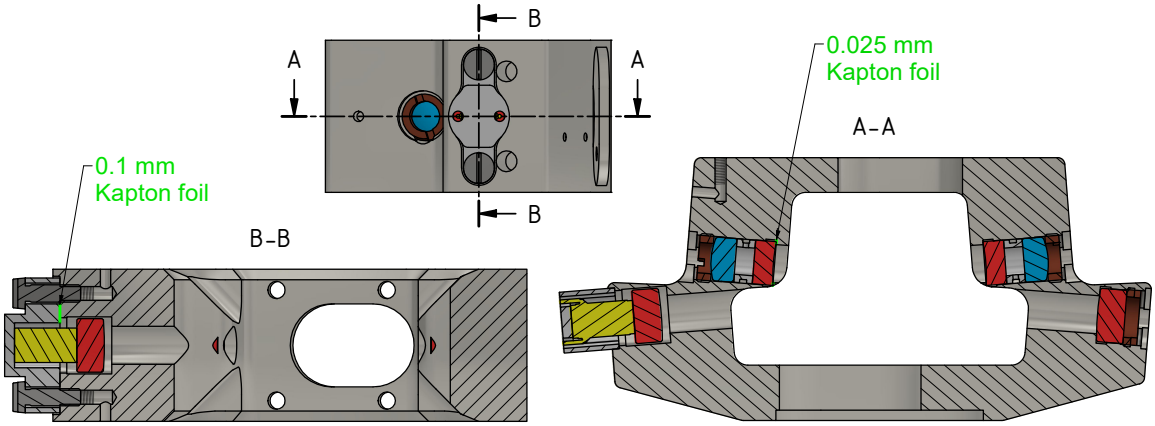


**Figure 3.6:** Alignment of the cavity. Shown is a technical drawing of the cavity mount consisting of a side view (top) and two cuts along the indicated axes A-A and B-B. Resonator mirrors are drawn in red. Three mirrors are positioned in fitting holes and fastened with Vespel retaining rings (dark brown). Two lenses (blue), which focus the EIT coupling light onto the atomic ensemble, are placed behind the concave mirrors. Spacer rings ensure the correct working distance to the atomic position. The fourth resonator mirror is glued onto a piezo (yellow). Fine alignment of the resonator is achieved by inserting pieces of thin Kapton foil (green) between one of the conave mirrors and the cavity mount and between the piezo cap and the cavity mount.

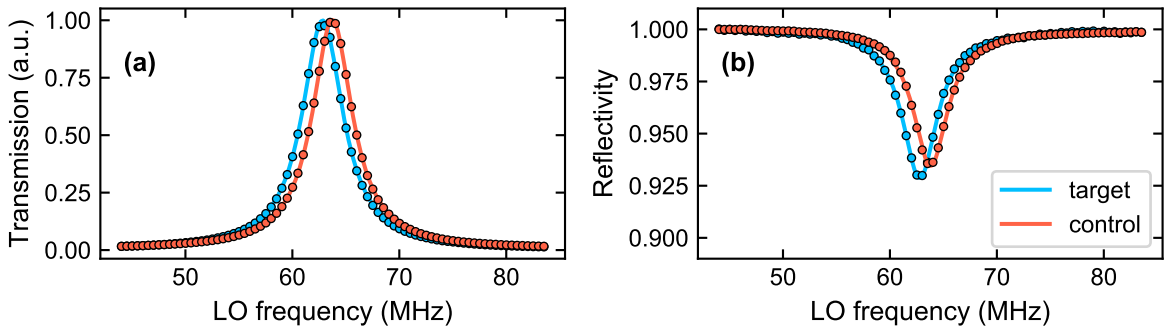


**Figure 3.7:** Transmission (a) and reflectivity (b) of the cavity for the control (red) and target (blue) beam path. These data were taken with the cavity inside the vacuum chamber after bake-out. The signal laser frequency is varied by ramping the frequency of a radio-frequency local oscillator (LO) which determines the set point of the laser lock. Lines are Lorentzian fits to the data points.

(PI Ceramic, PICMA P-885.10 piezo stack actuator, dimensions $5 \times 5 \times 9$mm, 6.5 µm travel at 100 V), the backside of which is glued onto an aluminum cap. The outer contour of the cap is matched to a fitting hole in the cavity mount. To achieve accurate alignment of the piezo mirror relative to the cap, a glueing mask with a fitting hole was used.

After mounting the mirrors, the position of the cavity mode was determined by coupling a laser beam into the resonator with high mode matching efficiency and looking at the direction of the incoming beam relative to the resonator mount. It turned out that the resonator eigenmode was shifted in $x$- and $y$-direction similar to Fig. 3.4 (a) and (b). The nonplanarity of the eigenmode due to the shift in $y$-direction contributed to an overall polarization mode splitting of about 4 MHz. This increased polarization mode splitting is due to a round-trip geometrical polarization rotation, see Ref. [70]. To reduce the mode shift, pieces of thin Kapton foil were inserted in front of one of the concave mirrors and between the piezo cap and the cavity mount, as indicated in Fig. 3.6. After several iterations, an almost centered cavity mode was obtained with a polarization mode splitting of just 0.3 MHz.

### 3.2.4 Characterization

After assembly and bake-out of the resonator inside the vacuum system, we couple signal light into the resonator with high mode matching efficiency, see Sec. 3.2.5, and observe the reflected and transmitted light using photodetectors. The resonator length is stabilized during these measurements using the technique described in Sec. 3.7.1.

Fig. 3.7 shows the obtained signals. Lorentzian fits to the transmission data yield a FWHM cavity linewidth $2\kappa = 4.534(5)$ MHz ($2\kappa = 4.659(14)$ MHz) for the control (target) path, resulting in an average finesse of $\mathcal{F} = 346$. This agrees well with the specifications of the I/O coupler coating. The polarization eigenmode splitting is 0.915(4) MHz, which is larger than before the cavity was inserted into the vacuum chamber. This may indicate that thermal material expansion during bake-out resulted in a slight change of the resonator

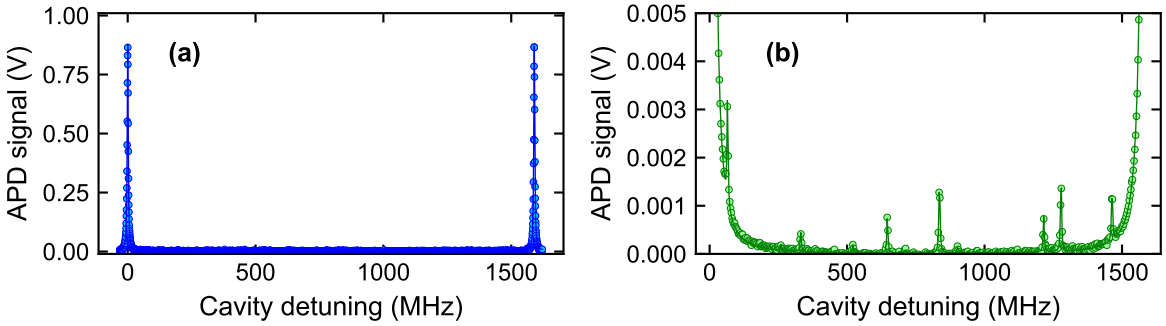


**Figure 3.8:** Cavity mode matching signal for the control beam path. The transmission through one of the HR cavity mirrors is recorded with an oscilloscope (Teledyne-LeCroy, HDO4104A-MS) using an avalanche photodetector (Thorlabs, APD130A) while scanning the signal laser frequency over one axial mode spacing. (a) the height of the peaks corresponding to the fundamental transverse cavity mode is determined at a high voltage range setting on the oscilloscope. The solid line is a fit using Eq. (3.6). (b) using a high resolution voltage range setting on the oscilloscope and averaging 46 traces, several peaks corresponding to higher order transverse modes can be identified. The solid line is a fit according to Eq. (3.7). Using Eq. (3.8) a mode matching efficiency of 98.9(2)% is obtained.

alignment. The on-resonance loss for reflected light is determined from Lorentzian fits to the reflection data, yielding 6.55(4)% (7.14(3)%) for the control (target) path. Assuming that each of the three HR mirrors contributes equally to the observed loss and that the I/O coupler is lossless, we obtain an HR mirror reflectivity of 99.990% (99.989%) from these numbers.

### 3.2.5 Mode Matching

High fidelity operation of the quantum gate requires that the transverse modes of the incoming control and target signal laser beams are matched to the transverse cavity eigenmode with high efficiency. For each beam, this is achieved by inserting two lenses into the beam path outside the vacuum chamber and by carefully optimizing their positions using micrometer screws. Similarly, the alignment of each incoming beam is optimized using two mirrors in kinematic mounts. The signals shown in Fig. 3.8 serve as a guide for this optimization.

To define the term mode matching efficiency, we write the electric field of a laser beam propagating along the positive $z$-axis as $\boldsymbol{E}(\boldsymbol{x},t) = \frac{1}{2}E(\boldsymbol{x})\boldsymbol{\epsilon}\exp(-i\omega t) + \text{c.c.}$ with $E(\boldsymbol{x}) \propto m(\boldsymbol{x})\exp(i\omega z/c)$, where $m(\boldsymbol{x})$ is the complex spatial mode function and $\boldsymbol{\epsilon}$ is the polarization vector, see Sec. 2.1. In the paraxial approximation, the eigenmodes of planar ring resonators are typically Hermite-Gauss modes [38, 141]. We express these eigenmodes as $m_{k,\ell}(\boldsymbol{x})$ with $k,\ell \in \mathbb{Z}_0^+$, where $(k,\ell)$ is the transverse mode order and $m_{0,0}$

is the fundamental cavity mode. Assuming the normalization

$$\int_{-\infty}^{\infty} dx \int_{-\infty}^{\infty} dy \, |m_{k,\ell}(x,y,z)|^2 = 1 \quad \forall z, \tag{3.2}$$

the $m_{k,\ell}(\boldsymbol{x})$ form an orthonormal basis for the space of transverse mode functions and we can expand the incoming laser beam mode

$$m_{\text{in}}(\boldsymbol{x}) = \sum_{k,\ell=0}^{\infty} a_{k,\ell} m_{k,\ell}(\boldsymbol{x}) \tag{3.3}$$

with

$$a_{k,\ell} = \int_{-\infty}^{\infty} dx \int_{-\infty}^{\infty} dy \; m^*_{k,\ell}(\boldsymbol{x}) m_{\text{in}}(\boldsymbol{x}). \tag{3.4}$$

We define the mode matching efficiency

$$\eta_{\text{mode}} = |a_{0,0}|^2 . \tag{3.5}$$

The mode matching setup was designed according to the following considerations. The incoming (outgoing) signal laser beams are coupled out of (into) polarization maintaining single-mode optical fibers using fiber couplers with a focal length of $f = 12\,\text{mm}$ (Schäfter+Kirchhoff, 60FC-4-M12-10). The free-space beam typically has a waist of 1.2 mm in front of the fiber couplers. To match the incoming beams to the cavity mode, it is important to note that the I/O coupling mirror acts onto the incoming beams like a plano-convex lens. To calculate the required beam parameters before the I/O coupler, we model the I/O coupler as a thick lens with refractive index $n_{fs} = 1.45$ of fused silica glass, using the ABCD matrices for curved interfaces from Chapter 15 in Ref. [141]. For the incoming control beam, we find a required beam waist in the tangential (sagittal) plane of $w_{\text{tang}} = 31.1\,\mu\text{m}$ ($w_{\text{sag}} = 31.4\,\mu\text{m}$) at a distance of $z_{\text{tang}} = 12.7\,\text{mm}$ ($z_{\text{sag}} = 14.3\,\text{mm}$) from the plane back side of the I/O coupler. For the target beam, the corresponding values are $w_{\text{tang}} = 126\,\mu\text{m}$, $w_{\text{sag}} = 136\,\mu\text{m}$, $z_{\text{tang}} = 13.3\,\text{mm}$, and $z_{\text{sag}} = -10.9\,\text{mm}$. The sign of $z_{\text{tang}}$ or $z_{\text{sag}}$ is negative if the corresponding waist, or a virtual image thereof, lies inside the mirror substrate or inside the cavity. Otherwise it is positive. These numbers show that perfect mode matching would require astigmatic beam shaping. However, we decided to use an axially symmetric incoming beam because the resulting mode matching error is only about 1%, as shown in App. E.

The focal lengths of the mode matching lenses are chosen such that they can be inserted into the beam path at suitable positions, see Fig. 3.13. We find that a combination of a plano-concave and a plano-convex spherical singlet lens with focal lengths of $-200\,\text{mm}$ and 150 mm (150 mm and $-100\,\text{mm}$) for the incoming control (target) beam is favorable. To minimize optical loss, these lenses have AR coatings at 780 nm (Laseroptik) with a specified reflectivity below 0.1% per surface.

To characterize the achieved mode matching efficiency, we compare the on-resonance cavity transmission signal of the fundamental mode to the signals from higher order modes,

which appear at different resonance frequencies as shown in Fig. 3.8 (b). We determine the height of the fundamental mode peak from Fig. 3.8 (a) by fitting the expression

$$U_0(\omega) = U_{\text{offs},0} + U_{0,0}\frac{1}{1 + (2\mathcal{F}\sin(2\pi((\omega - \omega_{0,0})/\Delta\omega_{\text{ax}})/\pi)^2}, \tag{3.6}$$

which is derived from Eqs. (2.1) and (2.3)–(2.6) assuming $t_a = 1$ and $\Delta_c = \omega - \omega_{0,0}$. When focusing the signal light transmitted through the cavity onto the photodetectors, we ensure that the spot size is much smaller than the size of the detector chip. Hence, we assume that each transverse component $m_{k,\ell}(\boldsymbol{x})$ of the incoming beam causes the same photodetector voltage per incoming power. We fix the obtained values for $U_{0,0}$, $\mathcal{F}$, and $\Delta\omega_{\text{ax}}$ from the previous fit and fit

$$U_{\text{ho}}(\omega) = U_{\text{offs,ho}} + \sum_{k,\ell} U_{k,l}\frac{1}{1 + (2\mathcal{F}\sin(2\pi(\omega - \omega_{k,l})/\Delta\omega_{\text{ax}})/\pi)^2}, \tag{3.7}$$

to the data in Fig. 3.8 (b) for all transverse orders ($k$,$\ell$) that are visible in the data. The mode matching efficiency is

$$\eta_{\text{mode}} = \frac{U_{0,0}}{\sum_{k,\ell} U_{k,\ell}}. \tag{3.8}$$

From a typical data set as shown in Fig. 3.8, we obtain $\eta_{\text{mode}} = 98.9(2)\%$. We regularly achieve very similar numbers with this method for both the control and the target beam path. Although the experimental setup is temperature stabilized, we observe that $\eta_{\text{mode}}$ typically drops by a few percent on a timescale of several days. Hence, we regularly re-optimize the alignment.

The statistical error on $\eta_{\text{mode}}$ estimated by the fit is presumably smaller than potential systematic errors. For instance, higher order transverse modes have a larger spatial extent and are therefore more likely to clip at the apertures in the cavity mount, see Fig. 3.6. This would cause a lower signal voltage on the photodetector per incoming power and would lead to an overestimation of the mode matching efficiency. Further improving $\eta_{\text{mode}}$ probably requires astigmatic input beam shaping, see App. E.

## 3.3 Vacuum Chamber

The experiments in this work require ultra-high vacuum (UHV) pressure levels to reduce the atom loss rate from the dipole trap due to collisions with background gas molecules. Fig. 3.9 shows the vacuum system. Prior to assembly, all suitable components were cleaned in an ultrasonic bath and heated to 200 °C in a separate bake-out chamber. After assembly, the system was connected to a turbo pump through the DN40CF angle-valve and baked out for two weeks at 120 °C. The 2D MOT cell dispensers, the ion pump, the non evaporable getter (NEG) module of the ion pump, and the vacuum gauge were degassed by applying a current during the bake-out, heating these components to a higher temperature than the rest of the system. The NEG module was activated during cool-down, with the rest of the vacuum system at 80 °C. After bake-out, the angle valve was closed and the turbo pump disconnected. The final pressure reading of the Bayard-Alpert gauge was

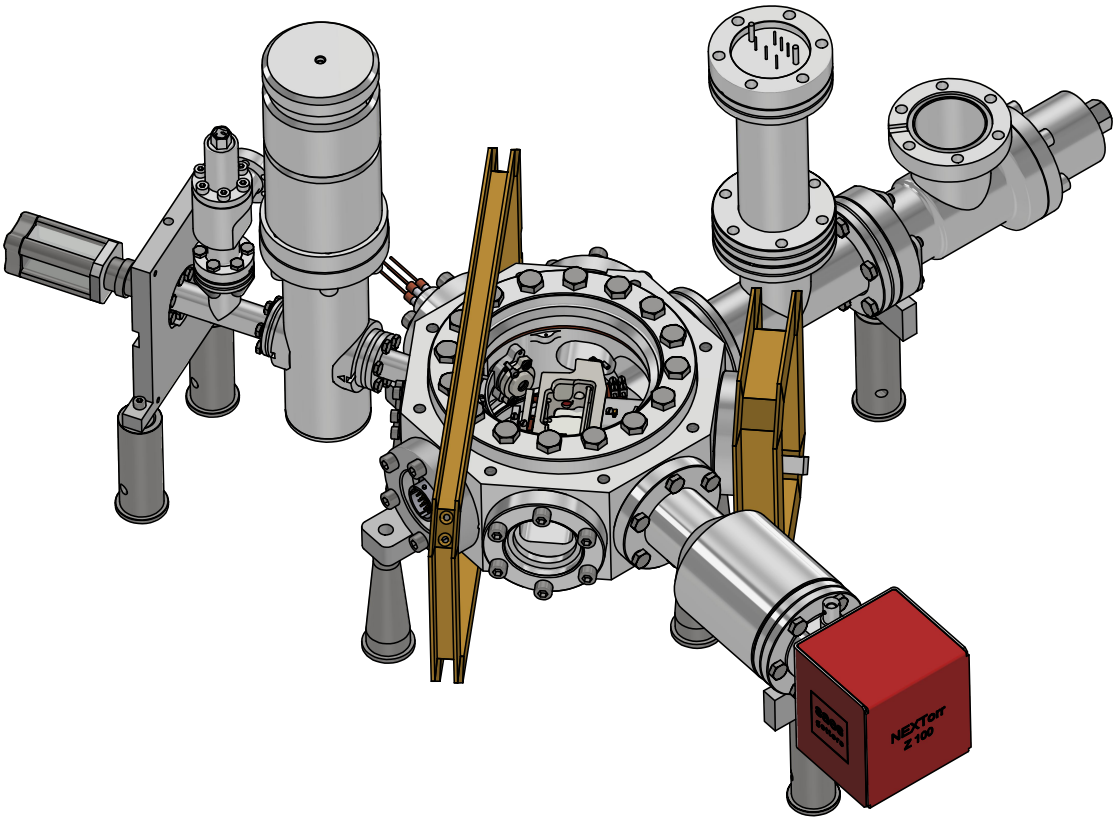


**Figure 3.9:** 3D model view of the vacuum system, adapted from Ref. [126]. The main chamber shown in the center is an octagon with two large DN100CF viewports at the top and bottom. It consists of stainless steel with low magnetic permeability (316 LN ESR). Inside, the resonator mount and the channeltron assembly are visible. Outside the chamber, the brass frames (beige) of the 3D MOT coils are located. A DN40CF T-piece, shown in the upper right corner, connects a Bayard-Alpert vacuum gauge and an angle valve for initial evacuation. On the opposite side of the main chamber, a 19 pin electric feedthrough (VACOM, CF40-MPC2-19-SE-CE-SSG) is visible. The ion getter pump (SAES Getters, NEXTorr Z 100) is drawn in red at the bottom right. In the far left of the image, the 2D MOT glass vacuum cell is located. It is connected to a DN16CF T-piece, attached to an angle valve (VAT, 54124-GE02-0001) and the all-metal gate valve, which leads to the main chamber. Copper wires (brown) of the HV feedthrough (VACOM, CF16-HV6-4-CE-CU13) for the channeltron are visible behind the gate valve. The whole vacuum system is supported by several posts, which are clamped onto the optical table. The height of these posts is chosen such that the atomic position and the cavity mode waist are located 5 inch = 127 mm above the optical table.

below $5 \times 10^{-10}$ mbar for a filament emission current of 1 mA.[3] The ion pump indicates a pressure below $1 \times 10^{-10}$ mbar. At these parameters, we measure trapping lifetimes in excess of 30 s.

Optical access to the cavity and to the atomic ensemble is provided by six viewports (MPF Products, custom made). All viewports consist of fused silica glass connected to a low magnetic permeability stainless steel (316 LN ESR) flange using a brazed solder seal, which is also nonmagnetic. We deliberately avoided the ferromagnetic solder material Kovar, which is known to develop leaks when exposed to rubidium. All viewports are AR coated on both sides. The two DN40CF viewports for cavity access, top and bottom in Fig. 3.2, have a specified reflectivity per surface of $< 0.1\%$ at 780 nm and 480 nm. The AR coating of the other viewports (2x DN100CF, 1x DN40CF, 1x DN16CF) is designed for a reflectivity per surface of $< 1\%$ in the range 480 nm to 532 nm and 770 nm to 1064 nm. All these numbers refer to 0° angle of incidence and are applicable for all beams except the Raman and MOT beams which pass through the DN100CF viewports under 45°, see Fig. 4.3. For these beams, a reflectivity per surface up to 2% is expected.

## 3.4 Electric Field Control

To utilize the Förster resonance described in Sec. 2.2.2, the electric field at the atomic position needs to be accurately controlled. To this end, four pin electrodes and two bar electrodes are integrated into the cavity mount. A voltage can be applied to each electrode individually. The resulting electric field is obtained from a numerical solution of Laplace's equation for the electrostatic potential $U$ in charge-free regions of space

$$\nabla^2 U(\boldsymbol{x}) = 0, \tag{3.9}$$

using a relaxation algorithm [83]. To this end, we use the implementation and utilities provided by the software SIMION.

For the simulation, relevant parts of the CAD model of the vacuum chamber are converted to a grid of points with a resolution of 0.1 mm. Each point of the grid is either vacuum or assigned to one of twelve electrodes. Fig. 3.10 shows an annotated 3D rendering of the electrode geometry.

Thanks to the properties of Laplace's equation, the electric field vector $\boldsymbol{E}(\boldsymbol{x}_0) = \nabla U(\boldsymbol{x}_0)$ at the atomic position $\boldsymbol{x}_0$ is a linear function of the 11-dimensional vector of electrode potentials $\boldsymbol{P}$. We express this linear dependence as

$$\boldsymbol{E}(\boldsymbol{x}_0) = M_{\text{conv}} \cdot \boldsymbol{P}, \tag{3.10}$$

where $M_{\text{conv}}$ is a $3 \times 11$ matrix. From the simulation, we find

$$M_{\text{conv}} = \begin{pmatrix} 0.00011 & -1.2 & -0.78 & -0.77 & -1.2 & 12 & 12 & 0.0031 & 0.011 & -0.017 & -0.38 \\ 0.0011 & -3.0 & -1.3 & 1.4 & 3.2 & -8.8 & 8.9 & -0.015 & 0.026 & 0.046 & 0.035 \\ -0.0029 & -1.1 & 1.0 & 1.0 & -1.1 & 0.14 & 0.18 & 0.0022 & 0.0074 & -0.12 & -0.064 \end{pmatrix} \mathrm{m}^{-1}. \tag{3.11}$$

[3] Setting a larger emission current of 10 mA yields higher pressure readings. Although a larger current should increase the sensitivity of the pressure measurement, we believe that the obtained values are not reliable because the power dissipated by the current also drastically heats up the tube, to which the gauge is attached. To avoid an increased pressure inside the main chamber due to the hot tube, we leave the gauge turned off completely for operating the system.

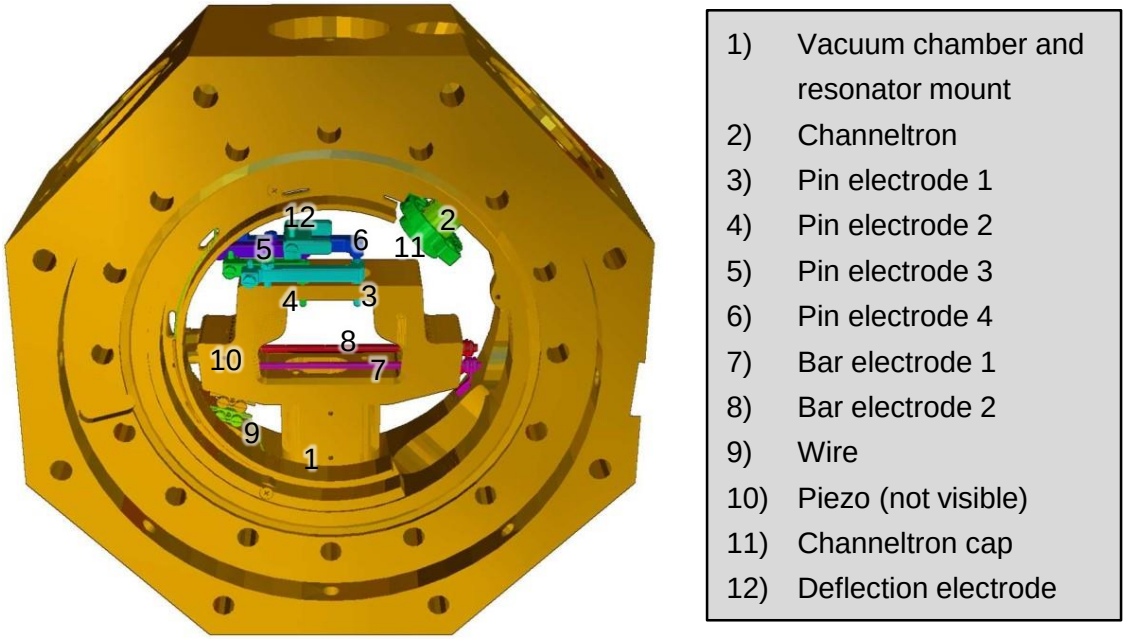


**Figure 3.10:** Electrode definition for the electric field simulation with SIMION. The image shows a 3D rendering of the simulation grid. Electrodes are shown in different colors.

The electrostatic potentials in $\boldsymbol{P}$ are defined relative to the potential of the vacuum chamber and the resonator mount. The order of the entries of $\boldsymbol{P}$ and of the columns of $M_{\text{conv}}$ is consistent with the enumeration of the electrodes 2–12 in Fig. 3.10 and the coordinate system is oriented as indicated in Fig. 3.2.

## 3.5 Field Ionization and Particle Detection

This sections covers tools for field ionization and particle detection that are integrated into the vacuum chamber. Although these tools were not used for the experiments in this thesis, they might become useful for future experiments. The purpose of this section is to provide documentation of the technical implementation and guidelines for operation. Related work and technical designs can be found in Refs. [5, 58, 77, 92].

Due to the weak binding of the Rydberg electron, Rydberg atoms can be ionized by applying moderate electric fields. For a given principal quantum number $n$, the required electric field $E_{\text{ion}}$ can be estimated classically as [5, 41]

$$E_{\text{ion}}(n) = \frac{1}{16}\frac{e}{4\pi\epsilon_0 a_0^2}\left(n - \delta_0\right)^{-4}. \tag{3.12}$$

Using the quantum defect $\delta_0 = 3.16$ [8], we find $E_{\text{ion}} = 80\,\frac{\text{V}}{\text{cm}}$ for $n = 48$. According to Eq. (3.11), an electric field of that magnitude is created when applying 330 V to the two bar electrodes shown in Fig. 3.10.

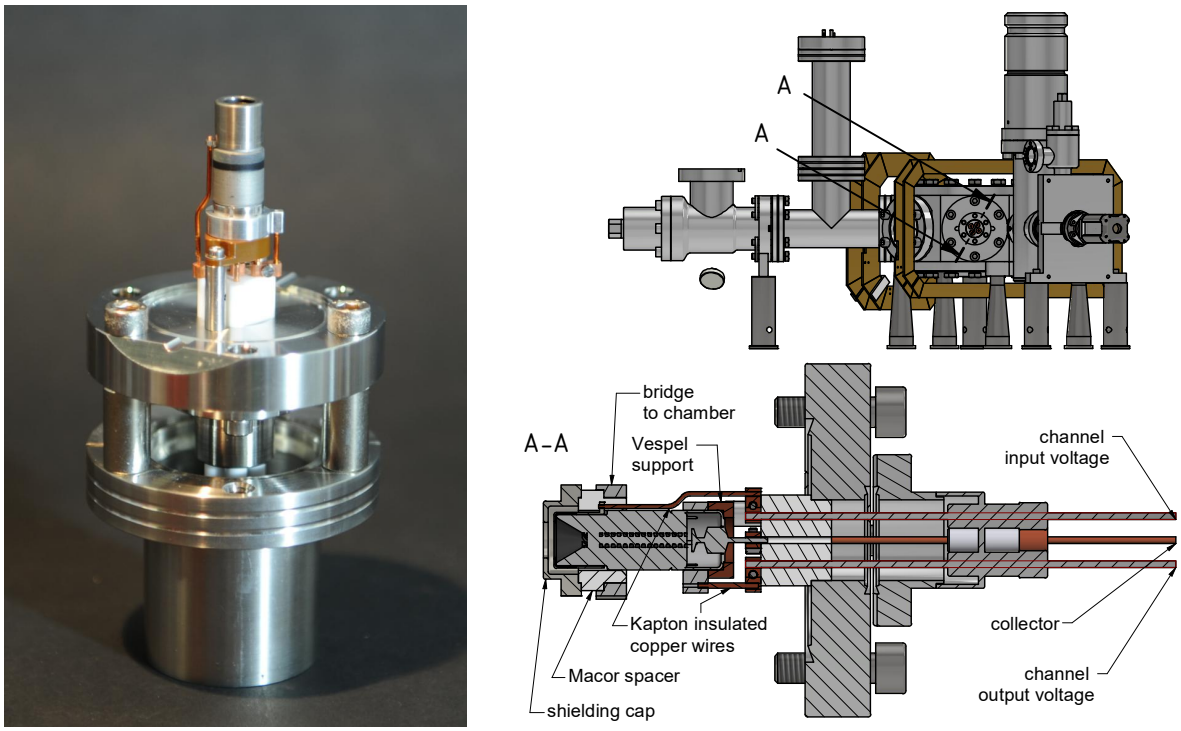


**Figure 3.11:** Photograph and technical drawing of the channeltron assembly. The channeltron is mounted onto the HV feedthrough flange and slides into a Macor spacer, which insulates the shielding cap (electrode 11 in Fig. 3.10) from the vacuum chamber. A cut along the indicated axis A-A illustrates the electrical connections.

The resulting ions or electrons can be detected using particle detectors such as channeltrons or multi-channel plates. Our setup contains a channeltron (PHOTONIS, MAGNUM 5901), which is shown in Fig. 3.11. It consists of a funnel-shaped input, six helical channels, and an electrically insulated collection anode. The channel output is operated at a positive voltage between 1.5 kV and 3 kV compared to the channel input. If a particle hits the input funnel, secondary electrons emerge from the surface and are accelerated down the channels. Successive collisions with the channel wall, which serves as a continuous dynode, result in a multiplication of the initial electrons. At the end of the channel, electrons are collected by the anode. Hence, the anode needs to be supplied with a slightly larger positive voltage than the channel output. In practice, this is often achieved by placing a bias resistor between the positive supply voltage, which is connected to the anode, and the channel output. Our channeltron has an internal bias resistor of 10% to 20% of the total channel resistance, which is specified between 18 MΩ and 50 MΩ. This leads to a bias current of roughly 100 µA through the channel. By measuring the anode current, particles hitting the input funnel can be detected. Detailed information about the operating theory of channeltrons can be found in Ref. [58].

As shown in Fig. 3.2, the channeltron does not have a direct line-of-sight to the atomic position. Hence, ions or electrons have to be steered towards the channeltron using a

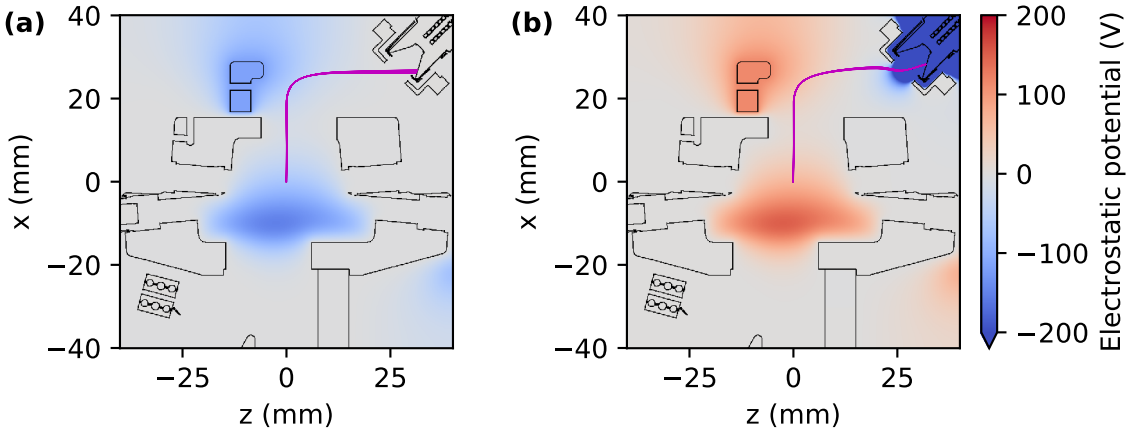


**Figure 3.12:** Simulation of (a) electron and (b) ion detection. The plot is a horizontal cut through the atomic plane ($y = 0$). Black lines mark the contours of electrodes and the color code indicates the electrostatic potential. A voltage of $-330\,\mathrm{V}$ ($330\,\mathrm{V}$) is applied to the bar electrodes, accelerating electrons (ions) in the positive $x$-direction. With the deflection electrode at $-115\,\mathrm{V}$ ($115\,\mathrm{V}$), the trajectories bend in $z$-direction such that the electrons (ions) hit the channeltron in the upper right corner. For detecting electrons (ions), the input of the channeltron is at $0\,\mathrm{V}$ ($-2\,\mathrm{kV}$). For each particle type, 100 trajectories were simulated, with a random starting position following a Gaussian distribution with $10\,\mu\mathrm{m}$ standard deviation centered at the coordinate origin.

deflection electrode, similar to Ref. [92]. To verify that this works, particle trajectory simulations were performed with SIMION. The results are shown in Fig. 3.12.

## 3.6 Laser Systems

The laser systems employed in this work have already been described in Refs. [8, 132, 149]. This section briefly explains minor modifications implemented in this thesis.

In previous experiments, the external cavity diode laser (ECDL) of the signal laser system at 780 nm (Toptica, DL pro) and the ECDL of the control coupling laser system[4] at 960 nm (Toptica, TA pro and SHG pro) were frequency stabilized using a reference cavity with a spacer made of ultra low expansion glass (Stable Laser Systems, ULE cavity), see Refs. [132, 149]. This cavity provides excellent frequency stability on short timescales, which enables locking the two ECDLs to a FWHM linewidth $< 2\,\mathrm{kHz}$ at an RMS integrated phase noise below 150 mrad measured out-of-loop between 50 kHz and 5 MHz [132].

The ULE cavity based locking approach has two disadvantages. First, a residual cavity drift of up to $\pm 600\,\frac{\mathrm{Hz}}{\mathrm{h}}$ requires occasional corrections to the locking setpoints and, second, it is difficult to lock both Rydberg coupling lasers onto the same ULE cavity.

[4] In Refs. [132, 149], this laser was actually used for the target photon. In this work, it is used for the control photon.

Hence, the second coupling laser (Toptica, TA-SHG pro) was previously locked onto the cavity-stabilized coupling laser using an offset phase lock. When addressing the atom-pair state $|67^2S_{1/2},69^2S_{1/2}\rangle$, the offset frequency was 24 GHz. For the atom-pair state $|48^2S_{1/2},50^2S_{1/2}\rangle$ used in this work, the required frequency offset is 68 GHz. This follows from Eq. (2.8), taking into account that the lasers emit light at 960 nm, which is frequency doubled to 480 nm. At such a high offset frequency, it becomes difficult to generate an error signal for the offset phase lock with good signal-to-noise ratio.

In front of this backdrop, we decided to phase lock the target coupling laser onto a new frequency comb (Menlo Systems, FC1500-250-ULN), which became available during this work and which has improved noise properties compared to our old comb. When the target coupling laser is phase locked to the frequency comb, it inherits part of the comb noise. The test report provided by Menlo indicates an in-loop RMS integrated phase noise of 80 mrad at 1 MHz bandwidth between the comb and its optical reference oscillator. Assuming that the reference oscillator has much lower noise than the comb, this number can be regarded as an estimate for the RMS integrated phase noise of the comb. To generate light at 960 nm, a part of the comb spectrum is amplified and then frequency doubled. It is expected that this will at least double the RMS integrated phase noise [131, 146]. Hence, comb noise is probably worse than the noise of our lasers locked onto the ULE cavity. This leaves room for future improvements concerning the phase noise of the target coupling laser.

To generate light for the Raman cooling scheme in Sec. 4.4, the previous ground state coupling laser (Toptica, DL pro) [132, 149] was tuned to a wavelength of 795 nm and stabilized onto the new frequency comb using an offset phase lock. Likewise, the stabilization light for the dual-rail setup, see next section, is derived from the previous stabilization laser for the Mach-Zehnder interferometers in Ref. [132] (Toptica, DL pro), which was tuned to a wavelength of 770 nm for this work.

## 3.7 Optical Setup for the Quantum-Logic Gate

### 3.7.1 Dual-Rail Setup and Cavity Lock

The control and the target qubits are implemented as weak coherent laser pulses containing less than one photon per pulse on average. These pulses are created using two independent double-pass AOM tracks. After the AOM track, each beam has a power of about 1 mW and is coupled into a polarization maintaining 50:50 fiber beam splitter. One of the outputs of each beam splitter is connected to a photodetector (Thorlabs, PDA10A) for monitoring the pulse shape. The other output is connected to two fiber-based attenuators which reduce the pulse energy to the single-photon level. Polarization maintaining single-mode fibers transport the single-photon pulses to the optical setup shown in Fig. 3.13, which implements the dual-rail scheme introduced in Sec. 2.6.

The input polarization states of the two qubits are prepared using a combination of a half- and a quarter-wave plate after a polarizing beam splitter cube (PBS) for polarization cleaning. The four PBSs from Fig. 2.3 marking the inputs and outputs of the quantum gate are implemented as polarizing plate beam splitters at Brewster's angle (Brewster PBS,

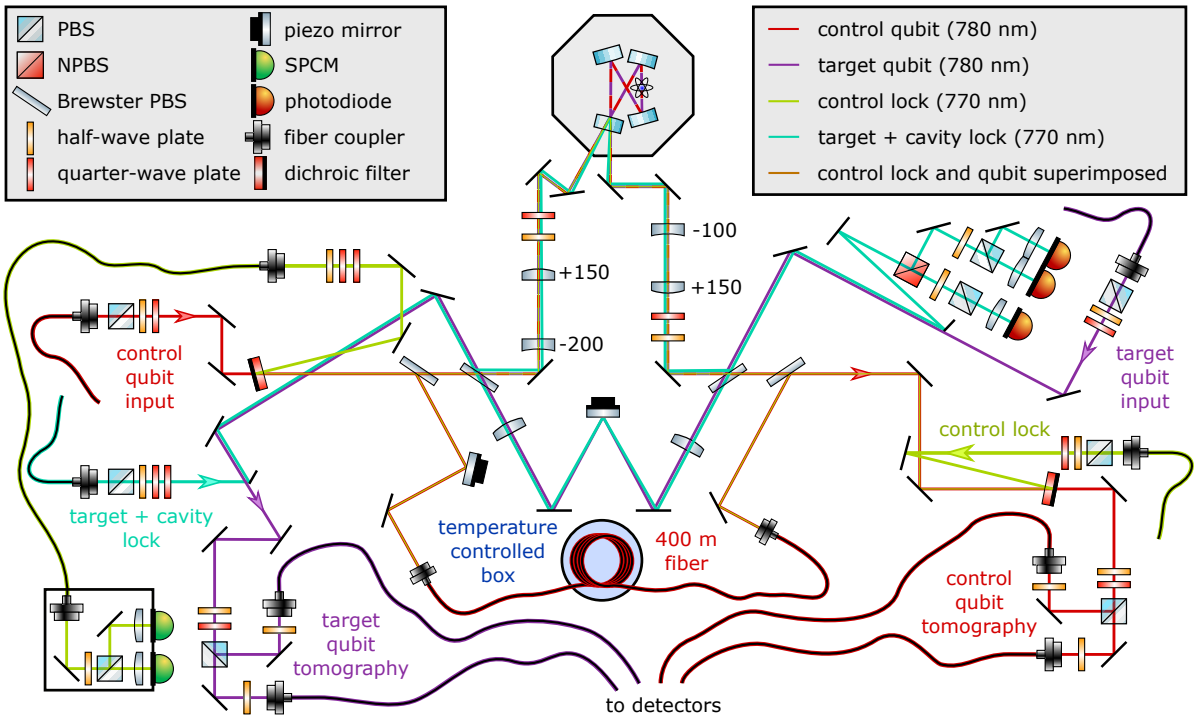


**Figure 3.13:** Dual-rail setup. Explanations are provided in the text.

purchased from Perkins Precision Developments). In addition to the cavity mode matching lenses introduced in Sec. 3.2.5, two lenses with focal lengths of 200 mm are placed in the target bypass path to optimize the mode matching with the beam exiting from the cavity path. A half- and a quarter-wave plate before and behind the cavity convert between the linear input and output polarization states and the circular polarization states required to address the atomic transition.

To keep the optical path length differences between the cavity path, the control bypass, and the target bypass constant, two mirrors glued onto piezo stacks (PI Ceramic, PICMA P-888.91) are used as actuators for two feedback loops. The error signals for these feedback loops are generated with stabilization light at 770 nm. Each of the two stabilization beams is sent onto its respective input Brewster PBS in a superposition polarization state $|\psi_{\text{in}}\rangle = (|H\rangle + \exp(i\phi_{\text{in}})|V\rangle)/\sqrt{2}$. Assuming equal transmission through the $|H\rangle$ and $|V\rangle$ path,[5] the resulting output polarization state is $|\psi_{\text{out}}\rangle = (|H\rangle + \exp(i(\phi_{\text{in}} + \Delta\phi))|V\rangle)/\sqrt{2}$, where $\Delta\phi = 2\pi\Delta L/\lambda$ is the phase shift due to the path length difference $\Delta L$. Using a combination of a half-wave plate and a PBS, the output power in states $|D\rangle$ and $|A\rangle$ is measured with two detectors. Subtracting the two measured powers yields a signal proportional to

$$|\langle D|\,\psi_{\text{out}}\rangle|^2 - |\langle A|\,\psi_{\text{out}}\rangle|^2 = \cos(\phi_{\text{in}} + \Delta\phi), \tag{3.13}$$

which has zero crossings at $\phi_{\text{in}} + \Delta\phi = \pi(2n+1)/2$ with $n \in \mathbb{Z}$. One of these zero crossings is used for keeping $\Delta L$ constant using a proportional-integral (PI) controller. The setpoint

[5] For the control path, this is a poor assumption. However, it is easy to modify the input state such that the desired output state is obtained.

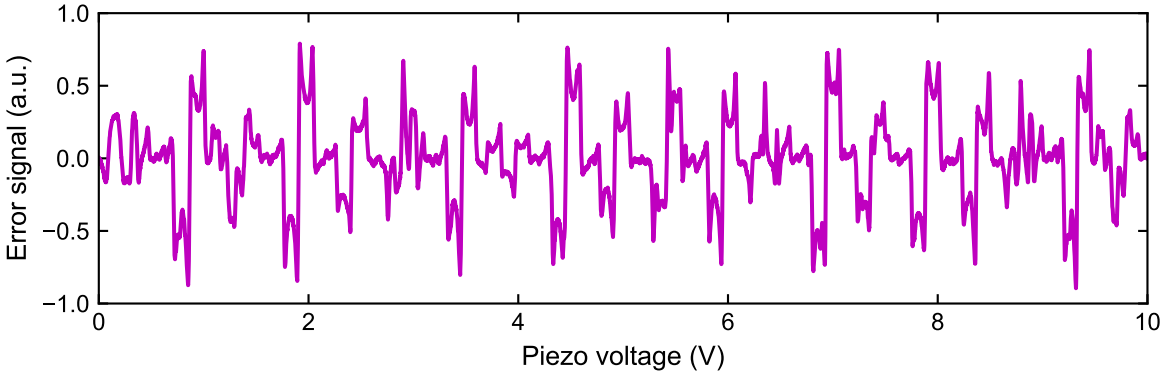


**Figure 3.14:** Cavity lock error signal when scanning the cavity length by varying the piezo voltage. As the stabilization beam couples to many higher-order transverse cavity modes, several PDH features can be identified in the signal. Any of the zero crossings can be used for locking. One axial mode spacing corresponds to 8.5 V.

of this feedback loop can be adjusted by rotating one of the input waveplates to change $\phi_{\text{in}}$ or, alternatively, by changing the detection basis from $D/A$ to other 50:50 superpositions of $|H\rangle$ and $|V\rangle$.

The target stabilization beam additionally generates the error signal for the cavity lock using a Pound-Drever-Hall (PDH) [25] locking technique. This technique requires phase modulation of the input light, which we achieve using a free-space electro-optic modulator (EOM) driven at 25 MHz and located before the input fiber. This modulation does not affect the target path length stabilization because the modulation frequency is larger than the bandwidth of the selected photodetector (Thorlabs, PDB210A). Likewise, interference between the cavity and the bypass polarization components does not affect the cavity lock error signal, because the bypass polarization is filtered out before the cavity lock photodetector (Thorlabs, APD130A) using a PBS.

For the target stabilization beam, combining and separating the 780 nm and 770 nm light is achieved using D-shaped mirrors. As a result, the stabilization beam travels through the dual-rail setup with a vertical offset of about 2 mm compared to the qubit beam. Hence, the stabilization beam is not well mode matched to the fundamental transverse cavity mode. This is advantageous to avoid light shifts and photon scattering at the atomic position caused by the 770 nm light, which has an input power of about 10 µW. Instead, the stabilization beam couples to several higher order transverse cavity modes. Each of these modes generates a PDH signal at a different resonance frequency, as shown in Fig. 3.14. Any of the zero crossings in this signal can be used for stabilizing the frequency difference between the cavity resonance and the stabilization laser. The absolute cavity resonance frequency is set by adjusting the stabilization laser frequency, which is referenced to the frequency comb using an offset phase lock.

In contrast to the target stabilization beam, the control stabilization beam needs to be well mode matched to the control qubit beam because both beams are coupled into the control bypass fiber. Hence, we use dichroic filters (Semrock, MaxDiode LD01-785/10,

measured transmission 99.7% at 780 nm) for combining and separating these beams. To avoid light shifts and photon scattering at the atomic position, it is advantageous to use a very low input power of about 1 pW at 770 nm. We detect this stabilization light using two single-photon counting modules (Excelitas, SPCM CD-3515H) after a non-polarization-maintaining single-mode fiber. A field-programmable gate array (FPGA) generates an error signal proportional to the difference between the SPCM count rates, using an infinite impulse response filter (exponentially weighted moving average) with a time constant of 8 ms.

The PI controllers for the control and target path stabilization as well as for the cavity lock are implemented digitally using two FPGA-based test and measurement boards (Red Pitaya STEMLab 125-14) running the open-source software package PyRPL. The PDH error signal for the cavity lock is digitally demodulated on the FPGA. The Red Pitaya boards have two 14 bit digital-to-analog converter outputs with a 2 V output voltage range. The output voltage is amplified to a range of 0 V to 10 V using an analog circuit. For the cavity lock, this voltage range covers slightly more than one axial mode spacing. For the control and target path stabilization, it corresponds to a little more than two wavelengths. If the feedback loop reaches one of the boundaries of the output voltage range, the control software automatically relocks the system near the center of the range. Such a relock event leads to a change of the stabilized path length by one wavelength at 770 nm. However, at 780 nm this corresponds to a phase shift of $2\pi(1 - 770/780) = 81$ mrad. If too many relock events occur, these phase shifts accumulate to an intolerably high value. To reduce relocking, the optical table, the optical resonator, and the control bypass delay fiber are temperature stabilized. For the cavity lock, relocking is never required under these conditions. However, the control path lock still suffers from relatively strong drifts due to the long optical fiber, requiring several relock events per minute. When operating the experiment, we therefore measure the control qubit output polarization at 780 nm several times per minute and readjust the setpoint of the feedback loop by rotating the half-wave plate before the control stabilization detectors. This procedure is automated using a computer-controlled rotation stage.

### 3.7.2 Efficiency of Optical Components and Detectors

Keeping optical loss under control is important when aiming at a high efficiency optical quantum gate. For each qubit, the gate setup starts at the respective input Brewster PBS and ends at the output Brewster PBS. For a resonant and empty cavity, the control qubit transmission through the gate setup is 90% for $H$ polarization and 63% for $V$ polarization. The corresponding values for the target qubit are 97% for $H$ polarization and 91% for $V$ polarization. Optical loss is caused by the transmission of 65% through the delay fiber, the resonant empty-cavity reflection loss of about 7%, the transmission through the lenses in the target bypass path of 99%, the Brewster PBS transmission of 99.7%, and the reflectivity of the mirrors outside the vacuum chamber of about 99.9%. The residual loss in the cavity path can be explained by a loss of about 0.1% per surface for each of the 22 AR coated surfaces, including four mode matching lenses, four waveplates, two passes through the vacuum viewport, and two passes through the plane side of the I/O coupling cavity mirror.

To measure the output state produced by the quantum gate, we use photonic state tomography [3] for each qubit. To this end, two duplicate tomography setups consisting of a computer-controlled half- and quarter-wave plate and a PBS are located after the output of the gate. For detection, the beams are coupled into polarization maintaining single-mode optical fibers which are spliced to the input fibers of a superconducting nanowire single-photon detection (SNSPD) system. This system was purchased from Quantum Opus and consists of a cryostat (QO-CRYO-HC4E2) and eight detection channels (QO-NPD-780-HDE), four of which are used for this experiment. The specified detection efficiency is 90% for 780 nm at a timing resolution of 70 ps and a maximum dead time of 25 ns. Including fiber coupling and splicing losses of 15%, we estimate a total detection efficiency of 77% for each of the four channels.

# Chapter 4

# Preparation of Ultracold Atoms inside the Optical Resonator

A crucial prerequisite for the quantum gate is the ability to prepare an ultracold atomic ensemble inside the resonator. To this end, a number of techniques for laser cooling and trapping are employed, which are well established and described extensively in the literature [50, 81, 96, 159]. This chapter explains how these techniques are implemented in our experimental setup.

The first two sections 4.1 and 4.2 describe the 2D and 3D MOT. These techniques produce a relatively large atomic ensemble inside the optical resonator and transfer a part of it into an optical dipole trap, as explained in Sec. 4.3. Inside the dipole trap, the Raman cooling scheme introduced in Sec. 4.4 further reduces the atomic temperature and prepares the ensemble in the desired spin state. As a last preparation step, Sec. 4.5 explains how lowering the power of the dipole trap leads to an expansion of the atomic ensemble, after which the target temperature is reached. Sec. 4.6 describes how the atoms are positioned at the cavity mode waist. To verify that all preparation steps were successful, a normal mode spectrum is finally observed and analyzed in Sec. 4.7.

## 4.1 2D MOT

2D MOTs are widely used to produce cold atomic beams for loading a 3D MOT. This technique allows for fast loading rates while maintaining UHV pressure at the 3D MOT position. For an extensive description of 2D MOTs, see Refs. [23, 61, 134, 166].

As mentioned in Sec. 3.1, our implementation uses a commercial 2D MOT package bought from Cold Quanta. It consists of a permanent magnet assembly, creating a specified magnetic field gradient of 37 $\frac{\mathrm{G}}{\mathrm{cm}}$, and a glass cell, into which two rubidium dispensers are integrated. The atomic beam leaves the glass cell through an exit hole with a diameter of 0.75 mm.

The optical setup for the 2D MOT is shown if Fig. 4.1. Each of the four cooling beams has a power of 50 mW at a red detuning of 11 MHz from the cycling transition of the $D_2$ line. To obtain a high flux of cold atoms, a large cooling volume is helpful. We achieve this by using elliptically shaped beams with spot sizes ($1/e^2$ radius of the intensity) of about 18 mm along and 6 mm perpendicular to the cell axis. The repumping beam is overlapped with the cooling light. It has the same beam size and a total power of 4 mW. To enhance

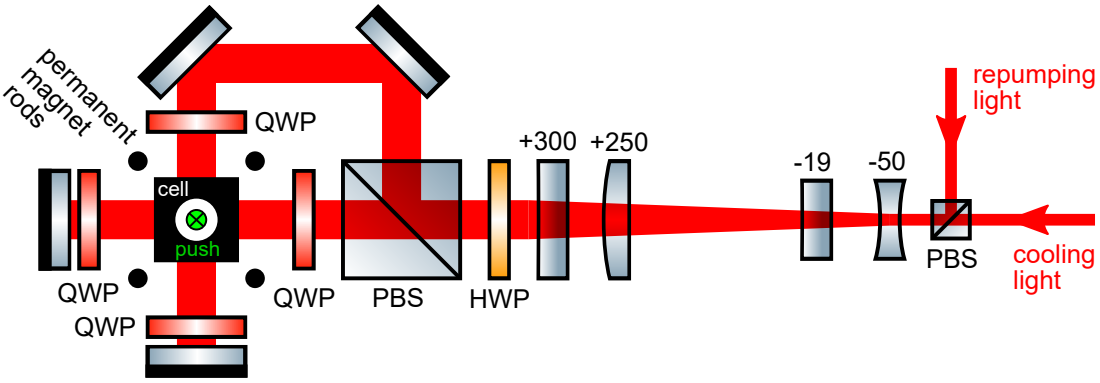


**Figure 4.1:** Optical setup for the 2D MOT. The drawing shows a side view of the 2D MOT cell (black rectangle). Four permanent magnet rods (black circles) generate the required magnetic field gradient. Cooling and repumping light (red) is superimposed on a polarizing beam splitter (PBS). Four appropriately oriented cylindrical lenses create a large beam that is elongated along the cell axis. A combination of a half-wave plate (HWP) and a PBS splits the incoming light into a horizontal and a vertical cooling beam. Quarter-wave plates (QWPs) generate the required circular polarization. Both cooling beams are retroreflected by a combination of a QWP and a mirror. The cold atom flux from the cell is enhanced by sending a push beam (green) along the cell axis, which points into the drawing plane.

the cold atom flux, a resonant push beam with a power of 7 mW and a spot size of 1 mm travels along the cell axis.

According to Cold Quanta, an atom flux up to $4 \times 10^9 \, \frac{\text{atoms}}{\text{s}}$ can be achieved with this 2D MOT cell design. In our setup, we measure a 3D MOT loading rate of $4 \times 10^7 \, \frac{\text{atoms}}{\text{s}}$ as shown in Fig. 4.2. As this is sufficient for the experiment, we put no effort into increasing the loading rate further. For instance, we operate only one of the dispensers at a relatively low current of 2.3 A.

It bears noting that we expect to transfer only a part of the atomic beam to the 3D MOT, because there is an aperture with 6 mm radius in the resonator mount and because not every atom that makes it through this aperture is captured. On its way toward the 3D MOT, the cold atomic beam typically expands at a divergence angle of 35 mrad according to Cold Quanta. This yields a beam diameter of about 10 mm after a traveled distance of 30 cm, see Fig. 3.2. Moreover, during the travel time of 35 ms obtained from Fig. 4.2 the atomic beam bends downwards by about 6 mm due to the gravitational force. To avoid further deflection of the beam due to magnetic field gradients, we chose nonmagnetic materials for the vacuum tubes and the gate valve, through which the beam has to travel.

## 4.2 3D MOT

A 3D MOT simultaneously cools and traps atoms. We employ this technique to collect atoms from the cold atomic beam in order to transfer them into an optical dipole trap

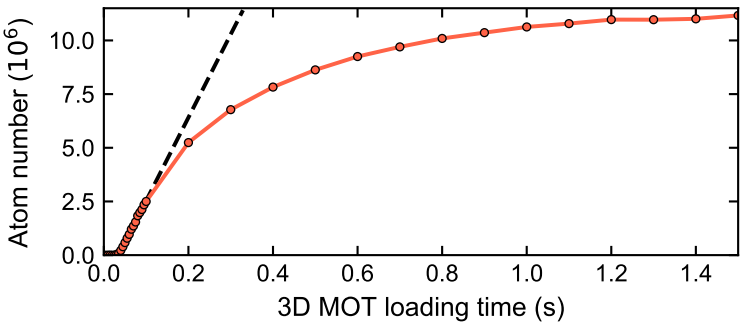


**Figure 4.2:** Loading curve (red) of the 3D MOT. The dashed line is a linear fit to the data points between 40 ms and 100 ms, yielding a delay of 35 ms and a loading rate of $4 \times 10^7 \, \frac{\text{atoms}}{\text{s}}$. At longer times, the measured atom number in the 3D MOT saturates and the cloud becomes larger than the region observed by the camera.

for the following cooling steps. Our setup offers the advantage that the 3D MOT can be operated directly at the mode waist of the optical resonator, because the resonator mount offers enough optical access for the cooling laser beams. As we require only a comparatively low atom number and density for the experiment, the 3D MOT performance is relatively uncritical. The scope of this section is therefore limited to a basic description and characterization. For an in-depth explanation of MOTs, see e.g. Ref. [96].

Fig. 4.3 illustrates the beam paths for cooling and trapping inside the main chamber. The 3D MOT trapping light has a total power of 15 mW and a red detuning of 15 MHz during the loading phase. Each beam has a spot size of about 7 mm, truncated by an aperture inside the cavity mount with 14 mm diameter. The repumping beam has a spot size of about 5 mm and a power of 1.5 mW. At a current of 8 A, the MOT coils generate a magnetic field gradient of $\partial_x B_x = -9 \, \frac{\text{G}}{\text{cm}}$, $\partial_y B_y = 6 \, \frac{\text{G}}{\text{cm}}$, and $\partial_z B_z = 3 \, \frac{\text{G}}{\text{cm}}$ along the $x$-, $y$-, and $z$-axis.[1] This implies that the current direction is clockwise when looking at the coils from the atomic position. The cooling beams along the coil axes are $L$ polarized and the beams perpendicular to the coil axes are $R$ polarized.

To characterize the cooling performance, we record absorption images of the atomic ensemble and determine the RMS cloud radius $\sigma$ and the atom number from a 2D Gaussian fit. Assuming that the atoms are released at time $t_0$ from a harmonic trap, the increase of the cloud radius as a function of time $t > t_0$ is given by

$$\sigma(t) = \sqrt{\sigma_0^2 + \frac{k_B T}{m}(t - t_0)^2}, \tag{4.1}$$

where $\sigma_0$ is the initial RMS radius, $k_B$ is the Boltzmann constant, $T$ is the temperature and $m$ is the atomic mass. By varying the time of flight $t$, the atomic temperature is

[1] The long MOT coil has inner diameters of 300 mm and 120 mm, a winding number of 70, and a resistance of about 1 Ω. The short coil has inner diameters of 80 mm and 120 mm, a winding number of 261, and a resistance of about 2 Ω. To reduce heat transfer onto the optical table at a typical operating power of 190 W, both coil frames are water cooled.

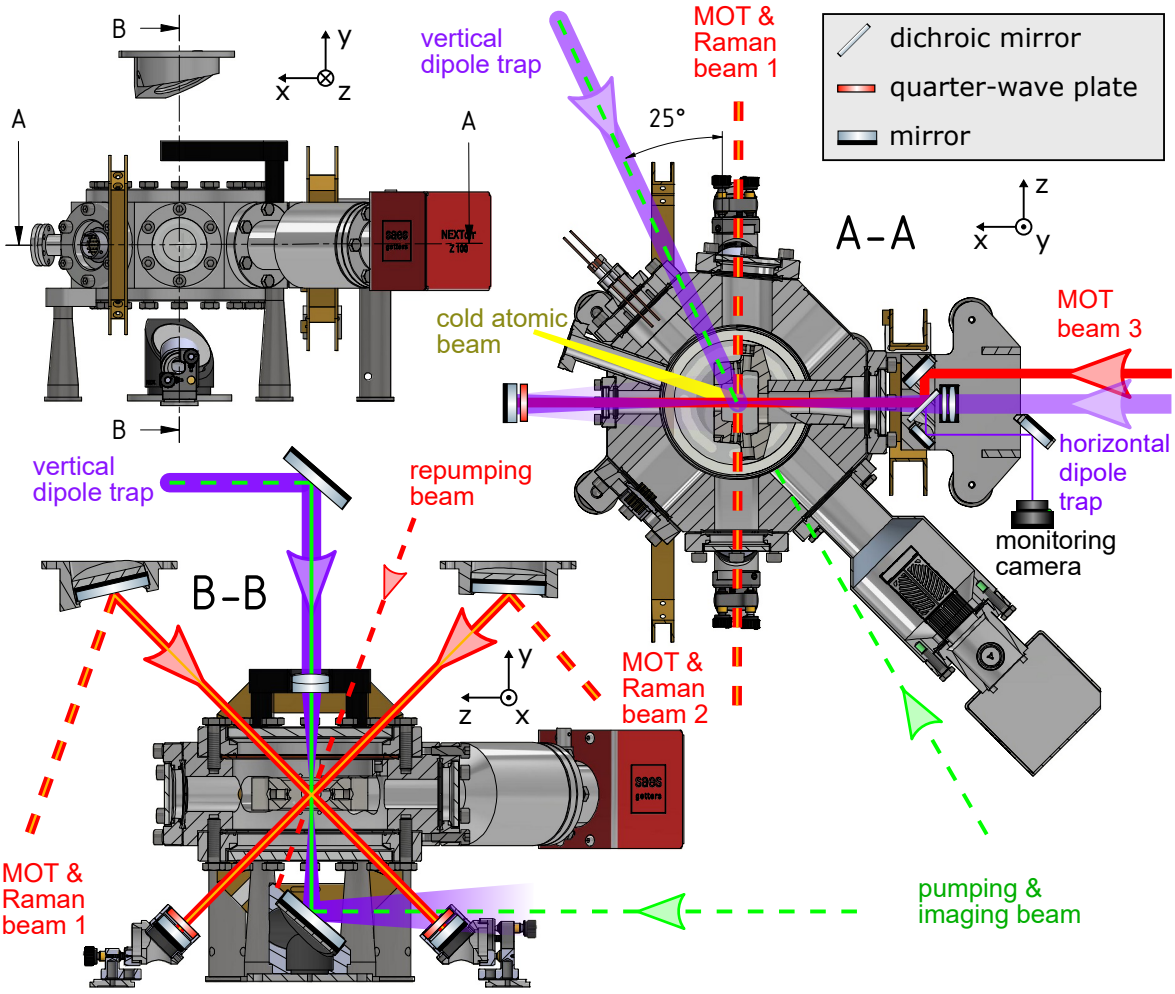


**Figure 4.3:** Beam paths for cooling and trapping inside the main chamber. Two cuts through the CAD drawing of the vacuum chamber along the indicated axes A-A and B-B are shown. Some components of the vacuum system are omitted for clarity, such as the 2D MOT appendix, the channeltron, the electrodes, and the vacuum gauge. Solid (dashed) colored lines denote laser beams in (outside) the drawing plane. The 3D MOT beams (red) are retroreflected after passing through the chamber, such that only three input beams are required. Two of these beams enter the system through the top viewport under an angle of 45°. These beams are superimposed with Raman cooling light (orange). The repumping light for the 3D MOT enters the chamber at a slightly steeper angle through the same viewport. The horizontal dipole trap beam (purple) is focused by an air-spaced lens doublet (Thorlabs, ACA254-150-1064) with a focal length of 150 mm. A small part of the dipole trap light power is reflected from a dichroic mirror and sent onto a camera for monitoring. The remaining light is transmitted and superimposed with the third 3D MOT beam, just before both beams enter the chamber through a DN40CF viewport. The cold atomic beam (yellow) from the 2D MOT reaches the center of the chamber at an angle of 19° to the horizontal 3D MOT beam. The vertical dipole trap (purple) is prepared on a breadboard above the chamber (not drawn), where also the imaging system is located, and is focused through the top viewport by an achromatic lens doublet (Thorlabs, AC254-075-AB) with a focal length of 75 mm. The optical pumping beam and the imaging beam enter the chamber through the bottom viewport.

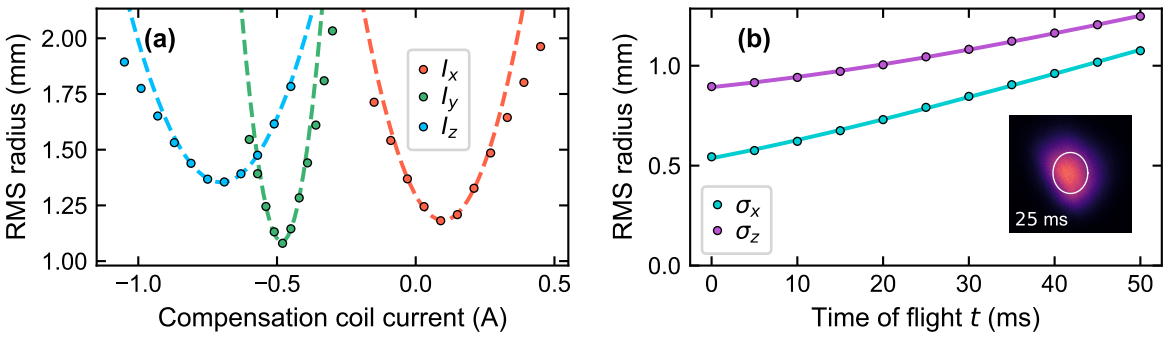


**Figure 4.4:** Optimization of polarization gradient cooling. The RMS radius of the ensemble after release from the trap is determined from absorption images by fitting a circular (a) and elliptical (b) 2D Gaussian function. The data in (a) is taken 40 ms after the cooling light is turned off. Hence, smaller cloud radius corresponds to lower temperature. By varying the current $I_x$, $I_y$, and $I_z$ through the compensation coils along the $x$-, $y$-, and $z$-axis, the points with best cooling performance are identified from a quadratic fit (dashed lines). At this optimum, a time-of-flight measurement (b) is performed with $5 \times 10^7$ atoms. The solid line is a fit using Eq. (4.1), yielding a temperature of 1.8(1) µK and 1.6(1) µK along the $x$- and $z$-direction. The inset shows a color coded absorption image of the ensemble after 25 ms, in which the white ellipse marks the RMS radius of the 2D Gaussian fit.

determined from a fit of Eq. 4.1. After MOT loading, we typically obtain $4 \times 10^7$ atoms at a temperature of 180 µK.

Absorption images were initially recorded with a preliminary setup, which had a magnification of 1/3.6 and used a single plano-convex lens with a focal length of 100 mm. This imaging system was used to record the data in Fig. 4.4, at a MOT coil current of 10 A. It was later replaced by the imaging system described in Ref. [126], which has a magnification of 4.7 and a resolution in the atomic plane (FWHM of the point spread function) of 4.7 µm limited by the 16 µm pixel size of the camera (Andor iXon DV887 EMCCD) and by the numerical aperture of the imaging system of 0.167. As shown in Fig. 4.3, the imaging beam travels along the positive $y$-axis and has a power of about 100 µW at a spot size of 3.7 mm.

After loading the 3D MOT, polarization gradient cooling (PGC) [20, 96] is performed. To this end, the MOT coil current is turned off in 0.2 ms, the red detuning of the cooling light is increased to 70 MHz, and the power is ramped from 50 mW to 5 mW in 10 ms, similar to Ref. [135]. To optimize the cooling performance, the background magnetic field is compensated at the 3D MOT position using three pairs of compensation coils.[2]

[2]Two rectangular coil pairs, with inner diameters of 789 mm and 219 mm, a coil separation of 845 mm, a winding number of 180, and a resistance of 6.6 Ω per coil generate a magnetic field along the $x$- and $z$-axis. A pair of square coils with an inner diameter of 804 mm, a coil separation of 240 mm, a winding number of 39, and a resistance of 2.3 Ω produces a field along the $y$-axis. The atomic position is located in the center of each coil pair. Using microwave spectroscopy with an atomic ensemble at the cavity mode waist, we find that the compensation coils produce a magnetic field per current of

Fig. 4.4 (a) shows this optimization. Quadratic fits (dashed lines) to the data points near the minimum yield optimal compensation coil currents of 0.10 A, −0.48 A, and −0.70 A. At the optimum, the achieved temperature is characterized with a time-of-flight measurement shown in Fig. 4.4 (b). Due to the non-uniform magnetic field gradient produced by the MOT coils, the atomic ensemble in the trap is elongated in the $z$-direction. This becomes important for the analysis in (b), because some data points are recorded at short expansion time. Elliptical 2D Gaussian fits are employed to extract the RMS cloud radii $\sigma_x$ and $\sigma_z$ along the $x$- and $z$-direction. The solid lines are fits using Eq. (4.1). Along the $x$-direction, we find an initial RMS cloud radius of $\sigma_{0,x} = 0.42(3)\,\mathrm{mm}$, $t_0 = -26(3)\,\mathrm{ms}$, and $T = 1.8(1)\,\mu\mathrm{K}$. Similarly, we obtain an initial RMS cloud radius of $\sigma_{0,z} = 0.83(3)\,\mathrm{mm}$), $t_0 = -26(3)\,\mathrm{ms}$), and $T = 1.6(1)\,\mu\mathrm{K}$ along the $z$-direction.

From Eqs. (11.6) and (11.7) in Ref. [96] one expects that the ratio of the equilibrium ensemble size in a MOT is related to the magnetic field gradients according to

$$\frac{\sigma_{0,x}^2}{\sigma_{0,z}^2} = \left|\frac{\partial_x B_x}{\partial_z B_z}\right|. \tag{4.2}$$

The agreement between the value 0.26(4) obtained for the left-hand side and 1/3 for the right-hand side is fair.

The nonzero values obtained for $t_0$ are plausible, because the atomic ensemble already expands during PGC, as turning off the magnetic field gradient eliminates the spatial confinement of the 3D MOT. Due to the initially higher temperature, it appears to the fit as if this expansion time was longer than the actual PGC time of 10 ms.

## 4.3 Optical Dipole Trap

### 4.3.1 Beam Path

To obtain an atomic ensemble that is smaller than the Rydberg blockade radius, a crossed-beam optical dipole trap (ODT) at a wavelength of $\lambda_{\mathrm{ODT}} = 1064\,\mathrm{nm}$ is used. It consists of a vertical and a horizontal beam, both of which are tightly focused at the atomic position, as shown in Fig. 4.3. The beams are derived from two different lasers, which run at sufficiently different frequencies such that interference between the two beams has a negligible effect onto the atomic density distribution.

The horizontal trapping beam is derived from a single frequency Nd:YAG laser (Innolight, Mephisto 2000) at a wavelength of 1064 nm. The beam is coupled out of a polarization-maintaining single-mode fiber near the vacuum chamber, using a fiber collimator (Thorlabs, F810APC-1064) with a focal length of 36.6 mm. The outcoupled beam has a spot size of about 6 mm. After polarization filtering with a PBS, the beam profile is narrowed along gravity using two cylindrical lenses with focals lengths of 100 mm and −50 mm. Next, two spherical lenses with focals lengths of −50 mm and 100 mm expand the beam

0.740(5) $\frac{\mathrm{G}}{\mathrm{A}}$, 1.386(3) $\frac{\mathrm{G}}{\mathrm{A}}$, and 0.676(3) $\frac{\mathrm{G}}{\mathrm{A}}$ in $x$-, $y$-, and $z$-direction, defined by the coordinate system in Fig. 3.2. A magnetic field of approximately zero is obtained for currents of 0.09 A, −0.41 A, and −0.67 A. This corresponds to a background magnetic field vector of $\boldsymbol{B} = (-0.07, 0.57, 0.45)$ G when the coils are turned off.

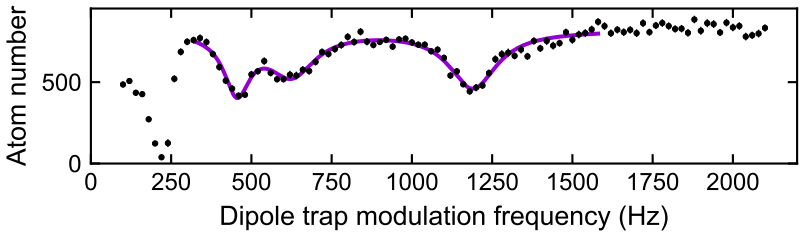


**Figure 4.5:** Trapping frequencies in the crossed-beam ODT. The plot shows a measurement of the atom number after modulating the intensity of both trapping beams for 400 ms at various frequencies. Parametric heating [129] removes atoms from the trap, when the modulation frequency equals twice the trapping frequency. Due to the gravitational sag, heating also occurs when the modulation frequency equals the trapping frequency along the $y$-axis. The observed dips correspond to $\omega_y$, $2\omega_y$, $2\omega_x$, and $2\omega_z$ in order of ascending frequency. The resonance frequencies $(\omega_x, \omega_y, \omega_z)/2\pi = (0.313(4), 0.228(2), 0.595(2))$ kHz are obtained by fitting a sum of three Lorentzians (solid line) to the data between 300 Hz and 1600 Hz.

to spotsizes of 6 mm and 12 mm. This beam is then sent onto the final focusing lens (Thorlabs, ACA254-150-1064 air spaced doublet) shown in Fig. 4.3. After the lens, a dichroic mirror overlaps the 1064 nm light with the horizontal 3D MOT beam. Due to imperfect AR coatings, a small part of the 1064 nm power is reflected from the first surface of the dichroic mirror. This reflex is used to obtain an estimate for the beam size at the atomic position. We measure beam waists of $w_{y,0} = 15\,\mu\text{m}$ and $w_{z,0} = 11\,\mu\text{m}$ along the $y$- and $z$-axis.

For the vertical trapping beam, an Ytterbium-doped fiber laser (Azurlight Systems, ALS-IR-20-SF) at 1064 nm is employed. The beam is coupled out of a polarization-maintaining single-mode fiber on the breadboard above the vacuum chamber, using a fiber collimator (Schäfter+Kirchhoff, 60FC-0-M20-08) with a focal length of 20 mm. The outcoupled beam has a spot size of about 3 mm. After polarization filtering with a PBS, the beam profile is slightly expanded using two spherical lenses with focal lengths of −200 mm and 250 mm. Next, the trapping beam is reflected from a piezo tip/tilt mirror for accurate beam positioning in the atomic plane. A dichroic mirror superimposes the trapping beam with the counter-propagating imaging beam. An achromatic doublet lens (Thorlabs, AC254-075-AB), which is also the primary lens of the absorption imaging system, focuses the trapping beam onto the atomic ensemble. To determine the spot size at the atomic position, a mirror was temporarily placed after the piezo tip/tilt mirror and the reflected beam was focused onto a camera by a duplicate of the achromatic doublet lens. We observe a radially symmetric beam profile with a waist of $w_{v,0} = 12.5\,\mu\text{m}$ along the $x$- and $z$-axis.

### 4.3.2 Dipole Trapping Potential

To calculate the trapping potential, we assume that the horizontal beam is an elliptical Gaussian mode with intensity [50, 141]

$$I_h(\boldsymbol{r}) = \frac{2P_h}{\pi w_y(x) w_z(x)} e^{-2\left(\frac{y^2}{w_y(x)^2}+\frac{z^2}{w_z(x)^2}\right)}, \tag{4.3}$$

where $P_h$ is the power, $w_y(x) = w_{y,0}\sqrt{1+x^2/x_{R,y}^2}$ and $w_z(x) = w_{z,0}\sqrt{1+x^2/x_{R,z}^2}$ are the spot sizes, and $x_{R,y} = \pi w_{y,0}^2/\lambda_{\mathrm{ODT}}$ and $x_{R,z} = \pi w_{z,0}^2/\lambda_{\mathrm{ODT}}$ are the Rayleigh lengths. Similarly, we assume a vertical Gaussian beam with intensity

$$I_v(\boldsymbol{r}) = \frac{2P_v}{\pi w_v(y)^2} e^{-2\frac{x^2+z^2}{w_v(y)^2}}, \tag{4.4}$$

where $P_v$ is the power, $w_v(y) = w_{v,0}\sqrt{1+y^2/y_R^2}$ is the spot size, and $y_R = \pi w_{v,0}^2/\lambda_{\mathrm{ODT}}$ is the Rayleigh length. The dipole potential [50]

$$U_{\mathrm{dip}}(\boldsymbol{r}) = -\frac{\mathrm{Re}(\alpha)}{2\epsilon_0 c}(I_h(\boldsymbol{r}) + I_v(\boldsymbol{r})) \tag{4.5}$$

with the complex dynamic polarizability $\alpha$ is expanded to second order for small values of $x$, $y$ and $z$

$$U_{\mathrm{dip}}(\boldsymbol{r}) \approx U_{\mathrm{dip}}(0) + \frac{1}{2}m\left(\omega_x^2 x^2 + \omega_y^2 y^2 + \omega_z^2 z^2\right), \tag{4.6}$$

with the atomic mass $m = 86.91\,\mathrm{u}$ of $^{87}\mathrm{Rb}$ and the trapping frequencies

$$\omega_i = \sqrt{\omega_{i,h}^2 + \omega_{i,v}^2} \tag{4.7}$$

for $i \in \{x, y, z\}$. Here, we abbreviated the trapping frequencies of the horizontal beam

$$(\omega_{x,h}, \omega_{y,h}, \omega_{z,h}) = \sqrt{-\frac{U_{h,0}}{m}}\left(\sqrt{\frac{1}{x_{R,y}^2}+\frac{1}{x_{R,z}^2}}, \frac{2}{w_{y,0}}, \frac{2}{w_{z,0}}\right), \quad U_{h,0} = -\frac{\mathrm{Re}(\alpha)}{\epsilon_0 c}\frac{P_h}{\pi w_{y,0} w_{z,0}} \tag{4.8}$$

and the trapping frequencies of the vertical beam

$$(\omega_{x,v}, \omega_{y,v}, \omega_{z,v}) = \sqrt{-\frac{U_{v,0}}{m}}\left(\frac{2}{w_{v,0}}, \frac{\sqrt{2}}{y_R}, \frac{2}{w_{v,0}}\right), \quad U_{v,0} = -\frac{\mathrm{Re}(\alpha)}{\epsilon_0 c}\frac{P_v}{\pi w_{v,0}^2}. \tag{4.9}$$

The density distribution for $N$ atoms in a harmonic trap is [50]

$$n(\boldsymbol{r}) = n_{\mathrm{peak}} e^{-\frac{x^2}{2\sigma_x^2}-\frac{y^2}{2\sigma_y^2}-\frac{z^2}{2\sigma_z^2}}, \qquad n_{\mathrm{peak}} = \frac{N}{(2\pi)^{3/2}\sigma_x\sigma_y\sigma_z}, \qquad \sigma_i = \sqrt{\frac{k_B T}{m\omega_i^2}}, \tag{4.10}$$

and, for temperatures far above quantum degeneracy, the peak phase space density is

$$\mathcal{D} = n_{\mathrm{peak}}\lambda_{\mathrm{dB}}^3 = N\left(\frac{\hbar\bar{\omega}}{k_B T}\right)^3 \tag{4.11}$$

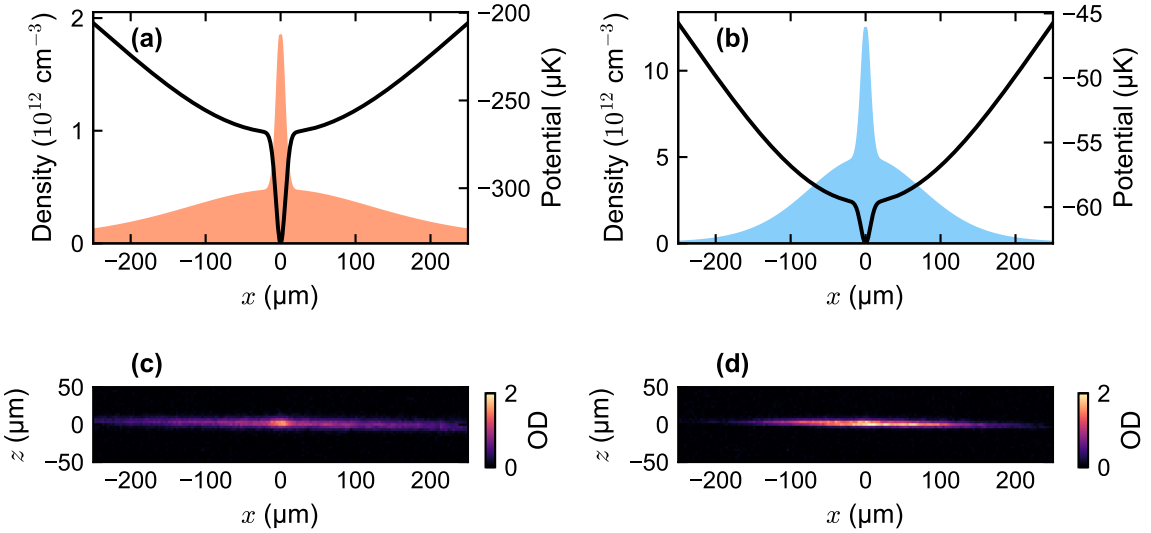


**Figure 4.6:** Atomic density distribution in the crossed-beam ODT before (a,c) and after (b,d) Raman cooling. The shaded area in (a) and (b) shows the calculated atomic density profile along the horizontal trap axis. The solid line indicates the trapping potential $U(x,0,0)/k_B$. Corresponding in-situ absorption images are shown in (c) and (d).

with $\bar{\omega} = (\omega_x\omega_y\omega_z)^{1/3}$ and the thermal de Broglie wavelength $\lambda_{\mathrm{dB}} = \sqrt{2\pi\hbar^2/mk_BT}$.

For the experiments presented in chapter 6, $N = 260$ atoms at 0.44 µK are prepared in the crossed-beam ODT, using the techniques described in Secs. 4.4 and 4.5. The final power of the horizontal and vertical trapping beam is 4.5 mW and 5 mW, respectively. Using the real part of the dynamic polarizability $\mathrm{Re}(\alpha) = 687.3$ a.u. from Ref. [4], with 1 a.u. $= 1.649 \times 10^{-41}$ J/(V/m)$^2$, we calculate $(\omega_{x,h}, \omega_{y,h}, \omega_{z,h})/2\pi = (0.01, 0.34, 0.46)$ kHz, $(\omega_{x,v}, \omega_{y,v}, \omega_{z,v})/2\pi = (0.44, 0.01, 0.44)$ kHz, and $(\omega_x, \omega_y, \omega_z)/2\pi = (0.44, 0.34, 0.64)$ kHz.[3] The agreement with the measured trapping frequencies, see Fig. 4.5, is moderate. At a temperature of 0.44 µK, RMS ensemble radii of $(\sigma_x, \sigma_y, \sigma_z) = (3.3, 4.5, 1.7)$ µm are obtained from the measured trapping frequencies. The three values are smaller than the estimated blockade radius of 7 µm, see Sec. 5.5. For 260 atoms, the peak density in the trap is $n_{\mathrm{peak}} = 6.5 \times 10^{11}$ cm$^{-3}$ and the peak phase space density is $1.4 \times 10^{-2}$.

### 4.3.3 Dipole Trap Loading

Both dipole trapping beams are already turned on during the MOT loading phase. After 0.5 s of loading, the MOT parameters are altered for 30 ms similar to Ref. [81] in order to enhance the transfer of atoms into the ODT. In particular, we increase the red detuning to 50 MHz and drastically reduce the repumping power to 1 µW. We refer to this stage as MOT compression. Subsequently, PGC is performed. Also here, we found that changing

[3] A numerical calculation which includes gravitational sag yields an about 10% lower value for $\omega_y$ and a trap depth of 0.9 µK.

the parameters improves the transfer into the ODT. Hence, a longer PGC time of 50 ms and a lower initial cooling power of 20 mW are used.

As our cooling scheme can produce larger atomic ensembles than necessary for the experiment, we deliberately lower the trapping beam powers during the loading phase in order to obtain the desired final atom number. For the measurements in chapter 6, the horizontal (vertical) beam has an initial power of 0.23 W (0.05 W). In daily alignment, these values are often varied to fine-tune the number of atoms.

For the subsequent MOT compression and PGC phase, the beam power is increased to its maximum value of 0.45 W (0.1 W). Keeping the crossed-beam ODT on for 150 ms after PGC, we measure a trapped atom number of $2.1 \times 10^4$ at a temperature of 46 µK. From a numerical calculation of the atomic density distribution $n(\boldsymbol{r}) \propto \exp(U_{\mathrm{dip}}(\boldsymbol{r})/k_B T)$ using Eqs. (4.3)–(4.5), we find that this corresponds to $n_{\mathrm{peak}} = 2 \times 10^{12}\,\mathrm{cm}^{-3}$ and $\mathcal{D} = 4 \times 10^{-5}$. The calculated density profile along the $x$-axis is shown in Fig. 4.6 (a). We note that a dimple-trap configuration is obtained, in which a low-density reservoir is in contact with a high-density trapping region. This may have a beneficial impact onto the evaporation dynamics in this trap, similar to Refs. [18, 80] which used more elaborate dimple-traps for all-optical production of BECs.

## 4.4 Raman Cooling

To reach the above mentioned parameters for the experiments in chapter 5, an improvement of the peak phase space density of more than two orders of magnitude is necessary. Hence, an additional cooling method is required. To this end, we employ the first two stages of the Raman cooling scheme reported in Ref. [159] in our crossed-beam ODT. This relatively new scheme is extremely simple and fast, which makes it attractive for many ultracold atom experiments. In fact, we do not exploit the full potential of the method, which is able to produce BECs. As an additional benefit, it already optically pumps the atomic ensemble into the desired Zeeman state.

In our setup, we initially implemented, optimized, and characterized Raman cooling using only the horizontal ODT beam. The results are presented in detail in Ref. [126]. The vertical ODT beam was added later. This section starts with an explanation of the Raman cooling scheme. Next, its optimization and the results from Ref. [126] are briefly summarized. Finally, the extension of the scheme to the crossed-beam ODT is discussed. Note that the type of Raman cooling considered here is not to be confused with sideband-resolved Raman cooling schemes, see e.g. Ref. [63], which can achieve similar performance but require much higher trap frequencies.

### 4.4.1 Physical Mechanism

The basic idea of the scheme is to use a Raman transition for Doppler cooling. Similar techniques have already been demonstrated three decades ago [72, 84]. Traditional Doppler cooling as in a MOT uses an atomic two-level transition between a ground state $|1\rangle$ and an excited state $|2\rangle$. In this situation, the achievable temperature is on the order of the Doppler limit $k_B T = \hbar\Gamma/2$ [96], which is determined by the excited state decay rate $\Gamma$.

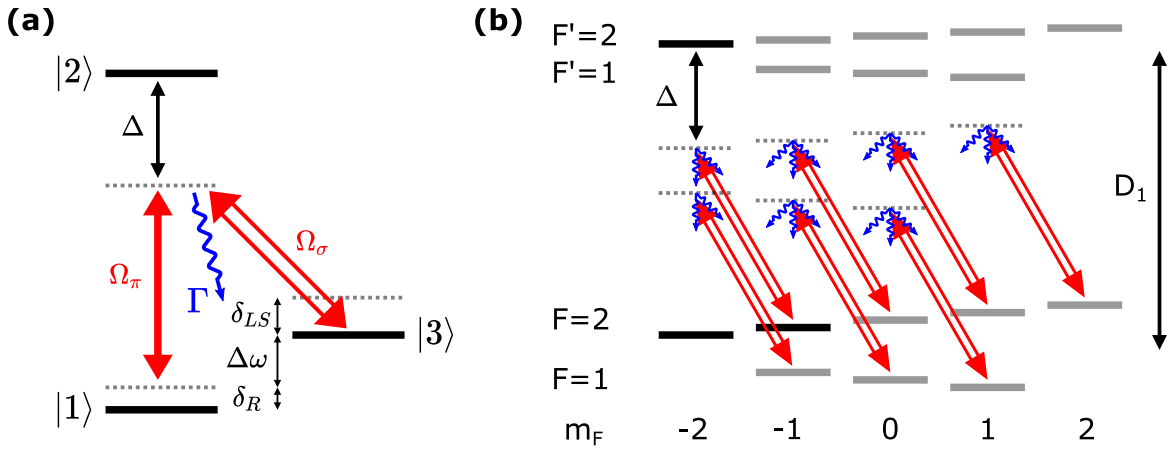


**Figure 4.7:** Atomic level scheme for Raman cooling. (a) Relevant levels for a cooling cycle. Weak $\pi$ light and strong $\sigma^-$ light induce a velocity selective Raman coupling (red arrows) which transfers population from state $|1\rangle$ to $|3\rangle$, removing kinetic energy because of a red two-photon detuning, somewhat similar to Doppler cooling. Atoms are repumped to state $|1\rangle$ by spontaneous scattering of $\sigma^-$ photons on the $|2\rangle \leftrightarrow |3\rangle$ transition. The probabilities for spontaneous decay (blue arrow) to the states $|1\rangle$, $|3\rangle$, and $|5^2S_{1/2}, F = 1, m_F = -1\rangle$ are 1/3, 1/6, and 1/2 respectively [96]. Further explanations are provided in the main text. (b) Complete hyperfine and Zeeman manifolds for the $5^2S_{1/2}$ and $5^2P_{1/2}$ states in $^{87}$Rb. Black bars mark the levels from (a). Optical pumping into state $|1\rangle$ is achieved by residual spontaneous scattering of the fairly far detuned $\sigma^-$ Raman light.

For Raman cooling, a third atomic energy level $|3\rangle$, which is usually another ground state, is added to the scheme. A cooling cycle consists of a velocity-selective Raman transition from $|1\rangle$ to $|3\rangle$, which removes kinetic energy, followed by a repumping process via the excited state $|2\rangle$. By decreasing the repumping rate, which takes the role of $\Gamma$ in traditional Doppler cooling, the Doppler limit can become arbitrarily small in a Raman cooling scheme. Instead, the final temperature is on the order of an effective recoil temperature, which stems from the energy deposited during the repumping process.

In the scheme from Ref. [159], the states $|1\rangle = |5^2S_{1/2}, F = 2, m_F = -2\rangle$, $|2\rangle = |5^2P_{1/2}, F' = 2, m'_F = -2\rangle$, and $|3\rangle = |5^2S_{1/2}, F = 2, m_F = -1\rangle$ in $^{87}$Rb are used. Atomic level diagrams are shown in Fig. 4.7. The transitions $|1\rangle \leftrightarrow |2\rangle$ and $|2\rangle \leftrightarrow |3\rangle$ have very similar resonance frequencies and belong to the $D_1$ line at a wavelength of 795 nm. The Raman transition is induced by a weak $\pi$-polarized light field with Rabi frequency $\Omega_\pi$ and a high intensity $\sigma^-$-polarized light field with Rabi frequency $\Omega_\sigma$. Both beams are red detuned from the atomic transitions by about $\Delta = -4.33$ GHz. This value was identified by Ref. [159] as beneficial because it reduces losses due to inelastic light-assisted collisions by avoiding photoassociation resonances. Although we just copied that detuning without further investigation, we indeed observed a degradation of the cooling performance whenever the cooling laser jumped to a different frequency.

The two-photon Rabi frequency of the Raman transition is $\Omega_R = \Omega_\pi \Omega_\sigma / (2\Delta)$ and the two-photon detuning is $\delta_R = \Delta\omega - \omega_{31}$, where $\omega_{31} = \omega_3 - \omega_1$ is the angular resonance

frequency of the transition $|1\rangle \leftrightarrow |3\rangle$ and $\Delta\omega = \omega_\pi - \omega_\sigma$ is the angular frequency difference between the two Raman beams. If the wave vectors of the $\pi$ and $\sigma^-$ beam are $\boldsymbol{k}_\pi$ and $\boldsymbol{k}_\sigma$, the Raman coupling acts resonantly onto atoms with a two-photon Doppler shift $\boldsymbol{k}_R \cdot \boldsymbol{v} = \delta_R$, where $\boldsymbol{k}_R = \boldsymbol{k}_\pi - \boldsymbol{k}_\sigma$ and $\boldsymbol{v}$ is the atomic velocity. Hence, specific velocity classes of atoms can be selectively addressed by tuning $\delta_R$.

The strong $\sigma^-$-polarized light field additionally performs a second task, which is the repumping process $|3\rangle \rightarrow |1\rangle$. Due to the large detuning $\Delta$, a relatively high intensity of $4.7\,\frac{\mathrm{W}}{\mathrm{cm}^2}$ is required to obtain a scattering rate of $\Gamma_{sc} = 4.1\,\mathrm{ms}^{-1}$ as in Ref. [159]. This simultaneously causes a light shift of $\delta_{LS} = \Delta\Gamma_{sc}/\Gamma = 2\pi \times (-500\,\mathrm{kHz})$ on state $|3\rangle$ [159]. As the $\sigma^-$-polarized light does not couple to $|1\rangle$ due to dipole selection rules and because the polarization is carefully aligned to be $\sigma^-$ in the experiment, there is no light shift on state $|1\rangle$. Hence, $\delta_{LS}$ contributes to the Raman detuning $\delta_R$. For that reason, it is crucial that the $\sigma^-$ beam has a sufficiently homogeneous intensity across the atomic ensemble.

Conveniently, the $\sigma^-$ light pumps atoms into state $|1\rangle$ also from all other Zeeman states of the ground state manifold. All these processes occur with significant scattering rates because the hyperfine splittings of the ground- and excited-state manifold are not much larger than $\Delta$. Moreover, these optical pumping rates exhibit negligible velocity dependence because the light is far detuned. As a consequence, the cooling scheme prepares the atomic ensemble in state $|1\rangle$ and no additional optical pumping steps are required. After a stimulated Raman transition from state $|1\rangle$ to $|3\rangle$, it takes an average of 3 scattering events to transfer an atom back to state $|1\rangle$. As explained in the supplement of Ref. [159], this translates to an effective recoil limit of $2.8\,\mu\mathrm{K}$.

Unlike textbook explanations of standard Doppler cooling, the scheme does not require counter-propagating light beams. This is because of the presence of the dipole trap. In one dimension, a harmonic trap periodically reverses the direction of the velocity which means that all atoms can be cooled in one dimension without a need for counter-propagating beams. In a three-dimensional harmonic potential described by Eq. (4.6), the components of the atomic motion along the $x$-, $y$-, and $z$-axes are decoupled from each other. To achieve cooling along all three axes, all trapping frequencies must differ from one another and the transferred momentum during a velocity selective Raman transition $\hbar\boldsymbol{k}_R$ must have a nonzero component along each axis. This is ensured by choosing $\boldsymbol{k}_\pi$ and $\boldsymbol{k}_\sigma$ appropriately.

### 4.4.2 Implementation and Characterization

As indicated in Fig. 4.3, the $\pi$-polarized Raman light is overlapped with two of the MOT beams. This solution is chosen because it requires little optical components and no additional optical access. As a result, this light field is not really $\pi$ polarized at the atomic position. But this has little effect on the performance of the cooling scheme because the light field generates a negligible spontaneous scattering rate and because its $\sigma^+$ and $\sigma^-$ components can only induce very far red-detuned Raman transitions due to the large Zeeman splitting. As each of the two beams is retroreflected, four different directions of $\boldsymbol{k}_\pi$ are available, even though this would not be required to achieve cooling along all three trap axes, as explained above. The $\sigma^-$-polarized pumping beam is overlapped with the imaging beam and propagates along the positive $y$-axis.

Both Raman light fields are power stabilized. The $\sigma^-$-polarized pumping beam has a

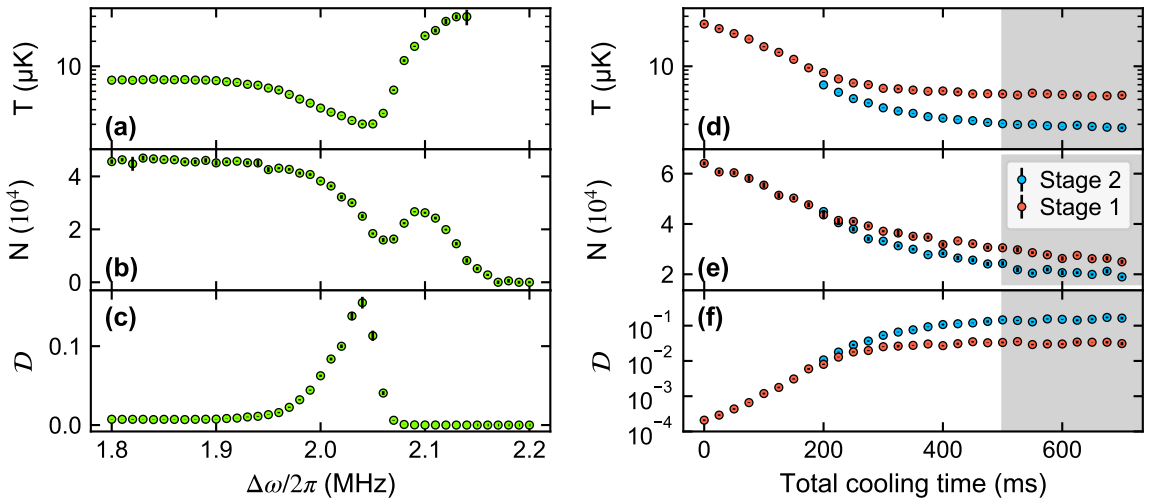


**Figure 4.8:** Optimization of Raman cooling. The panels on the left-hand side show the atomic temperature (a), atom number (b), and peak phase space density (c) after stage 2, as a function of the frequency difference between the two Raman beams. The optimal phase space density of $\mathcal{D} = 0.15$ is achieved at $\Delta\omega/2\pi = 2.04\,\mathrm{MHz}$, which approximately coincides with the minimum of the atomic temperature in (a). The panels on the right-hand show the evolution of temperature (d), atom number (e), and peak phase space density (f) as a function of the total cooling time. Adding a second Raman stage (blue datapoints) with modified parameters starting at 200 ms increases the achieved $\mathcal{D}$ by almost an order of magnitude. Cooling beyond 500 ms (gray shaded region) leads to little improvement in $\mathcal{D}$.

power of 10 mW and an elliptical waist at the atomic position with spot sizes of $w_x = 2\,\mathrm{mm}$ and $w_z = 180\,\mu\mathrm{m}$ along the $x$- and $z$-axis. This ensures a large intensity while keeping the beam profile sufficiently homogeneous across the trapped ensemble, as discussed in the previous section. For an atom in state $|3\rangle$, the calculated scattering rate is $\Gamma_{\mathrm{scat}} = 1/(0.6\,\mathrm{ms})$ and the light shift is $\delta_{LS} = 2\pi \times (-0.19\,\mathrm{MHz})$. The two $\pi$ beams have a total power up to 1 mW. By applying a magnetic field of 3.38 G along the negative $y$-axis, a differential Zeeman shift of $\delta_Z = 2\pi \times 2.36\,\mathrm{MHz}$ between the states $|1\rangle$ and $|3\rangle$ is created. Overall, this results in a Raman detuning of $\delta_R = \delta_Z + \delta_{LS} - \Delta\omega$. To adjust $\delta_R$, the frequency difference $\Delta\omega$ between the $\pi$ beam and the $\sigma^-$ beam is varied using an AOM.

Similar to Ref. [159], we optimize the achieved phase space density by dividing the cooling time into two stages with different beam powers, trap depth, and Raman detuning. This makes sense because the atomic density and velocity distributions change during the cooling process, shifting the optimal cooling parameter values away from the initial setting. For instance, a larger Raman detuning is favorable in the beginning because this addresses atoms at high velocity and transfers them to lower velocity. As the ensemble gets colder, less atoms with the addressed velocity are available and the cooling speed drops, making a lower Raman detuning beneficial. For lower detuning, a lower Raman Rabi frequency narrows the transition linewidth and reduces unwanted coupling to low-velocity atoms,

which would otherwise be heated. To reduce light-assisted collisions as the atomic density increases, it is helpful to reduce the atomic density by decreasing the trapping confinement.

For each stage, the cooling parameters are optimized for maximum final phase space density. As an example, Fig. 4.8 (a)–(c) illustrates the optimization of the Raman detuning during the second cooling stage. To understand the dependence of the temperature in (a) on $\Delta\omega$, we note that, first, for very small $\Delta\omega$, the light is too far detuned to have an effect, second, for increasing $\Delta\omega$ the number of atoms addressed by the Raman light increases, which causes cooling, and third, for too large $\Delta\omega$, the two-photon detuning of the Raman light is no longer red, thus causing heating. This has the following consequences for the atom number in (b). When increasing $\Delta\omega$, starting from small values, the initial decrease in temperature causes the density of the atomic sample to increase because of the presence of the dipole trap. This causes increased atom loss, presumably due to light-assisted inelastic collisions. At larger $\Delta\omega$, the temperature returns to the value, which it had without cooling. This causes the atom number to recover, too, at least somewhat. For even larger $\Delta\omega$, the temperature increases above its value without cooling, which causes atom loss due to evaporation. This explains the appearance of the local maximum of the atom number seen in (b).

Similar measurements were done for the power of the cooling beams and the dipole trap, see Ref. [126]. It bears noting that residual $\pi$- or $\sigma^+$-polarized components of the pumping beam heat the sample by pumping atoms out of the dark state $|1\rangle$. Hence, we optimized the polarization and the magnetic field direction by applying Raman pumping light for a certain time and minimizing the resulting atom loss. In contrast, changing the magnitude of the magnetic field did not lead to a significant change of the cooling performance.

We now summarize the results of the optimization, which is described in detail in Ref. [126]. Both stages use a pumping beam power of 10 mW. Stage 1 runs at a $\pi$ beam power of 1 mW, a trapping beam power of 0.45 W, and $\Delta\omega = 1.98$ MHz. As illustrated in Fig. 4.8 (d)–(f), stage 2 is applied after 200 ms. Here, the cooling parameters are changed to a $\pi$ beam power of 0.2 mW, a trapping beam power of 0.27 W, and $\Delta\omega = 2.04$ MHz. After the total cooling time of 500 ms, a temperature of 2.0 µK is achieved with $2.5 \times 10^4$ atoms, resulting in a peak phase space density of $\mathcal{D} = 0.15$.[4]

### 4.4.3 Cooling in the Crossed-Beam Trap

Instead of repeating the complete optimization for the crossed-beam ODT, we found that it was straightforward to reach sufficient performance for the experiments in chapter 6 by simply choosing suitable powers for the ODT beams, without modifying the other cooling parameters. To avoid atom loss, it makes sense to operate the trapping beams at full power in the beginning, while the atomic temperature is not yet much lower than the trap depth. However, as the atomic temperature drops during the first Raman cooling stage, the high atomic density region of the dimple potential may give rise to an increased loss rate due to inelastic collisions. Hence, the power of both trapping beams is lowered for stage 2.

[4] There is a mistake in the main text of Ref. [126], which lists a slightly higher phase space density at a higher temperature and a lower atom number.

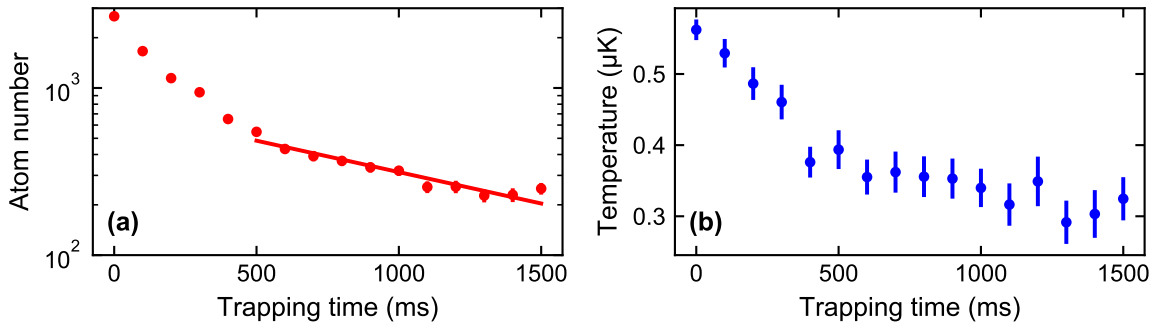


**Figure 4.9:** Evolution of (a) atom number and (b) temperature after expansion in the crossed-beam ODT. In the first 500 ms, the atom number decays relatively fast indicating evaporation from this shallow trap. Subsequently, atom number and temperature stabilize. The solid line in (a) is an exponential fit to the data between 500 ms and 1500 ms, yielding a $1/e$ lifetime of 1.2(1) s.

With a horizontal (vertical) beam power of 100 mW (5 mW) during stage 2, we finally obtain $1.8 \times 10^4$ atoms at a temperature of 3.4 μK. From our numerical calculation of the atomic density distribution in the trap, these numbers result in $n_{\mathrm{peak}} = 1 \times 10^{13}\,\mathrm{cm}^{-3}$ and $\mathcal{D} = 1 \times 10^{-2}$, see Fig. 4.6 (b). The phase space density is already close to the value used for the experiments in chapter 6.

## 4.5 Expansion in the Dipole Trap

According to Eq. (3.1), high retrieval efficiency of the control photon requires low atomic temperature. As we can prepare many more atoms with the Raman cooling method than needed, it makes sense to trade atom number for lower temperature. This is achieved by decreasing the horizontal beam power, which reduces the confinement and depth of the ODT. As a consequence, the atomic medium expands and high-velocity atoms escape from the trap.

We linearly ramp the horizontal ODT power from 100 mW to 4.5 mW in 100 ms. Compared to the final trapping frequencies, this ramping time is relatively slow. Hence, we assume that the change of the trapping potential is to a good approximation adiabatic. However, compared to the timescale on which thermalization of the ensemble is expected to occur, the ramp is fast. Hence, we expect that there is little evaporative cooling. In such a situation, the peak phase space density should be approximately conserved. Starting at $\mathcal{D} = 0.01$, we expect a final temperature of $T = (N/\mathcal{D})^{1/3}\hbar\bar{\omega}/k_B$. At the atom number of $N = 260$, which we use for the experiment, we expect $T = 0.5\,\mu\mathrm{K}$ from these considerations, which is close to the measured value $T = 0.44(2)\,\mu\mathrm{K}$. At this temperature, Eq. (3.1) predicts a thermal coherence time for the stored control photon of $\tau_R = 31\,\mu\mathrm{s}$, when assuming minimal two-photon recoil $k_R = 2\pi(1/480\,\mathrm{nm} - 1/780\,\mathrm{nm})$.

Fig. 4.9 shows the evolution of atom number and temperature as a function of the hold

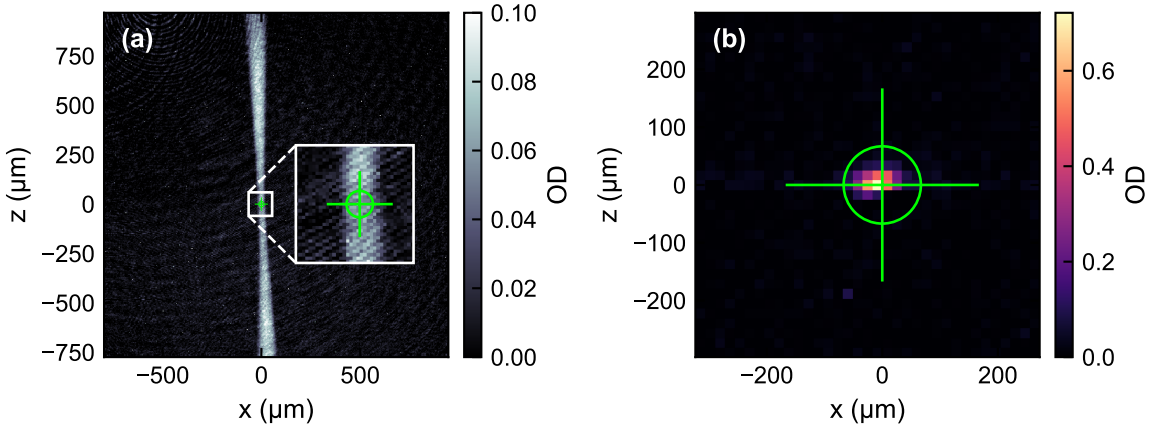


**Figure 4.10:** Overlap between dipole trap and cavity mode. Panel (a) shows results from a measurement that reveals the position of the cavity mode (white area) on the camera image, as explained in the main text. The center of the cavity mode (green crosshair) is determined from a fit. The inset contains a zoom into the region marked by the white rectangle. Panel (b) shows an average of ten in-situ absorption images of atomic ensembles in the crossed-beam ODT, for the same zoomed region on the camera image. The atomic position is close to the previously determined center of the cavity mode (green crosshair).

time in the final trap. Because of the fast initial evaporation, we wait 500 ms before we perform experiments with the ensemble.

## 4.6 Overlap between Dipole Trap and Cavity Mode

The final task left for completing the preparation of the atomic sample is to overlap it with the cavity mode. We achieve this by making use of the absorption imaging system.

As a first step, the location of the cavity mode on the camera image is determined. To this end, atoms are prepared in the 3D MOT and then pumped into the $F = 1$ hyperfine ground state, which does not couple to the imaging light. An absorption image is taken while sending 5 nW of repumping light into the cavity, which for this measurement is tuned on resonance with the repumping transition. Atoms which couple to the cavity mode are repumped and hence become visible in the absorption image, as shown in Fig. 4.10 (a). This reveals the position of the cavity mode.

As a second step, the *horizontal* position of the ODT is moved to the center of the cavity mode on the camera image. To this end, atomic ensembles are prepared as in a usual experiment, i.e. following the steps in Secs. 4.1–4.5 and without sending repumping light into the cavity. After each preparation cycle, an absorption image reveals the position of the atomic ensemble trapped in the ODT. An example of such an absorption image is shown in Fig. 4.10 (b). In an iterative procedure, the alignment of the ODT beams is changed until the position of the atomic ensemble in the camera image coincides with the previously determined position of the cavity mode waist.

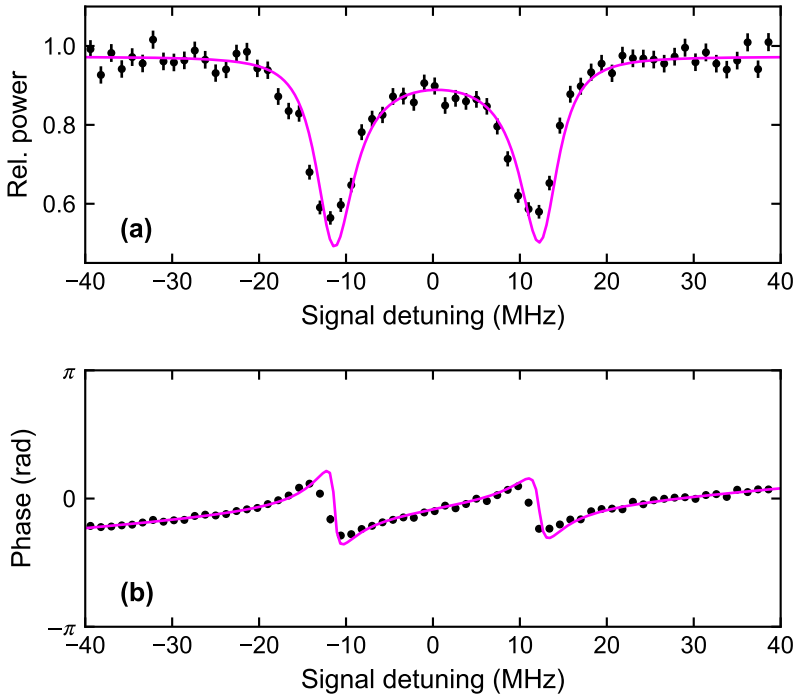


**Figure 4.11:** Normal modes of the atom-cavity system. Plotted are (a) the relative output power and (b) the phase $\phi$ of the output state when sending $D$-polarized target light into the dual-rail setup, while scanning the signal detuning $\Delta_c/2\pi$. The solid lines in (a) and (b) show fits to the data using Eqs. (4.12) and (4.15), respectively. The fit to the data in (a) yields a cooperativity of $C = 20.8(3)$.

In a third step, the *vertical* ODT position is optimized by maximizing the observed normal mode splitting when reflecting target signal light from the cavity, see Sec. 4.7.

## 4.7 Normal Modes of the Atom-Cavity System

As a final result of this chapter, a normal mode spectrum of the coupled atom-cavity system is shown in this section. This measurement reveals the cooperativity of the system and confirms that the previously described preparation steps were successfully implemented. To this end, the cavity resonance is tuned near the cycling transition $|g\rangle \leftrightarrow |e\rangle$, where $|g\rangle = |5^2S_{1/2}, F = 2, m_F = -2\rangle$ and $|e\rangle = |5^2P_{3/2}, F' = 3, m'_F = -3\rangle$. Driving this transition requires $\sigma^-$ light. The polarization convention for $\sigma^-$ is relative to the positive $z$ axis (see Fig. 3.2) which essentially represents the direction of the atomic spins. The polarization convention for $L$ and $R$, however, is relative to the wave vector of the light. As the control (target) signal light has a wave vector parallel (antiparallel) to the positive $z$ axis, it is $R$ ($L$) polarized. In addition, a magnetic field of 1.0 G pointing along the positive $z$-axis is applied. Due to the polarization mode splitting of the cavity, see Fig. 3.7, only one of the two signal light fields can be exactly on resonance with the

atomic transition. Our choice is such that the control photon is resonant. Hence, there is a small atom-cavity detuning $\Delta_{ac} = \omega_{ge} - \omega_c = 2\pi \times 0.9\,\mathrm{MHz}$ for the target photon.

The experimental sequence for the data shown here and in chapter 6 is the following. After 500 ms of MOT loading and 500 ms of Raman cooling, the ODT is expanded in 100 ms. As the magnetic field is $\boldsymbol{B} = (0, -3.4, 0)$ G during Raman cooling, the next step is to rotate the magnetic field vector to $\boldsymbol{B} = (0, 0, 1.0)$ G while holding the atomic ensemble in the expanded crossed-beam ODT. To conserve the atomic spin polarization, this rotation is performed slowly in 200 ms and a small magnetic field is avoided at all times. As there is fast initial evaporation in the expanded ODT, see Sec. 4.5, the atomic medium is held in the ODT for another 300 ms before starting the data acquisition stage, which takes 1 s. At the beginning of this stage, an atom number of 258(7) at a temperature of 0.44(2) µK was inferred from absorption images. During this period, a sequence of control and target signal and coupling light pulses is repeatedly sent onto the atomic medium, at a repetition rate of 10 kHz.

The data in Fig. 4.11 (a) and (b) are recorded using 1 µs long $D$ polarized target light pulses containing 0.19 photons on average with a temporal envelope according to Eq. (2.79). These pulses are sent through the target path of the dual-rail setup and the intensity and polarization of the output light field is measured as a function of the signal laser detuning from the cavity resonance.

The expected output power of the light pulses is

$$P_{\mathrm{out}}(\Delta_c) = \frac{1}{2} P_{\mathrm{in}} \left( T_H + \frac{T_V}{|\mathcal{R}_{\mathrm{empty}}|^2} |\mathcal{R}(\Delta_c)|^2 \right), \tag{4.12}$$

where the measured on-resonance transmission through the cavity path (bypass) is $T_V = 0.91$ ($T_H = 0.97$), the measured on-resonance reflectivity of the cavity is $|\mathcal{R}_{\mathrm{empty}}|^2 = 0.932$, and the cavity reflection coefficient $\mathcal{R}(\Delta_c)$ is given by Eq. (2.32) with $\beta = 0.983$, $\kappa/2\pi = 2.3\,\mathrm{MHz}$, and

$$C_{\mathrm{eff}} = C \frac{\Gamma_e}{\Gamma_e - 2i(\Delta_c - \Delta_{ac})} \tag{4.13}$$

according to Eqs. (2.31), (2.33), and (2.35) with $\Omega_{\mathrm{co}} = 0$ and $\Delta_s = \Delta_c - \Delta_{ac}$. In Fig. 4.11 (a), we plot $P_{\mathrm{out}}(\Delta_c)/P_{\mathrm{in}}$ and obtain $C = 20.8(3)$ from a fit using Eq. (4.12).

The output polarization state is

$$|\psi_{\mathrm{out}}\rangle = a_H |H\rangle - a_V e^{i\phi} |V\rangle + |\psi_{\mathrm{loss}}\rangle, \tag{4.14}$$

where $a_H$ and $a_V$ are two real and positive constants and $|\psi_{\mathrm{loss}}\rangle$ represents loss. We measure the phase $\phi$ using quantum state tomography of the output photons.[5] Taking into account the path length difference $\Delta L_t = 73\,\mathrm{cm}$ between the cavity path and the bypass, we expect to obtain

$$\phi(\Delta_c) = \phi_0 + \arg(\mathcal{R}(\Delta_c)) + \frac{\Delta L_t}{c} \Delta_c. \tag{4.15}$$

[5] More precisely, we measure the normalized Stokes parameters $S_{HV}$, $S_{DA}$, and $S_{RL}$ [12, 57] of the output polarization state and use $S_{DA} = -V \cos\phi$ and $S_{RL} = V \sin\phi$, where $V$ is the visibility.

The offset phase $\phi_0$ is determined by the setpoint of the target bypass path length stabilization. For the data in Fig. 4.11 (b), a fit using Eq. (4.14) with the previously obtained value $C = 20.8$ yields $\phi_0 = 0.9(1)\pi$.

We can also obtain an estimate for the expected cooperativity from the measured atom number by taking into account the atomic density distribution in the trap. To this end, we replace

$$\sum_{\ell=1}^{N} |g_\ell|^2 \to \int d^3\boldsymbol{r}\; n(\boldsymbol{r}) g^2 \exp\left(-2\frac{x^2+y^2}{w_c^2}\right) \tag{4.16}$$

in Eq. (2.35), where the $z$-dependence of the cavity mode function has been neglected because the atomic sample size is much smaller than the Rayleigh range. Combining this with $n(\boldsymbol{r})$ from Eq. (4.10) yields

$$C = N\frac{g^2}{\kappa\Gamma_e/2}\frac{w_c^2}{\sqrt{(w_c^2+4\sigma_x^2)(w_c^2+4\sigma_y^2)}}. \tag{4.17}$$

With $g/2\pi = 1.0\,\mathrm{MHz}$, $\kappa/2\pi = 2.3\,\mathrm{MHz}$, $\Gamma_e/2\pi = 6.07\,\mathrm{MHz}$, $\sigma_x = 3.3\,\mu\mathrm{m}$, $\sigma_y = 4.5\,\mu\mathrm{m}$, $w_c = 8.5\,\mu\mathrm{m}$, and $N = 260$, we find $C = 20$. This agrees well with the value of $C$ obtained in the above fit.

# Chapter 5

# Characterization of the Cavity Rydberg EIT System

This chapter presents calibration and characterization measurements of the cavity Rydberg EIT system which forms the basis for the optical CNOT gate in chapter 6. The complete temporal input pulse shapes of the gate protocol are provided in Sec. 5.1. The gate performance is optimized following the considerations presented in Sec. 2.7. Among other things, this implies that the temporal pulse shape of the control coupling light is chosen according to the model in Ref. [46]. The required input parameters for this model are extracted from two different types of measurements. First, cavity Rydberg EIT spectra are shown in Sec. 5.2. Second, a measurement of the decay of the write-read efficiency in a storage-and-retrieval experiment as a function of the dark time is presented in Sec. 5.3. Characterization measurements of the control and target signal pulses exiting the gate are provided in Sec. 5.4. Finally, cavity Rydberg blockade is discussed in Sec. 5.5.

## 5.1 Input Pulse Sequence

The complete temporal input pulse sequence of the gate protocol, see Sec. 2.6, is shown in Fig. 5.1. The signal input pulse envelopes are chosen according to Eq. (2.79) with $T = T_c = T_t = 1\,\mu\text{s}$ for the control and target qubit. The control (target) pulse contains $\bar{n}_c = 0.14$ ($\bar{n}_t = 0.13$) photons on average. The control (target) signal detuning from the transition $|g\rangle \leftrightarrow |e\rangle$, where $|g\rangle = |5^2S_{1/2}, F = 2, m_F = -2\rangle$ and $|e\rangle = |5^2P_{3/2}, F' = 3, m'_F = -3\rangle$, is $\Delta_s/2\pi = 0$ ($\Delta_s/2\pi = -0.9\,\text{MHz}$) such that each photon is resonant on the corresponding polarization eigenmode of the cavity, see Sec. 4.7.

The coupling light at 480 nm is sent through the concave cavity mirrors as described in Sec. 3.1. The control (target) coupling light addresses the transition from $|e\rangle$ to $|r'\rangle = |48^2S_{1/2}, F = 2, m_F = -2\rangle$ ($|r\rangle = |50^2S_{1/2}, F = 2, m_F = -2\rangle$). As with the signal light in Sec. 4.7, this implies that the control (target) coupling light is $R$ ($L$) polarized at the atomic position. The control (target) coupling detuning is set to $\Delta_{\text{co}}/2\pi = 0$ ($\Delta_{\text{co}}/2\pi = 0.9\,\text{MHz}$). These values of $\Delta_{\text{co}}$ are needed to match the single-photon detuning of the signal light. Hence, two-photon resonance $\Delta_{\text{co}} + \Delta_s = 0$ is obtained for the control and the target photon.

Unless otherwise noted, all data in this chapter were taken using the general atomic preparation procedure described in Sec. 4.7, at a magnetic field of $\boldsymbol{B} = (0, 0, 1.0)$ G and at an electric field of $\boldsymbol{E} = (0.2, 0, 0.7)\frac{\text{V}}{\text{cm}}$, see Sec. 6.3. According to Eqs. (2.9) and

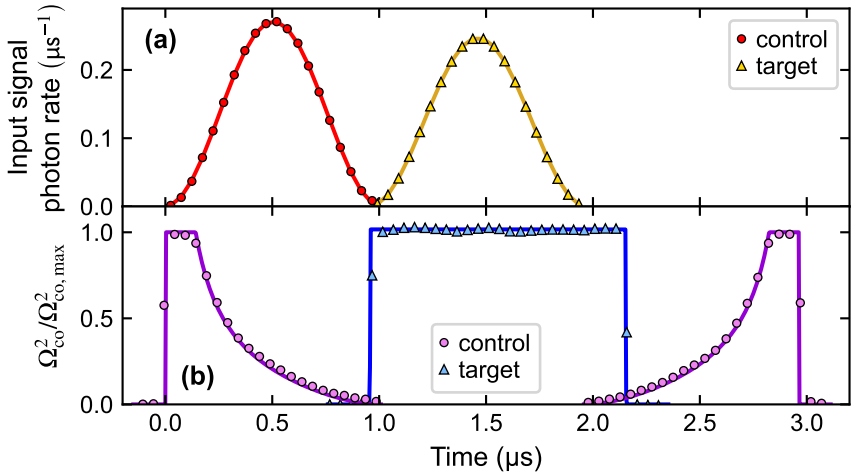


**Figure 5.1:** Input pulse sequence. Characterization measurements of the incoming control (circles) and target (triangles) signal and coupling light pulses are shown. Panel (a) contains the incoming signal photon rate as a function of time. The solid lines are fits of $|u_s(t)|^2$ from Eq. (2.79) to the data. In panel (b), the normalized power of the control (target) EIT coupling light is shown, where $\Omega_{\mathrm{co,max}}/2\pi = 20.8\,\mathrm{MHz}$ ($\Omega_{\mathrm{co,max}}/2\pi = 43.0\,\mathrm{MHz}$). The solid purple line is the optimal coupling pulse calculated numerically with Eqs. (2.50) and (2.52), which is truncated at a maximum of $\Omega_{\mathrm{co,max}}$. The solid blue line is a fitted rectangular pulse.

(2.15), Stark shifts $\Delta E_{\mathrm{Stark}}/h$ of $-10.1\,\mathrm{MHz}$ and $-13.5\,\mathrm{MHz}$ on the states $|r'\rangle$ and $|r\rangle$ are expected due to this electric field.

To optimize the write-read efficiency of the control photon, optimal coupling pulses are calculated using the model in Sec. 2.4. This requires a value for the coherence time $1/\gamma_{rg}$. Two different methods for measuring $\gamma_{rg}$ will be discussed in Secs. 5.2 and 5.3, which yield $1/\gamma_{rg} = 0.6\,\mu\mathrm{s}$ and $1/\gamma_{rg} = 7\,\mu\mathrm{s}$ in the presence and absence of EIT coupling light, respectively. When calculating optimal coupling pulses, we use the latter value $1/\gamma_{rg} = 7\,\mu\mathrm{s}$ based on the following considerations. As shown in Fig. 5.1, the optimal coupling pulse reaches its maximum power only for a relatively small fraction of the pulse duration and has much lower power for most of the remaining time. The previously quoted value of $1/\gamma_{rg} = 0.6\,\mu\mathrm{s}$ from Sec. 5.2 was measured at the maximum coupling power of 30 mW. Hence, $1/\gamma_{rg} = 0.6\,\mu\mathrm{s}$ would be a poor approximation for modeling storage and retrieval. However, obtaining $\gamma_{rg}$ from a fit to an EIT spectrum at low coupling power is difficult because the fit essentially determines $\gamma_{rg}$ from the dip at zero detuning, which becomes quite narrow in this situation and is therefore hard to resolve.[1] As a pragmatic solution, we use the value $1/\gamma_{rg} = 7\,\mu\mathrm{s}$ measured in the absence of coupling light to calculate approximately optimal coupling pulses. From the model in Sec. 2.4, we expect that this does not reduce the achieved write-read efficiency much.

[1] The linewidth of the dip in the EIT spectrum at zero detuning is essentially given by the cavity EIT linewidth $\kappa_F$. According to Eq. (2.43), $\kappa_F$ decreases with $\Omega_{\mathrm{co}}$ and eventually becomes smaller than the spectral resolution of the measurement, which is limited, for instance, by laser frequency noise.

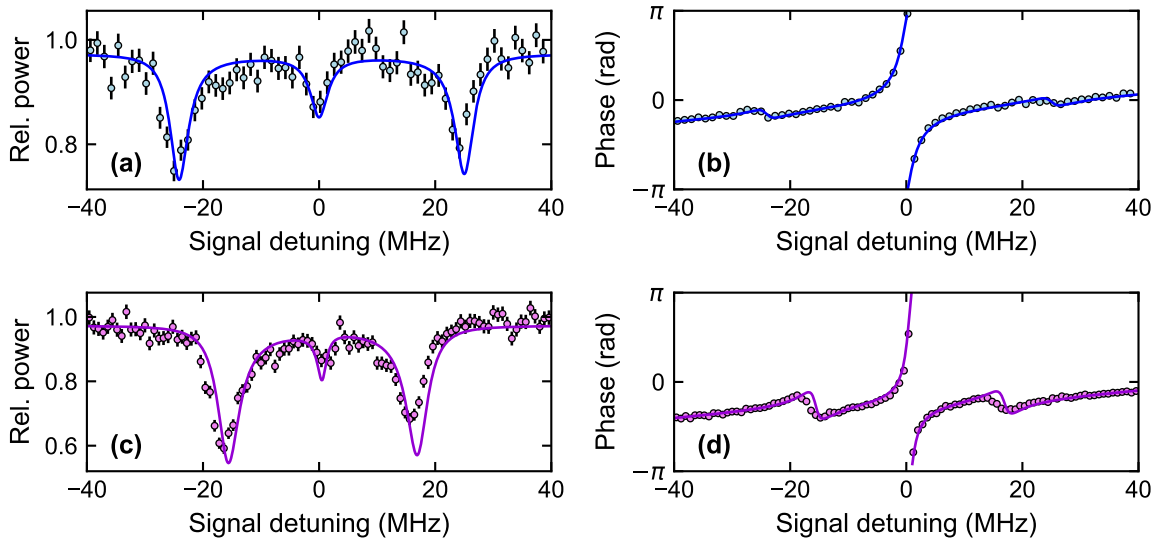


**Figure 5.2:** Cavity Rydberg EIT spectra (a,b) for the target photon and (c,d) for the control photon. (a) and (c) show the relative power and (b) and (d) show the phase of the light reflected from the cavity as a function of the signal detuning $\Delta_c/2\pi$. An EIT feature at zero detuning is clearly observed, which causes a $2\pi$ phase boost when tuning $\Delta_c$ through zero. Fits (lines) reveal the coupling Rabi frequency $\Omega_{\mathrm{co}}$, the coherence time $1/\gamma_{rg}$, and the cooperativity $C$.

The other input parameters for the the model from Sec. 2.4 are $C = 21$, $\kappa/2\pi = 2.3\,\mathrm{MHz}$, $\kappa_H/2\pi = 40\,\mathrm{kHz}$, and $\Delta_c = \Delta_s = \Delta_{\mathrm{co}} = 0$. Combining this with $T_c + t_{\mathrm{dark}} = 2.0\,\mu\mathrm{s}$, Eq. (2.54) predicts $\eta_{sr,\mathrm{ad}} = 66.1\%$. From the numerical solution of Eqs. (2.45)–(2.48) $\eta_{sr} = 64.7\%$ we conclude that the adiabatic approximation works well in this parameter regime.

As explained in Sec. 2.7, the target coupling Rabi frequency should be as large as possible. Hence, we use a rectangular target coupling pulse with a power of 70 mW, which is limited by our laser system. The duration of this pulse is chosen long enough to ensure good overlap with the delayed component of the target signal pulse, see Eq. (2.44).

## 5.2 Cavity Rydberg EIT

We record two cavity Rydberg EIT spectra, one with each coupling light field. Similar to Sec. 4.7, we determine the amplitude and phase of the signal light reflected from the cavity when varying the signal detuning over a range of 80 MHz. To obtain phase information, $D$ polarized signal light is sent into the target signal beam path, see Figs. 2.3 and 3.13, and the polarization at the output is measured. Signal light transmitted through the bypass serves as a phase reference. This requires sufficient temporal overlap between the cavity component and the bypass component. Had we used the control signal beam path, there would have been very little temporal overlap between the two components due to the 2 µs

delay caused by the long fiber. For that reason, the target beam path is used to record both EIT spectra.[2]

In the present Sec. 5.2, we deviate from the pulse sequence described in Sec. 5.1. For the control coupling data, the signal light pulses have a rectangular shape with 1 µs length and contain 0.7 photons on average, while the target data is recorded with 1 µs long signal pulses that are shaped according to Eq. (2.79) and contain 0.19 photons on average. The fact that the signal pulse shapes are different for the control and target coupling data is not expected to impact the measurement results in a relevant way. Rectangular Rydberg coupling pulses with a duration of 1.5 µs are superimposed with the signal light pulses.

The resulting cavity Rydberg EIT spectra are shown in Fig. 5.2.[3] We model the data using Eqs. (4.12) and (2.32) with

$$C_{\text{eff}} = C\frac{\Gamma_e}{\Gamma_e - 2i(\Delta_c - \Delta_{ac}) + \frac{|\Omega_{\text{co}}|^2}{\gamma_{\text{rg}} - 2i(\Delta_{\text{co}} + \Delta_c - \Delta_{ac})}} \tag{5.1}$$

according to Eqs. (2.31), (2.33), and (2.35). A simultaneous fit to the power and phase data for each Rydberg state yields $\Omega_{\text{co}}/2\pi = 20.6(4)\,\text{MHz}$ ($\Omega_{\text{co}}/2\pi = 43.0(4)\,\text{MHz}$), $1/\gamma_{rg} = 0.6(2)\,\mu\text{s}$ ($1/\gamma_{rg} = 0.21(5)\,\mu\text{s}$), $C = 23.6(6)$ ($C = 21.1(9)$), and $\phi_0 = 0.748(3)\pi$ ($\phi_0 = 0.917(2)\pi$) for the data with control (target) coupling light. The remaining parameters of the fit model are fixed to the same values as in Sec. 4.7.

The control (target) coupling light power was $P_{\text{co}} = 30\,\text{mW}$ ($P_{\text{co}} = 70\,\text{mW}$) in this measurement. We estimate the control (target) coupling beam waists at the atomic position using the matrix element $d_{er}$ for the transition $|e\rangle \leftrightarrow |r'\rangle$ ($|e\rangle \leftrightarrow |r\rangle$). The angular part of this matrix element is $1/\sqrt{3}$ [8] and the radial part is obtained from $R^{nS}_{5P} = 0.014 \times (50/n)^{3/2} a_0$ [128]. We find $d_{er} = 7.3 \times 10^{-32}\,\text{C m}$ ($d_{er} = 6.9 \times 10^{-32}\,\text{C m}$) for the Rydberg state addressed by the control (target) coupling light. Assuming that the atoms are positioned at the intensity maximum $c\epsilon_0 |E_{\text{co}}|^2/2 = 2P_{\text{co}}/\pi w_{\text{co}}^2$ of a Gaussian beam with waist $w_{\text{co}}$ and electric field amplitude $|E_{\text{co}}| = \hbar |\Omega_{\text{co}}|/d_{er}$, we obtain $w_{\text{co}} = 20\,\mu\text{m}$ ($w_{\text{co}} = 14\,\mu\text{m}$).

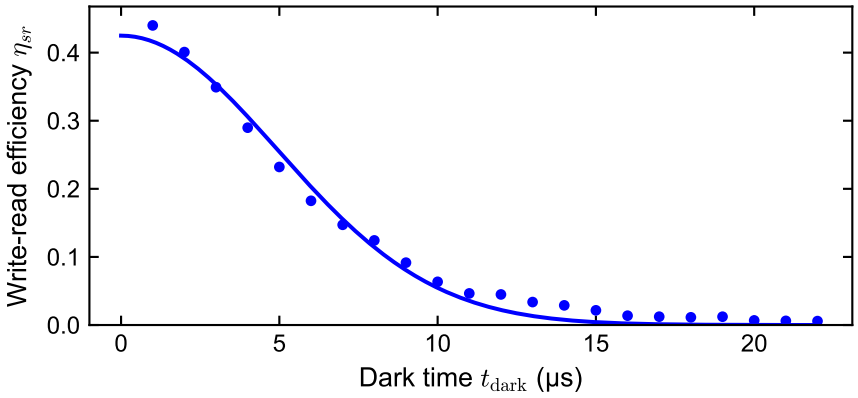


**Figure 5.3:** Decay of the write-read efficiency $\eta_{sr}$ during the dark time between storage and retrieval. A Gaussian fit according to $\eta_{sr}(t_{\mathrm{dark}}) = \eta_{sr}(0)\exp(-t_{\mathrm{dark}}^2/\tau^2)$ yields $\eta_{sr}(0) = 42(1)\%$ and the $1/e$ decay time $\tau = 7.0(2)\,\mu\mathrm{s}$.

## 5.3 Decay of Coherence during the Dark Time between Storage and Retrieval

The fit to the data in Fig. 5.2 yielded a value for the coherence time $1/\gamma_{rg} = 0.6(2)\,\mu\mathrm{s}$ between $|g\rangle$ and $|r'\rangle$. According to Eq. (2.53), an alternative method for obtaining $\gamma_{rg}$ is to consider storage and retrieval using the state $|r'\rangle$, vary the dark time $t_{\mathrm{dark}}$, and measure the corresponding decay of the write-read efficiency $\eta_{sr}$ . Such a measurement is shown in Fig. 5.3. An approximately Gaussian decay with a $1/e$ time of $7.0(2)\,\mu\mathrm{s}$ is observed.

This is considerably longer than the value obtained from the data in Fig. 5.2. An important difference between the two measurements is that the EIT coupling light is turned on at its full power of 30 mW when recording the EIT spectrum, potentially inducing additional dephasing [133]. Such a contribution to the dephasing rate is expected to decrease as a function of the laser power. For zero coupling power we find the value $1/\gamma_{rg} = 7\,\mu\mathrm{s}$ by measuring the dark-time decay shown in Fig. 5.3.

The measured decay time is considerably shorter than the thermal coherence time $\tau_R = 31\,\mu\mathrm{s}$ predicted by Eq. (3.1). However, the atoms are not truly in the dark during

[2]It would be possible to use the control signal beam path instead. To this end, one could send a second signal input pulse onto the gate 2 µs prior to the usual signal-and-control pulse. In this scenario, the bypass light of the first input pulse would have good temporal overlap with the cavity-path light of the second input pulse. Hence, one would obtain phase information. Note that, in essence, this scenario represents a delay line interferometer, which makes the visibility quite sensitive to phase noise of the laser generating the signal light.

[3]To measure these data, we linearly ramp the signal detuning from −40 MHz to 40 MHz while holding one prepared atomic ensemble in the trap for 1 s. There is some asymmetry in the spectra in Fig. 5.2 (c) and (d). This is likely due to the high average input photon number of 0.7 per pulse, which resulted in evaporative loss of atoms caused by scattering of photons during the frequency ramp. For the quantum gate experiments, we choose much lower input photon number. Moreover, the gate performance depends only weakly on the cooperativity. Hence, a moderate atom loss is not a major concern.

the time $t_{\mathrm{dark}}$ because the crossed-beam ODT is always on continuously and induces a position dependent differential light shift between the ground and Rydberg state which contributes to the dephasing rate. A minor extension to the model of Ref. [133] predicts a value for $\gamma_{rg}$ that is fairly close to our measurement.

For the quantum gate experiment, a relatively short dark time of $T_t = 1\,\mu\mathrm{s}$ is used in order to limit loss inside the control bypass delay fiber, see Sec. 2.7. As $1/\gamma_{rg}$ during the dark time is considerably longer than $T_t$, the gate efficiency would not profit much from an increased coherence time at this point. In the future, the efficiency may be improved by replacing the long delay fiber with a high-efficiency quantum memory, as discussed at the end of Sec. 2.7. After such an upgrade, $\gamma_{rg}$ is expected to become an important limiting factor for the efficiency of the gate.

The coherence time can be increased, for instance, by turning off the dipole trap during the dark time. In this situation, a $1/e$ time of $36(2)\,\mu\mathrm{s}$ has been observed in our apparatus.[4] This reproduces an important result from Ref. [133]. This is a nontrivial observation because the surfaces near the atomic ensemble in the new apparatus are made of titanium, whereas in the old vacuum chamber, used in Ref. [133], they were made of glass. As observed in Ref. [69], such surface effects can drastically impact the Rydberg coherence time.

## 5.4 Output Pulses

Here, we characterize the outgoing control and target signal pulses in the absence of Rydberg blockade. This is interesting for identifying imperfections that are independent of the photon-photon interaction. Rydberg blockade is avoided for the data presented here even though the full pulse sequence shown in Fig. 5.1 is used. To understand this, it is instructive to clarify two points. The first point is that we do not postselect data upon detection of one control and one target photon here, in contrast to the analysis in Secs. 5.5–6.6. As we use coherent input pulses containing much less than one photon on average, the probability that the control or the target pulse contains zero photons is much higher than the probability of having one photon in each pulse. The second point is that the input polarization states are chosen such that one photon is always in its bypass. Instead of sending this photon into its bypass, one could just as well omit the corresponding signal light pulse. However, data with both photons present are also useful for quantum process tomography in Sec. 6.4.[5]

[4] In this measurement, many parameters were different than in the rest of this chapter, such as the atomic density, temperature, trapping geometry, etc. Moreover, the Rydberg state $|r'\rangle = |67^2S_{1/2}\rangle$ was used for storage. Due to the larger principal quantum number, the retrieval efficiency oscillates around a Gaussian decay as a function of time in this measurement. The $1/e$ time of this Gaussian decay was $36(2)\,\mu\mathrm{s}$. The observed oscillations are well known and originate from molecular states bound by the interaction between the Rydberg electron and surrounding ground-state atoms [8, 98, 132]. Such oscillations are absent in Fig. 5.3 due to the lower principal quantum number.

[5] Fig. 5.4 is generated from a subset of the same raw data that are also used to generate Figs. 6.1 and 6.4. Fig. 5.4 (a) contains data for the input polarization settings $|DH\rangle$, $|AH\rangle$, and $|RH\rangle$; (b) for $|RH\rangle$; (c) for $|VD\rangle$, $|VA\rangle$, and $|VR\rangle$; and (d) for $|VR\rangle$.

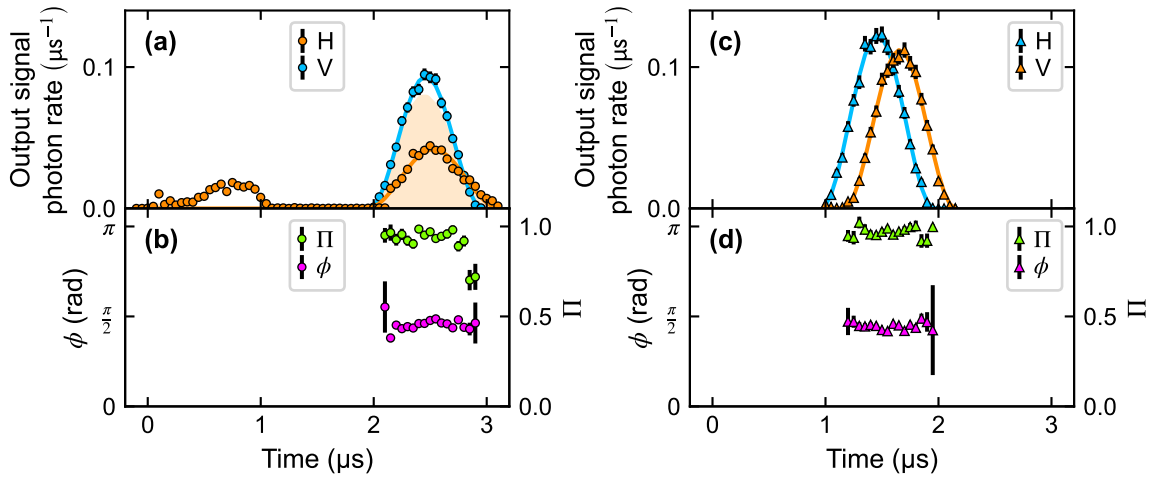


**Figure 5.4:** Characterization of the outgoing (a,b) control and (c,d) target signal pulses. The incoming control (target) photon is in a 50:50 superposition of $H$ and $V$ for the data in the panels on the left (right) hand side. (a) and (c) contain the outgoing signal photon rates for different polarization components. (b) and (d) show the degree of polarization $\Pi$ and the phase $\phi$, exemplarily for $R$ polarized input. The solid lines are fits of $|u_s(t)|^2$ from Eq. (2.79) to the data. The shaded area in (a) is a theory prediction assuming $1/\gamma_{rg} = 7\,\mu s$. Detailed explanations are provided in the main text.

### 5.4.1 Storage and Retrieval

First, we analyze the outgoing control signal pulse. The input control signal light is in a 50:50 superposition of $H$ and $V$ polarization. The input target signal light is $H$ polarized and bypasses the cavity. Fig. 5.4 (a) shows the $H$ and $V$ components of the outgoing control signal light. Orange (blue) data points correspond to light that was routed through the cavity path (bypass).

As expected, the bypass component $V$ is delayed by 2 µs due to the optical fiber. The theoretical prediction for the cavity component from Eqs. (2.45)–(2.48) is marked by the orange shaded area. The discrepancy between this prediction and the measured data is presently not well understood. We extract a write-read efficiency of $\eta_{sr} = 39(1)\%$ which is quite a bit lower than the theoretical expectation of about 65% from Sec. 5.1. We observe that there is significantly more leakage during the storage interval between 0 µs and 1 µs than the model predicts, which suggests that part of the excess loss occurs already during storage. The observed deviation of the model from our data may be a result of the assumption $1/\gamma_{rg} = 7\,\mu s$, which was measured at $\Omega_{co} = 0$.

To obtain complete information about the control output polarization state, we additionally measure the degree of polarization

$$\Pi = \sqrt{S_{HV}^2 + S_{DA}^2 + S_{RL}^2}, \tag{5.2}$$

where $S_{HV}$, $S_{DA}$, and $S_{RL}$ are the normalized Stokes parameters [12, 57], and the phase $\phi$, defined by Eq. (4.14). In this measurement, we use $R$ polarized input control signal

light. As shown in Fig. 5.4 (b), the degree of polarization is high for the times at which there is appreciable overlap between the two components in (a). A weighted average of the plotted data points yields $\Pi = 0.942(7)$ and $\phi = 0.455(4)\pi$. The ideal output state $R$ would correspond to $\phi = \pi/2$. As discussed in Sec. 2.4.2 of Ref. [149], a nonzero coupling detuning $\Delta_{\mathrm{co}}$ leads to a phase shift $t_{\mathrm{dark}}\Delta_{\mathrm{co}}$ on the retrieved photonic output state. We used this effect to fine tune the control coupling laser frequency, aiming at $\Delta_{\mathrm{co}} = 0$.

### 5.4.2 Cavity Rydberg EIT

Next, we analyze the outgoing target signal pulse. Again, the target input pulse is in a 50:50 superposition of $H$ and $V$ polarization. The control signal light is $V$ polarized and bypasses the cavity. The outgoing $H$ and $V$ components of the target signal light are shown in Fig. 5.4 (c). Again, orange (blue) data points correspond to light that was routed through the cavity path (bypass).

The amplitude of the outgoing cavity component is reduced due to losses in optical components and due to an on-resonance cavity EIT reflectivity of $|\mathcal{R}|^2 = 90(1)\%$. Moreover, a pulse delay $t_d = 0.20(1)\,\mu\mathrm{s}$ of the $V$ component relative to the bypass component $H$ is visible in the data.[6] The agreement with the expectation $t_d = 0.18\,\mu\mathrm{s}$ from Eq. (2.44) is good. For the times at which there is appreciable overlap between the two components, the data in Fig. 5.4 (d) show the degree of polarization and the phase $\phi$ of the output for $R$ polarized input. A weighted average of the plotted data points yields $\Pi = 0.974(5)$ and $\phi = 0.442(4)\pi$, both of which are close to the ideal values. We note that obtaining the ideal output phase $\pi/2$ requires tuning the setpoint of the bypass path length stabilization such that an offset phase of $\phi_0 = \pi$ is obtained, see Eq. (4.14). Moreover, we note that the delay between the $H$ and $V$ components of the target output pulse is expected to vanish in the presence of a stored control excitation, see Sec. 2.5.

## 5.5 Cavity Rydberg Blockade

### 5.5.1 Conditional $\pi$ Phase Shift

We now consider cavity Rydberg blockade. Reflecting one target photon while a control excitation is stored inside the cavity is expected to induce a $\pi$ phase shift on the $|HV\rangle$ component of the two-photon output state. To verify this, we prepare the input state $|RV\rangle$ and measure the phase of the control output photons, postselecting upon the detection of a single target photon in state $|V\rangle$. We find $\phi = -0.42(4)\pi$.[7] This value is consistent with a conditional $\pi$ phase shift, for which we would expect $\phi = -\pi/2$.

[6] Note that this delay does not set a fundamental limit to the gate fidelity. When using a long-lived quantum memory instead of the delay fiber, one would obtain better gate performance for longer pulses, which would make the fractional delay much smaller and less of an issue for the fidelity. Presently, the gate fidelity is dominantly limited by other effects.

[7] If we perform an analogous measurement on the target photon by preparing $|HR\rangle$ and postselecting upon detection of a single control photon in state $|H\rangle$, we find $\phi = -0.52(3)\pi$.

### 5.5.2 Conditional Loss

Apart from inducing a conditional $\pi$ phase shift, reflecting one target photon during the dark time increases the loss probability of the two photons. For a perfect superatom geometry, we would expect that this increase is solely due to a reduction of the target cavity reflectivity from $|\mathcal{R}|^2 = 90\%$ to $|\mathcal{R}_b|^2 = 83\%$, which is predicted by Eq. (2.80) for our measured cooperativity of $C = 21$. Together with the measured $\eta_{sr} = 39\%$ we would expect a two-photon survival probability of 32%. However, we measure a significantly lower value of 17(2)%.

This discrepancy may be a consequence of an imperfect superatom geometry. As discussed in Sec. 2.5.3, $\eta_{sr}$ is reduced to $\eta_{sr,t}$ in this situation, see Eq. (2.65). In addition, also $|\mathcal{R}_b|^2$ is reduced because the distance between the stored Rydberg excitation and some atoms is larger than the blockade radius, such that Eq. (2.80) does not hold anymore. However, measuring $\eta_{sr,t}$ and $|\mathcal{R}_b|^2$ separately is nontrivial. As $\eta_{sr,t}$ is by definition postselected upon successful reflection of a target photon, see Sec. 2.5.3, one would need to infer it from a coincidence rate. To this end, one would need to obtain $|\mathcal{R}_b|^2$ from an independent measurement. However, when aiming at measuring $|\mathcal{R}_b|^2$, we do not use a single-photon source for the control photon and suffer from an imperfect storage efficiency. Postselecting data upon detection of a retrieved control photon would not solve this problem because then we would measure the same coincidence rate as above. Hence, the contributions of $\eta_{sr,t}$ and $|\mathcal{R}_b|^2$ to the observed conditional loss are presently unknown.

We stress that conditional loss does not set a fundamental limit to the gate efficiency. To understand this, we once more assume a perfect superatom geometry, which implies that $\eta_{sr,t} = \eta_{sr}$ and that $\mathcal{R}_b$ is given by Eqs. (2.80) and (2.81). In this situation, $|\mathcal{R}_b|$ can become arbitrarily close to unity by choosing large enough $C$. As discussed at the end of Sec. 2.7, a high-efficiency gate is possible at large $C$ if a long coherence time $1/\gamma_{rg}$ can be achieved.

### 5.5.3 Blockade Radius

To obtain an estimate for the blockade radius in our experiment using Eq. (2.55), we require a value for $\gamma_F$. In practice, determining $\gamma_F$ is not easy. We temporarily assume that $\gamma_{rg}$ and $\gamma_F$ are both dominated by electric field noise. Hence, one naively expects $\gamma_F = |\frac{\alpha_{\gamma'} - \alpha_{r'}}{\alpha_r}|\gamma_{rg}$, where the static electric polarizabilities are $(\alpha_{r'},\alpha_r,\alpha_{\gamma'}) = (0.15,0.20,1.9) \times 10^{12}$ a.u. for the states $(|r'\rangle,|r\rangle,|\gamma'\rangle)$, see Sec. 2.2.2. Here, one atomic unit is $1.649 \times 10^{-41}$ J(m/V)$^2$ and we neglected the static ground state polarizability of 319 a.u. Using $\gamma_{rg}$ from the fit to the data in Fig. 5.2, we obtain $1/\gamma_F = 25(6)$ ns and $R_b = 7$ $\mu$m. Really, $\gamma_{rg}$ is not dominated by electric field noise because repeating the measurement of Fig. 5.2 at approximately zero electric field, so that the sensitivity to electric field fluctuations is much reduced, yields no big improvement regarding $\gamma_{rg}$. However, the value of $\gamma_F$ extracted from the above estimate is so large that it seems unlikely that other mechanisms produce a larger value of $\gamma_F$. Hence, we believe that $1/\gamma_F = 25(6)$ ns and $R_b = 7$ $\mu$m are worst-case estimates.

The measured two-photon survival probability, see Sec. 5.5.2, suggests that a perfect superatom geometry is not a terribly good assumption. Indeed, the RMS ensemble radii

$(\sigma_x, \sigma_y, \sigma_z) = (3.3, 4.5, 1.7)$ µm found in Sec. 4.3.2 are smaller but not much smaller than our estimate for the Blockade radius $R_b = 7$ $\mu$m.

# Chapter 6

# Quantum-Logic Gate between Optical Photons

This chapter presents the central results of this thesis, namely experimental results on an optical CNOT gate with an average efficiency above 40%. Some contents of this chapter have been published in Ref. [143]. Sec. 6.1 presents truth tables, which contain classical probabilities of obtaining different output states for a certain input state. Subsequently, we study the non-classical phenomenon of entanglement generation in Sec. 6.2. Sec. 6.3 shows how an electrically tuned Förster resonance is used to maximize the gate fidelity. A complete characterization of the gate operation is provided in Sec. 6.4 using quantum process tomography. As the high gate efficiency is an outstanding feature of this implementation, an extensive discussion of this topic is presented in Sec. 6.5. Finally, an extension of the scheme to a CNOT gate with multiple target qubits leads to the production of Greenberger-Horne-Zeilinger (GHZ) states of up to 5 photons in Sec. 6.6.

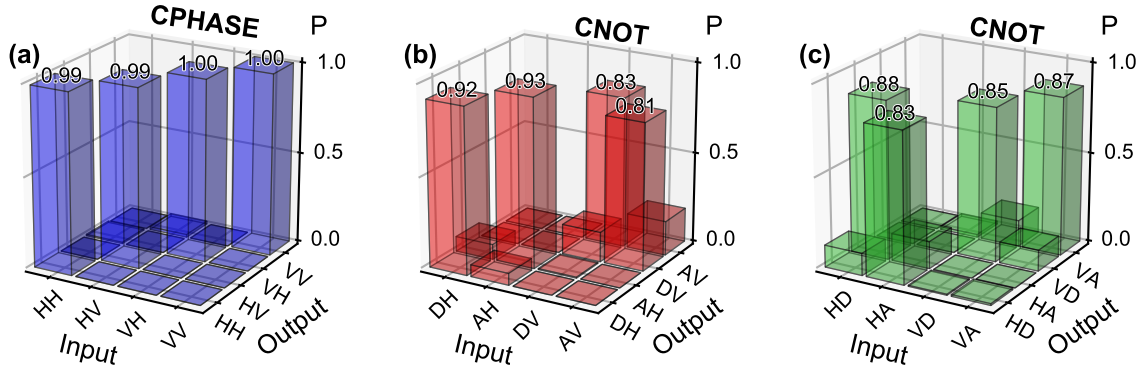


**Figure 6.1:** Truth tables. (a) Postselected truth table in the controlled phase (CPHASE) basis. The average fidelity is 99.4(4)%. (b) Postselected truth table in a CNOT basis. The average fidelity is 87(1)%. (c) Postselected truth table in an alternative CNOT basis. The average fidelity is 86(2)%.

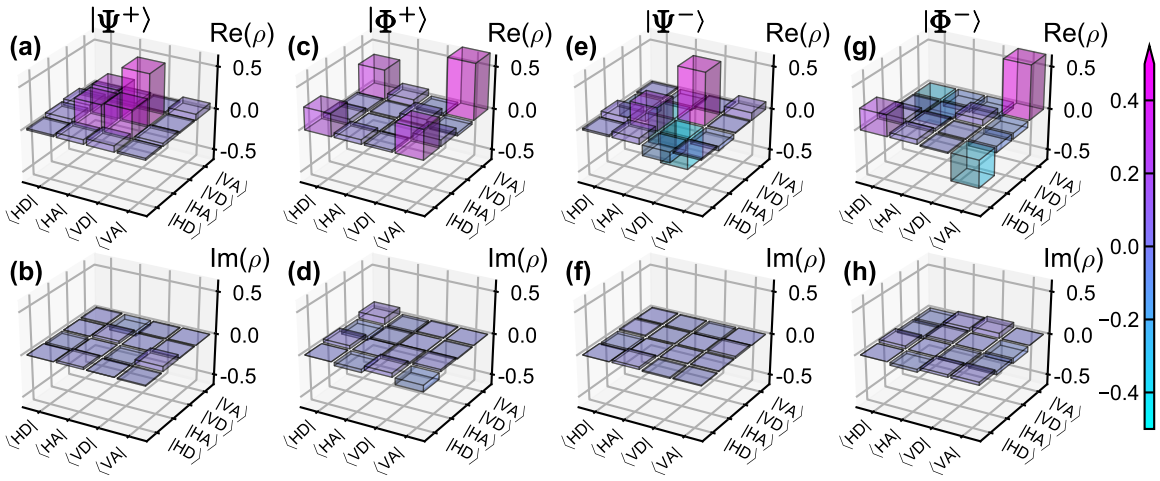


**Figure 6.2:** Bell state tomography. (a,c,e,g) Real and (b,d,f,h) imaginary parts of the reconstructed postselected output density matrices for the input states (a,b) $|DD\rangle$, (c,d) $|DA\rangle$, (e,f) $|AD\rangle$, and (g,h) $|AA\rangle$. Ideally the output states would be the four orthogonal Bell states $|\Psi^+\rangle$, $|\Phi^+\rangle$, $|\Psi^-\rangle$, and $|\Phi^-\rangle$ of Eq. (6.1).

## 6.1 Truth Tables

Fig. 6.1 shows postselected truth tables measured in three different bases. To measure these data, one of the indicated states is used as an input, and the measured probabilities of obtaining the indicated output states in a measurement are displayed. The average fidelity of each truth table is the arithmetic mean of the four labeled probabilities. For the data presented here and in the following sections, we discard the leakage counts during the storage interval between 0 µs and 1 µs in Fig. 5.4. Apart from this, we always include the full temporal output pulse shapes in our data analysis.

The postselected CPHASE truth table in Fig. 6.1 (a) is interesting because it is very close to ideal, thus excluding a variety of otherwise possible sources of experimental imperfections. This insight will be useful below. This is expected from the setup because photons do not jump from one rail to the other. Hence, deviations from a perfect CPHASE truth table come mostly from imperfections in PBSs and waveplates. The CNOT truth tables show the conditional $\pi$ phase shift associated with cavity Rydberg blockade. For the input states in Fig. 6.1 (b), the phase shift manifests itself as a conditional flip $|D\rangle \leftrightarrow |A\rangle$ of the *control* polarization if the target photon is in state $|V\rangle$. An analogous flip can be observed on the *target* polarization in (c) if the control photon is in state $|H\rangle$.

## 6.2 Bell-State Generation

Generating an entangled output state from a separable input state is an important capability of a CNOT gate. Fig. 6.2 shows the postselected output density matrices obtained in quantum state tomography [104] for the input states (a,b) $|DD\rangle$, (c,d) $|DA\rangle$, (e,f) $|AD\rangle$, and (g,h) $|AA\rangle$. From these input states, an ideal gate would produce the four

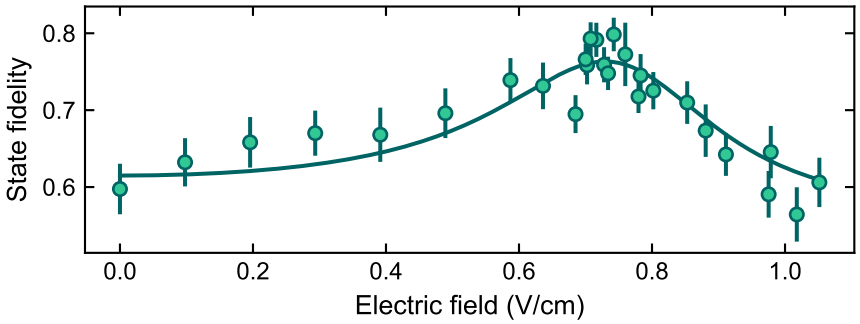


**Figure 6.3:** Electrically tuned Förster resonance. For $|DD\rangle$ input, the state fidelity with the ideal output $(|HA\rangle + |VD\rangle)/\sqrt{2}$ obtained from quantum state tomography is shown for different electric field values. The frequencies of the two coupling lasers were reoptimized for each datapoint to compensate for the changed Stark shifts of the addressed Rydberg states. A maximum of the state fidelity is observed near an electric field of $0.73\,\frac{\mathrm{V}}{\mathrm{cm}}$, which is the expected position of the Förster resonance.

orthogonal Bell states

$$\begin{aligned} |DD\rangle &\mapsto |\Psi^+\rangle = \tfrac{1}{\sqrt{2}}\left(|HA\rangle + |VD\rangle\right) \\ |DA\rangle &\mapsto |\Phi^+\rangle = \tfrac{1}{\sqrt{2}}\left(|HD\rangle + |VA\rangle\right) \\ |AD\rangle &\mapsto |\Psi^-\rangle = \tfrac{1}{\sqrt{2}}\left(|HA\rangle - |VD\rangle\right) \\ |AA\rangle &\mapsto |\Phi^-\rangle = \tfrac{1}{\sqrt{2}}\left(|HD\rangle - |VA\rangle\right). \end{aligned} \tag{6.1}$$

From the data presented in Fig. 6.2, we calculate the corresponding Bell-state fidelity according to Eq. (2.68). For the input states $|DD\rangle$, $|DA\rangle$, $|AD\rangle$, and $|AA\rangle$, we find $F = 79(2)\%$, $F = 82(2)\%$, $F = 81(2)\%$, and $F = 78(3)\%$, respectively. The fact that these fidelities exceed 50% amounts to witnessing two-qubit entanglement.

## 6.3 Electric Field and Förster Resonance

To enhance the Rydberg-Rydberg interaction with the electrically tuned Förster resonance described in Sec. 2.2.2, we apply voltages of $-2.43\,\mathrm{V}$, $-33.4\,\mathrm{V}$, and $-31.1\,\mathrm{V}$ to the two bar electrodes, the pin electrode 1, and the pin electrode 4 in Fig. 3.10. All other electrodes are held at $0\,\mathrm{V}$. According to Eqs. (3.10) and (3.11), this results in an electric field vector of $\boldsymbol{E} = (0.2, 0, 0.7)\frac{\mathrm{V}}{\mathrm{cm}}$, the magnitude of which is $0.73\,\frac{\mathrm{V}}{\mathrm{cm}}$ in accordance with Eq. (2.18). By varying the electrode voltages, we verified that the maximum entangling gate fidelity is indeed obtained at this electric field, as shown in Fig. 6.3.

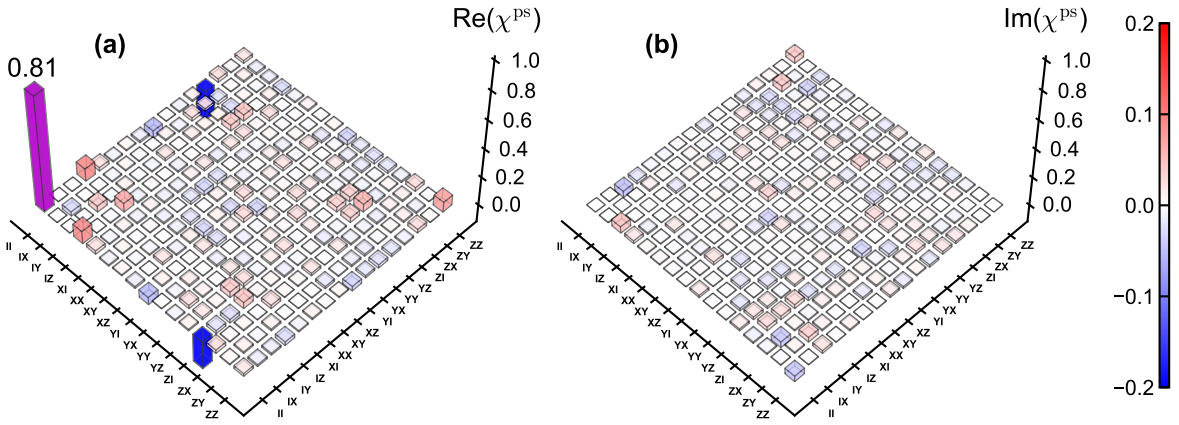


**Figure 6.4:** Quantum process tomography. Real and imaginary parts of the elements of the postselected $16 \times 16$ process matrix $\chi^{\mathrm{ps}}$. The basis for the matrix representation is chosen such that for the ideal gate, one matrix element would equal unity and all others would vanish. The postselected process fidelity is 81(2)%.

## 6.4 Quantum Process Tomography

Instead of characterizing the output state for only a few selected input states, we now fully analyze the performance using quantum process tomography [104, 105, 113, 123]. The latter gives a complete characterization of the quantum process, i.e. it yields a map $\mathcal{E}$ from the $4 \times 4$ density matrix $\rho_{\mathrm{in}}$ at the input to the $4 \times 4$ density matrix $\rho_{\mathrm{out}} = \mathcal{E}(\rho_{\mathrm{in}})$ at the output. The map $\mathcal{E}$ is assumed to be linear. Hence, to characterize $\mathcal{E}$, it suffices to experimentally determine $\rho_{\mathrm{out}}$ using quantum state tomography for a basis of 16 matrices $\rho_{\mathrm{in}}$.

The thus reconstructed map $\mathcal{E}$ can be written in a chi-matrix representation as [104]

$$\mathcal{E}(\rho) = \sum_{i,j=1}^{16} A_i \rho A_j^{\dagger} \chi_{i,j}, \tag{6.2}$$

where the $4 \times 4$ matrices $A_i$ are chosen at will to form a basis $\mathcal{A}$ of operators. The complex expansion coefficients $\chi_{i,j}$ form the $16 \times 16$ process matrix $\chi$ [42]. Of course, the $\chi_{i,j}$ depend on the choice of the basis $\mathcal{A}$. From the experimental data for a basis of 16 matrices $\rho_{\mathrm{in}}$, we calculate a linear, unbiased estimator for $\chi$ by inverting a linear system [104], see also Ref. [143]. Once $\chi$ has been determined, $\rho_{\mathrm{out}} = \mathcal{E}(\rho_{\mathrm{in}})$ can be predicted for an arbitrary $\rho_{\mathrm{in}}$ using Eq. (6.2).

Possible loss of photons is represented by $\mathrm{tr}(\rho_{\mathrm{out}}) \leq 1$, i.e. $\mathcal{E}$ is typically not trace preserving [104]. If the basis $\mathcal{A}$ was orthonormal, i.e. if $\mathrm{tr}(A_i^{\dagger} A_j) = \delta_{i,j}$, then one would obtain $\mathrm{tr}(\chi) = 4\bar{\eta}$ with the average efficiency $\bar{\eta}$ of Eq. (6.4). We normalize the process matrix upon postselection to correct its trace, i.e. we consider the postselected process matrix $\chi^{\mathrm{ps}} = \chi/\bar{\eta}$.

We choose $A_i = UB_i$, where the unitary $4 \times 4$ matrix

$$U = \begin{pmatrix} 1 & 0 & 0 & 0 \\ 0 & -1 & 0 & 0 \\ 0 & 0 & 1 & 0 \\ 0 & 0 & 0 & 1 \end{pmatrix} \tag{6.3}$$

describes the operation of the ideal two-qubit gate in the $(|HH\rangle, |HV\rangle, |VH\rangle, |VV\rangle)$ basis and where the $4 \times 4$ matrices $B_i$ are the 16 tensor products which can be formed from the single-qubit Pauli matrices $I$, $X$, $Y$, and $Z$ in the $(|H\rangle,|V\rangle)$ basis, i.e. $B_1 = I \otimes I$, $B_2 = I \otimes X$, $B_3 = I \otimes Y$, ..., $B_{16} = Z \otimes Z$. The $\frac{1}{2}A_i$ form an orthonormal basis. Hence $\mathrm{tr}(\chi^{\mathrm{ps}}) = 1$. This choice of the $A_i$ is beneficial because for the ideal process matrix, it yields the simple expression $\chi^{\mathrm{id}}_{i,j} = \delta_{1,i}\delta_{1,j}$.

The elements of $\chi^{\mathrm{ps}}$ are shown in Fig. 6.4 with the $B_i$ used as labels. A simple model, which includes only the four measured efficiencies of the CPHASE basis states and two single-qubit visibilities $V_c = 86(4)\%$ and $V_t = 78(3)\%$ for the control and the target qubit agrees fairly well with the measured $\chi^{\mathrm{ps}}$, see Ref. [143].

Now, we turn to the process fidelity. If the basis $\mathcal{A}$ was orthonormal, then the process fidelity would be [42] $F_{\mathrm{pro}} = \frac{1}{16}\mathrm{tr}(\chi^{\mathrm{id}}\chi)$. Hence, $F_{\mathrm{pro}} = \mathrm{tr}(\chi^{\mathrm{id}}\chi)$ for the basis $\mathcal{A}$ chosen here. The postselected version thereof is the postselected process fidelity $F^{\mathrm{ps}}_{\mathrm{pro}} = \mathrm{tr}(\chi^{\mathrm{id}}\chi^{\mathrm{ps}})$. Using that $\mathcal{E}$ is typically a completely positive map [104], one can show that this yields $F^{\mathrm{ps}}_{\mathrm{pro}} \leq 1$. Using $\chi^{\mathrm{id}}_{i,j} = \delta_{1,i}\delta_{1,j}$, one obtains $F^{\mathrm{ps}}_{\mathrm{pro}} = \chi^{\mathrm{ps}}_{1,1}$ [105, 123]. Hence, Fig. 6.4 yields $F^{\mathrm{ps}}_{\mathrm{pro}} = 81(2)\%$. This is clearly above the classical limit of 50%. Multiplying $F^{\mathrm{ps}}_{\mathrm{pro}}$ with the average efficiency $\bar{\eta}$ of Eq. (6.4) yields a process fidelity *without postselection* of $F_{\mathrm{pro}} = 34(1)\%$, which is much better than in all previous measurements of CNOT gates with optical photons, in which $F_{\mathrm{pro}}$ never exceeded 11%.

We note that it is not a coincidence that the postselected Bell state fidelities in the previous section equal the postselected process fidelity within the uncertainties. This is expected because the CPHASE truth table of our gate is to a very good approximation ideal, as shown in Fig. 6.1 (a). For a mathematical proof of this equivalence, see Ref. [143].

## 6.5 Efficiency

The efficiency of the gate is the probability that no photon is lost inside the gate, if one control and one target photon impinge onto the gate. The gate is the part of the setup which is shown in Fig. 2.3. The efficiency also includes optical elements like lenses and waveplates which are not drawn in Fig. 2.3 for simplicity, see Fig. 3.13. The only components which are not included in the efficiency are the light source and the detection setup. This makes sense because neither light sources nor detectors need to be cascaded in a sequence of gates.

The efficiency $\eta$ depends on the input density matrix $\rho_{\mathrm{in}}$ and can be written as $\eta(\rho_{\mathrm{in}}) = \mathrm{tr}[\mathcal{E}(\rho_{\mathrm{in}})]$. For comparing different experiments, one can introduce various figures of merit, which attempt to express the most relevant information about the function $\eta$ in just one number. Obvious choices include the maximum, the minimum, and various averages. We define the average efficiency $\bar{\eta} = \int d\psi \eta(|\psi\rangle\langle\psi|)$, where the integral is over the uniform

(Haar) measure [154] of all normalized input state vectors, similar to the definition of the average fidelity [42]. For any orthonormal basis of state vectors $|v_i\rangle$, the average efficiency can be rewritten as [143]

$$\bar{\eta} = \frac{1}{4}\sum_{i=1}^{4}\eta(|v_i\rangle\langle v_i|). \tag{6.4}$$

Instead of considering only $\bar{\eta}$, one can characterize the full function $\eta$ for all $\rho_{\text{in}}$. As the map from $\rho_{\text{in}}$ to $\eta(\rho_{\text{in}})$ is a linear form, it can be written as $\eta(\rho_{\text{in}}) = \text{tr}(\Theta^\dagger\rho_{\text{in}})$ with a $4\times 4$ matrix $\Theta$, which we call the efficiency matrix. As $\eta(\rho_{\text{in}})$ is real for all Hermitian $\rho_{\text{in}}$, $\Theta$ is Hermitian. For a full characterization of the efficiency function it suffices to measure $\eta(\rho_{\text{in}})$ for a basis of 16 input density matrices $\rho_{\text{in}}$. From this, $\Theta$ can be reconstructed by inverting a linear system. If a process matrix has already been determined, one finds $\Theta = \sum_{i,j=1}^{16} A_j^\dagger A_i \chi_{i,j}$ [143].

In our experiment, the postselected CPHASE truth table in Fig. 6.1 (a) is to a good approximation ideal. Hence, the matrix representation of $\Theta$ in the CPHASE basis is to a good approximation diagonal [143]. To give the full information about $\Theta$, it therefore suffices to quote only these diagonal elements, i.e. the efficiencies obtained if one of the CPHASE basis states is used as an input state. These are measured to be

$$\eta_{HH} = 35.1(7)\%, \quad \eta_{HV} = 15.7(1.4)\%, \quad \eta_{VH} = 61.1(1)\%, \quad \eta_{VV} = 54.9(1.0)\%. \tag{6.5}$$

According to Eq. (6.4), the arithmetic mean of these four efficiencies is the average efficiency $\bar{\eta} = 41.7(5)\%$.

These values are obtained when choosing the experimental parameters to maximize $\bar{\eta}$. If, instead, one was interested in maximizing the minimum eigenvalue $\eta_{\text{min}}$ of $\Theta$, one would have to choose different parameters. We find e.g. $\eta_{\text{min}} = 24.4(2.2)\%$ for a target coupling Rabi frequency of 20 MHz and an atom number of 500, resulting in a collective cooperativity of 40. At these parameters, we obtain

$$\eta_{HH} = 38.2(0.7)\%, \quad \eta_{HV} = 24.4(2.2)\%, \quad \eta_{VH} = 61.1(1)\%, \quad \eta_{VV} = 34.4(0.5)\% \tag{6.6}$$

and $\bar{\eta} = 39.5(6)\%$ along with a Bell-state fidelity of 73(1)% for the output state generated from the input state $|DD\rangle$.

We now discuss how $\eta_{HH}$, $\eta_{HV}$, $\eta_{VH}$, and $\eta_{VV}$ were measured. First, we note that $\eta_{VH}$ refers to a situation in which both photons are in their bypass rails. Hence, this number is independent of the performance of the atom-cavity system and can be expressed as

$$\eta_{VH} = T_{c,V}T_{t,H}, \tag{6.7}$$

where $T_{c,V}$ is the transmission through the control bypass path and $T_{t,H}$ is the transmission through the target bypass path. Using a continuous optical input power of about 1 mW, we measure $T_{c,V} = 0.630(1)$ and $T_{t,H} = 0.970(1)$ with a power meter (Thorlabs, PM160). This yields the above value for $\eta_{VH}$. Along with this, we measure the on-resonance transmission through the control (target) cavity path in the absence of atoms $T_{c,H} = 0.900(1)$ ($T_{t,V} = 0.910(1)$), which will be useful below.

The other three efficiencies $\eta_{HH}$, $\eta_{HV}$, and $\eta_{VV}$ depend on the performance of the atom-cavity system. Therefore, measurements at the single-photon level are required. One

might consider measuring the average number of photons per pulse before the input and after the output of the gate using a single-photon detector. However, this method would be prone to systematic errors in the calibration of the detection efficiency, which typically depends critically on the alignment of the incoming beam with respect to the detector. Hence, we use a method that does not require such a calibration. The basic idea is that if one considers the ratio of two count rates that were measured with the same single-photon detector without changing the alignment, then the detection efficiency cancels. Following this idea, we express the remaining efficiencies as

$$\eta_{HH} = \frac{N_{c,H}}{N_{c,H}^{\mathrm{ref}}} T_{c,H} T_{t,H}, \tag{6.8}$$

$$\eta_{VV} = \frac{N_{t,V}}{N_{t,V}^{\mathrm{ref}}} T_{c,V} T_{t,V}, \tag{6.9}$$

and

$$\eta_{HV} = \frac{C_{HV}}{C_{HV}^{\mathrm{ref}}} T_{c,H} T_{t,V}. \tag{6.10}$$

Here, $N_{c,H}$ ($N_{c,H}^{\mathrm{ref}}$) is the average number of detected control photons in state $|H\rangle$ when running the gate protocol without a target photon in the presence (absence) of a prepared atomic ensemble, excluding (including) counts during the storage time interval. Similarly, $N_{t,V}$ ($N_{t,V}^{\mathrm{ref}}$) is the average number of detected target photons in state $|V\rangle$ when running the gate protocol without a control photon in the presence (absence) of a prepared atomic ensemble. Moreover, $C_{HV}$ ($C_{HV}^{\mathrm{ref}}$) is the average number of detected coincidence events with exactly one control photon in state $|H\rangle$ and exactly one target photon in state $|V\rangle$, when running the gate protocol with both photons at the input and in the presence (absence) of a prepared atomic ensemble. To obtain a smaller statistical uncertainty for the denominator of Eq. (6.10), we use that the counting statistics in the absence of atoms follows a Poissonian distribution[1] and substitute $C_{HV}^{\mathrm{ref}} = N_{c,H}^{\mathrm{ref}} \exp(-N_{c,H}^{\mathrm{ref}}) N_{t,V}^{\mathrm{ref}} \exp(-N_{t,V}^{\mathrm{ref}})$.

Our data acquisition procedure is such that we interleave cycles with and without preparation of an atomic ensemble. To obtain the numbers in Eq. (6.5), we evaluate a part of the data set shown in Figs. 6.2 and 6.4, in which both photons are initially in 50:50 superpositions of $|H\rangle$ and $|V\rangle$ and in which both tomography setups were set to the $H/V$ basis.[2] This has the advantage that the average photon number in the cavity path is only half as large as at the gate input, reducing the probability for unwanted multi-photon events.[3] We measure $N_{c,H} = 0.0182(2)$, $N_{c,H}^{\mathrm{ref}} = 0.0453(8)$, $N_{t,V} = 0.0421(3)$, $N_{t,V}^{\mathrm{ref}} = 0.0439(7)$, and $C_{HV} = 3.5(3) \times 10^{-4}$, which yield Eq. (6.5).

[1] This assumption is justified because our input light pulses are coherent states.

[2] The evaluated input states are $|DD\rangle$, $|DA\rangle$, $|AD\rangle$, $|AA\rangle$, $|RR\rangle$, $|RD\rangle$, and $|DD\rangle$. The astute reader may notice that this implies that the measured $N_{c,H}$ ($N_{t,V}$) contains an unwanted contribution due to an occasionally present target (control) photon inside the cavity path, which results in a systematic underestimation of the efficiency $\eta_{HH}$ ($\eta_{VV}$). However, this effect is small due to the low input photon number.

[3] An evaluation of a different part of the same data set, using only the input state $|HV\rangle$, yields a slightly smaller value of $\eta_{HV}$ because of a higher probability of multi-photon events in the atom-cavity system. As the goal of our experiment is to determine the performance which the gate would have if the input pulses were single-photon Fock states, the value quoted in Eq. (6.5) is much more relevant.

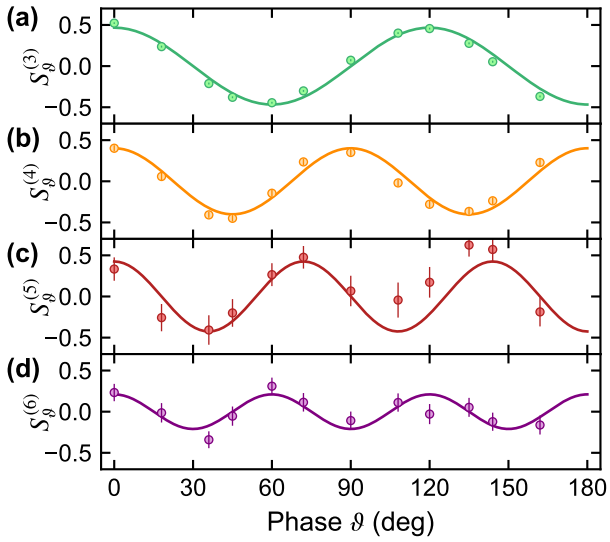


**Figure 6.5:** Multi-photon entanglement. To verify genuine $N$-photon entanglement, we study parity oscillations. To this end, we measure all photons in the same polarization basis ($|b_{\vartheta,+}\rangle$,$|b_{\vartheta,-}\rangle$) with $|b_{\vartheta,\pm}\rangle = (|H\rangle \pm e^{i\vartheta}|V\rangle)/\sqrt{2}$, where $\vartheta$ is real. The measurement outcomes yield the generalized Stokes parameters $S_\vartheta^{(N)} = \langle M_\vartheta^{\otimes N}\rangle$, where $M_\vartheta = |b_{\vartheta,+}\rangle\langle b_{\vartheta,+}| - |b_{\vartheta,-}\rangle\langle b_{\vartheta,-}|$ is the single-qubit operator describing the projection of the Stokes vector along a suitable direction. Dots show measured values of $S_\vartheta^{(N)}$ for $3 \le N \le 6$ as a function of $\vartheta$. The lines are fits according to Eq. (6.12).

Experimentally, two-photon coincidences are detected at an average rate of 560 $s^{-1}$ per incoming photon pair. This number is factors of 520 and $1.3 \times 10^4$ larger than in Refs. [53] and [151], respectively, thus making much more demanding experiments possible in a realistic data acquisition time.

## 6.6 Production of GHZ States

The two-photon gate implemented here is easily extended to a multiple-target CNOT gate [104], thus allowing us to directly produce multi-photon entanglement. This scalability provided by our scheme is advantageous because fewer resources are required compared to cases where several two-qubit gates are cascaded. In particular, an $N$-photon GHZ state $|\Psi_N\rangle = (|H\rangle^{\otimes N} + |V\rangle^{\otimes N})/\sqrt{2}$ can be generated by sending one control photon and $N-1$ target photons onto the gate in an input state with polarization $|D\rangle^{\otimes N}$. We choose to assemble all target photons in one pulse. The target pulse lasts long enough that interactions among target photons are negligible. Hence, each target photon simply acquires a $\pi$ phase shift conditioned on the presence of the same control photon. As a result, the input state $|D\rangle^{\otimes N}$ is mapped onto the output state $(|H\rangle|A\rangle^{\otimes(N-1)} + |V\rangle|D\rangle^{\otimes(N-1)})/\sqrt{2}$. A simple single-qubit unitary applied to all outgoing target photons converts this into the above GHZ state $|\Psi_N\rangle$.

To detect an $N$-photon GHZ state, we again use input pulses with a Poissonian photon

number distribution. But this time, we postselect upon the detection of exactly one control and exactly $N-1$ target photons. The measurements for $N \in \{3,4,5\}$ use $\bar{n}_c = 0.31$ and $\bar{n}_t = 0.41$. As a matter of fact, all $N \leq 5$ data are extracted from the same raw data by postselecting upon different numbers of detected photons. The measurement for $N = 6$ is from a different data set, using $\bar{n}_c = 0.28$ and $\bar{n}_t = 0.88$.

To verify the $N$-photon entanglement, we study parity oscillations [99, 127, 164]. From the experimental data in Fig. 6.5, we calculate the coherence

$$\mathcal{C}_N = \frac{1}{N} \sum_{k=0}^{N-1} (-1)^k S^{(N)}_{k\pi/N} \tag{6.11}$$

and obtain $\mathcal{C}_3 = 47.5(6)\%$, $\mathcal{C}_4 = 39.2(2)\%$, $\mathcal{C}_5 = 37(8)\%$, and $\mathcal{C}_6 = 21(4)\%$. For simplicity, we fit

$$S^{(N)}_{\vartheta} = p \cos(N\vartheta) \tag{6.12}$$

with a free fit parameter $p \in [0,1]$ to the data in Fig. 6.5. This simple curve is expected, e.g. if $\rho_{\text{out}} = p|\Psi_N\rangle\langle\Psi_N| + (1-p)I$, where $I$ is the identity matrix. As an alternative to the direct calculation of $\mathcal{C}_N$ with Eq. (6.11), one can insert the fit curve into this calculation. This yields $\mathcal{C}_N = p$ and makes use of all the available data instead of only the points for $\vartheta = \pi k/N$ with $k \in \{0,1,2,...,N-1\}$. We used this method only for processing the $N = 6$ data.

Our data clearly rule out a completely incoherent mixture for all these values of $N$, because that would imply $\mathcal{C}_N = 0$. In addition, we measure the populations of the states $|H\rangle^{\otimes N}$ and $|V\rangle^{\otimes N}$ and use the results to calculate

$$\mathcal{P}_N = \left\langle (|H\rangle\langle H|)^{\otimes N} + (|V\rangle\langle V|)^{\otimes N} \right\rangle . \tag{6.13}$$

Combining these results, we determine the postselected state fidelity [99, 127, 164]

$$F_N = \langle \Psi_N | \rho_{\text{out}} | \Psi_N \rangle = \frac{1}{2}(\mathcal{P}_N + \mathcal{C}_N) \tag{6.14}$$

and obtain $F_3 = 62.3(4)\%$, $F_4 = 54.6(1.4)\%$, $F_5 = 54.8(5.3)\%$, and $F_6 = 35.9(3.7)\%$. $F_N > 50\%$ implies genuine $N$-photon entanglement [99, 127, 164]. Assuming that the statistical uncertainties quoted here correspond to a Gaussian distribution, the $p$-value, i.e. the probability of $F_N < 50\%$, is $(10^{-207}, 5 \times 10^{-4}, 0.18)$ for $N = (3,4,5)$. A simple model, taking efficiencies and single-qubit visibilities into account agrees well with the experimental data, see Ref. [143].

# Chapter 7

# Conclusion and Outlook

In this work, an optical CNOT gate based on cavity Rydberg EIT was realized and characterized. For the first time, a quantum nonlinear system outperforms the efficiency reached in CNOT gates based on LOQC experiments. However, further improvements to the efficiency are required before practical applications come into reach.

The current performance is limited by the short coherence time of less than 1 µs observed while the EIT coupling light is on. If this issue can be resolved and if the coherence time can be extended to the value of 7 µs observed during the dark time between storage and retrieval, this would be a big step forward. Even longer coherence times around 30 µs are possible if a repulsive dipole trap is used or if the trap is turned off completely during the experiment [133]. The ultimate limit is the Rydberg-state lifetime. With a longer coherence time, a more favorable parameter regime becomes available that allows for much higher gate performance. If one additionally replaces the delay fiber by a storage device with lower loss, such as a high-efficiency quantum memory [62], the theory model developed in Chapter 2 suggests that an efficiency above 90% might be feasible in this situation. Beyond that, the Rydberg-state lifetime may be extended in a cryogenic environment, in which blackbody-induced decay can be suppressed. Moreover, even the small loss induced by the cavity itself may be reduced by employing state-of-the-art cavity mirrors, as discussed in Sec. 3.2.2.

The apparatus developed in this work is not limited to photon-photon gates, but is quite generally useful as an efficient light-matter interface. In the superatom regime, the atomic ensemble can be regarded as a quantum two-level system that can be coherently prepared and manipulated, as demonstrated in Ref. [160]. The coherence time of this two-level system may be extended beyond the Rydberg lifetime by using a Rydberg-dressed atomic ground state, similar to the proposal in Ref. [101]. In this regime, the system may be used as an efficient quantum network node.

Combining our system with a high-brightness single-photon source may enable the production of GHZ states beyond 5 photons. High-fidelity GHZ states can, for instance, be useful for quantum metrology. Similarly, our gate could fuse several one-dimensional cluster states, for instance produced with the scheme of Ref. [147], into a two-dimensional cluster state. Such a state would be a precious resource for measurement based quantum computing.

Finally, other types of nonclassical states of light may be produced with our system. An intriguing option are optical Schrödinger cat states, which have been proposed as resources for optical quantum computing. If cat states with $|\alpha| > 2.5$ can be realized, deterministic

quantum computing using linear optics and photon detection becomes possible [116]. Previous experiments with optical photons stayed well below this threshold [52, 144]. As losses induce decoherence on optical cat states, a high efficiency setup is crucial. Our experimental setup may offer an efficient method for the production of optical cats, using a protocol similar to Ref. [52].

# Appendix A

# Calculation of Interaction Matrix Elements

We want to calculate matrix elements of the dipole-dipole operator. A similar calculation is also shown in Appendix B of Ref. [8]. However, the result deviates from Ref. [163] by a factor of 2. To check which result is correct, the calculation is repeated here with a slightly different approach, which is, in a way, more direct and does not rely on 6-$j$ and 9-$j$ symbols. The results of our calculation agree with Ref. [8].

It is instructive to rewrite Eq. (2.10) in Cartesian coordinates[1]

$$V_{dd} = \frac{e^2}{4\pi\epsilon_0 R^3}(x_1x_2 + y_1y_2 - 2z_1z_2). \tag{A.1}$$

This can be expressed in terms of spherical harmonics $Y_\ell^{m_\ell}(\theta,\phi)$

$$V_{dd} = \frac{e^2}{4\pi\epsilon_0 R^3} r_1 r_2 \left(-\frac{4\pi}{3}\right)(Y_1^1 Y_1^{-1} + Y_1^{-1}Y_1^1 + 2Y_1^0 Y_1^0). \tag{A.2}$$

Here, $Y_1^{m_1}Y_1^{m_2}$ is shorthand for $Y_1^{m_1}(\theta_1,\phi_1)Y_1^{m_2}(\theta_2,\phi_2)$. Matrix elements between atom-pair states are evaluated using the position representation of a single-atom Rydberg state

$$\langle \boldsymbol{x}|\, n,\ell,s,j,m_j\rangle = u_{n,\ell,j}(r)\sum_{m_\ell,m_s} C^{j,m_j}_{\ell,m_\ell,s,m_s} Y_\ell^{m_\ell}(\theta,\phi)|s,m_s\rangle, \tag{A.3}$$

where $u_{n,\ell,j}(r)$ is the radial wave function,[2] the spin part $|s,m_s\rangle$ is kept in representation-free form, and the

$$C^{j,m_j}_{\ell,m_\ell,s,m_s} = \langle\, \ell,m_\ell,s,m_s|\, \ell,s,j,m_j\rangle \tag{A.4}$$

are Clebsch-Gordan coefficients. This results in a separation of the matrix elements into a radial and an angular part

$$\langle \gamma', m'_{j1}, m'_{j2}|V_{dd}|\gamma, m_{j1}, m_{j2}\rangle = -\frac{e^2}{4\pi\epsilon_0 R^3}\cdot R^{n_1,\ell_1,j_1}_{n'_1,\ell'_1,j'_1}\cdot R^{n_2,\ell_2,j_2}_{n'_2,\ell'_2,j'_2}\cdot D\cdot \delta_{s'_1,s_1}\delta_{s'_2,s_2} \tag{A.5}$$

[1] Note that the coordinates for the Rydberg electron of atom 1 and 2 refer to two different coordinate systems, each of which has its origin at the respective atomic core.

[2] The index $j$ represents the fact that there is spin-orbit coupling which leads to $j$ dependent radial wave functions and energies, i.e. fine structure. Calculating $u_{n,\ell,j}(r)$ is possible, for instance, with the method described in Chapter 2.2.2 of Ref. [8].

with the single-atom radial matrix elements

$$R^{n,\ell,j}_{n',\ell',j'} = \int_0^\infty u^*_{n'\ell'j'}(r) r u_{n,\ell,j}(r) r^2 dr \tag{A.6}$$

and the angular part

$$\begin{aligned} D = \sum_{m'_{\ell1},m_{\ell1},m'_{\ell2},m_{\ell2},m_{s1},m_{s2}} & \left(C^{j'_1,m'_{j1}}_{\ell'_1,m'_{\ell1},s'_1,m_{s1}} C^{j'_2,m'_{j2}}_{\ell'_2,m'_{\ell2},s'_2,m_{s2}}\right)^* \\ & \cdot \left(W^{(1)}_1 W^{(2)}_{-1} + W^{(1)}_{-1} W^{(2)}_1 + 2W^{(1)}_0 W^{(2)}_0\right) \cdot C^{j_1,m_{j1}}_{\ell_1,m_{\ell1},s_1,m_{s1}} C^{j_2,m_{j2}}_{\ell_2,m_{\ell2},s_2,m_{s2}}, \end{aligned} \tag{A.7}$$

where the sums over $m'_{s1}$ and $m'_{s2}$ have already been collapsed using

$$\langle s',m'_s|\, s,m_s\rangle = \delta_{s',s}\delta_{m'_s,m_s}, \tag{A.8}$$

the superscript $k$ of $W^{(k)}_q$ denotes the index of the atom, and we abbreviated the single-atom solid-angle integral

$$W_q = \oint d\Omega \sqrt{\frac{4\pi}{3}} \left(Y^{m'_\ell}_{\ell'}\right)^* Y^q_1 Y^{m_\ell}_\ell. \tag{A.9}$$

Specifically for $\ell = m_\ell = 0$, we use that the spherical harmonics are orthonormal and obtain

$$W_q = \frac{1}{\sqrt{3}} \delta_{\ell',1}\delta_{m'_\ell,q}. \tag{A.10}$$

Matrix elements in a coupled basis are obtained from

$$\langle \gamma', J', M'|V_{dd}|\gamma, J, M\rangle = -\frac{e^2}{4\pi\epsilon_0 R^3} \cdot R^{n_1,\ell_1,j_1}_{n'_1,\ell'_1,j'_1} \cdot R^{n_2,\ell_2,j_2}_{n'_2,\ell'_2,j'_2} \cdot \widetilde{D} \cdot \delta_{s'_1,s_1}\delta_{s'_2,s_2} \tag{A.11}$$

with

$$\widetilde{D} = \sum_{m'_{j1},m_{j1},m'_{j2},m_{j2}} \left(C^{J',M'}_{j'_1,m'_{j1},j'_2,m'_{j2}}\right)^* \cdot D \cdot C^{J,M}_{j_1,m_{j1},j_2,m_{j2}}. \tag{A.12}$$

# Appendix B

# Model of Cavity Rydberg Blockade

## B.1 Hamiltonian

We consider Rydberg EIT similar to Sec. 2.3, but with the important difference that there is another atom nearby which is prepared in $|r'\rangle$. Hence, we have a two-atom Hamiltonian that includes atom-light coupling between pair states $|gr'\rangle$, $|er'\rangle$, and $|rr'\rangle$, as well as an atom-atom interaction given by $V_{dd}$ in Eq. (2.10), which couples $|rr'\rangle$ to other atom-pair states.

In our experiment, the atoms have a random spatial distribution. Hence, the internuclear axis for a given atom pair may include some angle $\zeta$ with the wave vector $\boldsymbol{k}_s$ of the EIT signal light. The polarizations of the light fields in our experiment are chosen such that the atom-pair state $|rr'\rangle$ would correspond to the quantum number $M = -1$, if the $z$-axis was chosen along $\boldsymbol{k}_s$.[1] The connection between the state $|rr'\rangle$ and the states $|\gamma,J,M\rangle$ of Sec. 2.2.2 with the $z$-axis chosen along the internuclear axis is made by rotating the coordinate system by the angle $\zeta$. This rotation is expressed by a Wigner $D$-matrix, see e.g. Eq. (2.45) in Ref. [8], yielding

$$|rr'\rangle = \cos^2\frac{\zeta}{2}|\gamma,1,-1\rangle + \frac{\sin\zeta}{\sqrt{2}}|\gamma,1,0\rangle + \sin^2\frac{\zeta}{2}|\gamma,1,1\rangle. \tag{B.1}$$

To obtain a more compact notation, we rewrite Eq. (B.1) as

$$|rr'\rangle = d_c|\gamma,1,c\rangle + d_0|\gamma,1,0\rangle, \quad d_0 = \frac{\sin\zeta}{\sqrt{2}}, \quad d_c = \sqrt{1-|d_0|^2}, \tag{B.2}$$

where we abbreviated the normalized pair state

$$|\gamma,1,c\rangle = c_{-1}|\gamma,1,-1\rangle + c_1|\gamma,1,1\rangle, \quad c_{-1} = \frac{\cos^2\frac{\zeta}{2}}{d_c}, \quad c_1 = \frac{\sin^2\frac{\zeta}{2}}{d_c}. \tag{B.3}$$

Similarly, we introduce the normalized pair state with primed quantum numbers

$$|\gamma',1,c\rangle = c_{-1}|\gamma',1,-1\rangle + c_1|\gamma',1,1\rangle \tag{B.4}$$

[1] We temporarily choose the $z$-axis along $\boldsymbol{k}_s$. We prepare the ensemble in $|5^2S_{1/2},F=2,m_F=-2\rangle$ and use a two-photon transition with $\sigma^-$ polarized signal light and $\sigma^+$ polarized coupling light to address the two Rydberg states via the excited state $|5^2P_{3/2},F'=3,m_{F'}=-3\rangle$. Hence, we can only address the stretched spin states $|n^2S_{1/2},F=2,m_F=-2\rangle$ which are equivalent to $|n^2S_{1/2},m_j=-1/2,m_i=-3/2\rangle$ in fine-structure notation, where $m_i$ is the Zeeman quantum number of the nuclear spin. For an atom pair, $m_{j1}=m_{j2}=-\frac{1}{2}$ implies $M=-1$.

with the same coefficients $c_1$ and $c_{-1}$. We further abbreviate the pair states

$$|r_c\rangle = |\gamma, 1, c\rangle, \qquad |r_0\rangle = |\gamma, 1, 0\rangle, \qquad |f_c\rangle = |\gamma', 1, c\rangle, \qquad |f_0\rangle = |\gamma', 1, 0\rangle \tag{B.5}$$

and obtain

$$|rr'\rangle = d_c|r_c\rangle + d_0|r_0\rangle. \tag{B.6}$$

We now drop the $r'$ from the notation of $|gr'\rangle$, $|er'\rangle$, and $|rr'\rangle$ for brevity. Using the atom-light interaction terms from Ref. [36] and the matrix elements of $V_{dd}$ from Sec. 2.2.2, we obtain the following two-atom Hamiltonian in the electric-dipole approximation

$$\begin{aligned} H =& \hbar\omega_{ge}|e\rangle\langle e| + \hbar\omega_{gr}\left(|r_c\rangle\langle r_c| + |r_0\rangle\langle r_0|\right) + \hbar\omega_{gf}\left(|f_c\rangle\langle f_c| + |f_0\rangle\langle f_0|\right) \\ & - \frac{1}{2}\left[(E_{0,s}e^{-i\omega t} + \text{c.c.})d_{ge}^*|e\rangle\langle g| + (E_{0,\text{co}}e^{-i\omega_{\text{co}}t} + \text{c.c.})d_{er}^*|r\rangle\langle e| + \text{H.c.}\right] \\ & + \frac{\hbar}{2}\left(\Omega_{fc}|f_c\rangle\langle r_c| + \Omega_{f0}|f_0\rangle\langle r_0| + \text{H.c.}\right). \end{aligned} \tag{B.7}$$

The zero of energy is chosen as the energy of state $|g\rangle$. Hence, $\hbar\omega_{ge}$ is the energy of $|e\rangle$, $\hbar\omega_{gr} = E_\gamma$ is the energy of $|r_c\rangle$ and $|r_0\rangle$, and $\hbar\omega_{gf} = E_{\gamma'}$ is the energy of $|f_c\rangle$ and $|f_0\rangle$. $d_{ge}$ ($d_{er}$) is the electric dipole matrix element of the signal (coupling) transition. The atom-atom interaction Rabi frequencies are

$$\Omega_{fc} = -\frac{2C_3}{\hbar R^3}, \qquad \Omega_{f0} = -2\Omega_{fc} = \frac{4C_3}{\hbar R^3}. \tag{B.8}$$

For simplicity, we omitted an additional coupling term caused by the coupling light in Eq. (B.7). We choose this approach because the goal of our calculation is to derive an analytic expression for the blockade radius and we expect that this coupling term has a negligible effect onto the blockade radius.[2]

[2] To see why an additional coupling exists, consider the orthogonal complement $|r_\perp\rangle = d_0|r_c\rangle - d_c|r_0\rangle$ of the state $|rr'\rangle$ in the two-dimensional space spanned by $|r_c\rangle$ and $|r_0\rangle$. Much like the coupling light couples the state $|rr'\rangle$ to the state $|er'\rangle$, it couples the state $|r_\perp\rangle$ to an atom-pair state $|e_\perp\rangle$. The state $|e_\perp\rangle$ is somewhat similar to $|er'\rangle$ but can be entangled and can contain single-atom states which involve Zeeman substates other than those in $|er'\rangle$. In principle, this coupling can become relevant because the state $|r_\perp\rangle$ can become populated by the dipole-dipole interaction if $\zeta \neq 0$. When including this coupling, then the $|5P_{3/2}\rangle$ components of the state $|e_\perp\rangle$ will undergo spontaneous emission into a variety of Zeeman substates of the atomic ground state.

A naive calculation of the steady-state solution of this model would yield a poor spin polarization in the atomic ground state. However, this is unrealistic because in the experiment, the number of atoms in the ensemble is typically much larger than the number of photons in the input signal light pulse. This shows that there is a separation of time scales. The experiment is deliberately kept much shorter than the time scale on which the spin polarization of the atomic ground state is lost. But the experiment lasts long enough that the states involved in EIT and Rydberg blockade come to their stationary state. Hence, we obtain a more realistic model for our experiment by calculating a steady state when replacing the population decay of state $|e_\perp\rangle$ by a dephasing of state $|e_\perp\rangle$. Technically, this is achieved by dropping the corresponding decay of diagonal elements of the density matrix from the model, while keeping the decay of off-diagonal elements.

For the parameters of our experiment, the resulting dephasing of state $|e_\perp\rangle$ has little effect. To illustrate this, we assume that the coherent coupling between states $|r_\perp\rangle$ and $|e_\perp\rangle$ is slower than the dephasing of state $|e_\perp\rangle$. Hence, one can adiabatically eliminate state $|e_\perp\rangle$. Effectively, this means that the coupling to state $|e_\perp\rangle$ disappears from the model and is replaced by an increase in the dephasing rate of state $|r_\perp\rangle$, which in essence corresponds to an increase in the dephasing rates of states $|r_c\rangle$ and $|r_0\rangle$. In Sec. B.4.2, it will turn out that the dephasing rates of states $|r_c\rangle$ and $|r_0\rangle$ have little effect on the blockade physics.

In an interaction picture and using the rotating-wave approximation the Hamiltonian becomes

$$\begin{aligned} H_{\text{int}} =& -\hbar\Delta_s|e\rangle\langle e| - \hbar\Delta_{gr}\left(|r_c\rangle\langle r_c| + |r_0\rangle\langle r_0|\right) - \hbar\Delta_{gf}\left(|f_c\rangle\langle f_c| + |f_0\rangle\langle f_0|\right) \\ &+ \frac{\hbar}{2}\left(\Omega_s|e\rangle\langle g| + \Omega_{\text{co}}|r\rangle\langle e| + \Omega_{fc}|f_c\rangle\langle r_c| + \Omega_{f0}|f_0\rangle\langle r_0| + \text{H.c.}\right) \end{aligned} \tag{B.9}$$

with the two-photon detuning $\Delta_{gr} = \omega + \omega_{\text{co}} - \omega_{gr} = \Delta_s + \Delta_{\text{co}}$ and the sum of the two-photon detuning and the Förster defect $\Delta_{gf} = \omega + \omega_{\text{co}} - \omega_{gf} = \Delta_{gr} + \Delta_F$, where $\Delta_F = \Delta E_F/\hbar$.

## B.2 Dynamic Polarizability

The dynamics of the atomic density matrix $\rho$ in the interaction picture is described by the quantum master equation [36]

$$\partial_t\rho = \frac{1}{i\hbar}[H_{\text{int}}, \rho] + \mathcal{D}(\rho). \tag{B.10}$$

For an operator $a$, we abbreviate

$$\mathcal{L}_a(\rho) = 2a\rho a^\dagger - a^\dagger a\rho - \rho a^\dagger a \tag{B.11}$$

and assume a dissipator

$$\mathcal{D}(\rho) = \frac{\Gamma_e}{2}\mathcal{L}_\sigma(\rho) + \frac{\gamma_{rc}}{2}\mathcal{L}_{P_{rc}}(\rho) + \frac{\gamma_{r0}}{2}\mathcal{L}_{P_{r0}}(\rho) + \frac{\gamma_{fc}}{2}\mathcal{L}_{P_{fc}}(\rho) + \frac{\gamma_{f0}}{2}\mathcal{L}_{P_{f0}}(\rho), \tag{B.12}$$

where

$$\sigma = |g\rangle\langle e|, \qquad P_k = |k\rangle\langle k|, \qquad k \in \{r_c, r_0, f_c, f_0\}. \tag{B.13}$$

$\sigma$ annihilates an excitation on the signal transition. Hence, $\mathcal{L}_\sigma$ represents spontaneous emission. $P_k$ projects onto state $|k\rangle$. Hence, $\mathcal{L}_{P_k}$ represents dephasing. $\gamma_k$ is a dephasing rate.

We now calculate the steady-state solution of this quantum master equation in the limit of weak signal drive

$$\epsilon = \frac{|\Omega_s|}{\Gamma_e} \ll 1. \tag{B.14}$$

To this end, we use the ansatz

$$\rho_{gg} = 1 + O(\epsilon^2), \qquad \rho_{jj} = O(\epsilon^2), \qquad j \in \{e, r_c, r_0, f_c, f_0\} \tag{B.15}$$

for the populations and

$$\rho_{jg} = O(\epsilon), \qquad \rho_{jk} = O(\epsilon^2), \qquad j,k \in \{e, r_c, r_0, f_c, f_0\} \tag{B.16}$$

for the off-diagonal elements. One can show that this ansatz is self-consistent. Neglecting terms of order $\epsilon^2$ we find in the steady state

$$\rho_{eg} = \frac{-i\Omega_s}{\Gamma_e - 2i\Delta_s + \sum\limits_{p\in\{c,0\}} \frac{|\Omega_{\text{co}} d_p|^2}{\gamma_{rp} - 2i\Delta_{gr} + \frac{|\Omega_{fp}|^2}{\gamma_{fp} - 2i\Delta_{gf}}}}. \tag{B.17}$$

In particular, $\rho_{er_0} = \rho_{er_c} = O(\epsilon^2)$ implies that the expectation value of the electric-dipole moment reads $\langle d \rangle = \rho_{eg} d_{ge} e^{-i\omega t} + \text{c.c.} + O(\epsilon^2)$. We rewrite this as $\langle d \rangle = \frac{1}{2} d_0 e^{-i\omega t} + \text{c.c.}$ with amplitude $d_0$. Using the fact that $\rho_{eg}$ is proportional to $E_{0,s}$, we obtain $d_0 = \alpha E_{0,s}$ with the complex dynamic polarizability

$$\alpha = \frac{-2\left|d_{ge}\right|^2}{\hbar \Omega_s} \rho_{eg}. \tag{B.18}$$

## B.3 Atomic Transmission and Cavity Reflection

We now consider an ensemble of atoms. Let the stationary Rydberg excitation $|r'\rangle$ be carried by the $k$th atom. Let $\alpha_{k\ell}$ denote the polarizability of the $\ell$th atom. This means that the $\Omega_{fp}$ depend on the distance between the $k$th and the $\ell$th atom and that the $d_p$ depend on the angle $\zeta_{k\ell}$ between $\boldsymbol{k}_s$ and the internuclear axis connecting the $k$th and the $\ell$th atom. Hence, we now write $\Omega_{k\ell,p}$ and $d_{k\ell,p}$ instead of $\Omega_{fp}$ and $d_p$. Hence, for $\ell \neq k$

$$\alpha_{k\ell} = \alpha_0 \frac{i\Gamma_e}{\Gamma_e - 2i\Delta_s + \sum\limits_{p\in\{c,0\}} \frac{\left|\Omega_{\text{co}} d_{k\ell,p}\right|^2}{\gamma_{rp} - 2i\Delta_{gr} + \frac{\left|\Omega_{k\ell,p}\right|^2}{\gamma_{fp} - 2i\Delta_{gf}}}} \tag{B.19}$$

with $\alpha_0 = 2\left|d_{ge}\right|^2 / \hbar\Gamma_e$. The $k$th atom, which is in the dark state $|r'\rangle$, however, does not interact with the EIT signal light. Hence,

$$\alpha_{kk} = 0. \tag{B.20}$$

We consider an ensemble of atoms with homogeneous density $\varrho$, such that the number of atoms in a given volume $V$ is $N = \varrho V$. The macroscopic polarization $P$ is defined as the dipole moment per volume [36]. Therefore, it has the property $P_k = \frac{1}{2} P_{k,0} e^{-i\omega t} + \text{c.c.}$ with a complex coefficient $P_{k,0}$. Hence, $P_{k,0} = \epsilon_0 \chi_k E_{0,s}$ with the complex dynamical electric susceptibility

$$\chi_k = \frac{\varrho}{\epsilon_0 N} \sum_{\ell=1}^{N} \alpha_{k\ell}. \tag{B.21}$$

The atomic transmission is then

$$t_k = \exp\left( -\frac{d_t}{2N} \sum_{\ell=1}^{N} \frac{\alpha_{k\ell}}{i\alpha_0} \right). \tag{B.22}$$

In analogy to Sec. 2.3, the cavity reflection coefficient is

$$\mathcal{R}_k = -1 + \frac{2\beta}{1 + C_k - i\Delta_c/\kappa} \tag{B.23}$$

where

$$C_k = \frac{C}{N} \sum_{\ell=1}^{N} \frac{\alpha_{k\ell}}{i\alpha_0}. \tag{B.24}$$

This expression holds as long as all the coupling constants $|g_\ell|$ are identical. If not, we generalize the above result to

$$C_k = \frac{1}{\kappa\Gamma_e/2}\sum_{\ell=1}^{N}|g_\ell|^2\,\frac{\alpha_{k\ell}}{i\alpha_0}. \tag{B.25}$$

Inserting Eq. (B.19), we obtain

$$C_k = \frac{1}{\kappa}\sum_{\substack{\ell=1\\\ell\neq k}}^{N}\frac{2\,|g_\ell|^2}{\Gamma_e - 2i\Delta_s + \sum\limits_{p\in\{c,0\}}\frac{\left|\Omega_{\rm co}d_{k\ell,p}\right|^2}{\gamma_{rp}-2i\Delta_{gr}+\frac{\left|\Omega_{k\ell,p}\right|^2}{\gamma_{fp}-2i\Delta_{gf}}}}. \tag{B.26}$$

As a simple crosscheck, we consider $d_0 = 0$ and the van der Waals limit $\gamma_{fp} \ll |\Delta_{gf}|$. We obtain

$$C_k = \frac{1}{\kappa}\sum_{\substack{\ell=1\\\ell\neq k}}^{N}\frac{|g_\ell|^2}{\Gamma_e/2 - i\Delta_s + \frac{|\Omega_{\rm co}|^2}{\gamma_{rc}/2-i(\Delta_{gr}+\Delta_{k\ell})}} \tag{B.27}$$

with $\Delta_{k\ell} = -\left|\Omega_{k\ell,c}\right|^2/4\Delta_{gf}$. Inserting this into our Eq. (B.23) yields an expression for $\mathcal{R}_k$ which is identical to Eq. (2) in Ref. [22]. Using Eq. (B.8), we find

$$\hbar\Delta_{k\ell} \approx -\frac{C_6}{R_{kl}^6}, \qquad C_6 = \frac{|C_3|^2}{\hbar(\Delta_F+\Delta_{gr})}, \tag{B.28}$$

where $R_{k\ell}$ is the distance between the $k$th and the $\ell$th atom. If the Förster defect $\Delta_F$ is much larger than the two-photon detuning $\Delta_{gr}$, then the expression for $C_6$ is consistent with Eq. (2.40) in Ref. [8].

## B.4 Blockade Radius

Based on the atom-pair property $\alpha_{k\ell}$ from Eq. (B.19), we will now derive an expression for the blockade radius. For simplicity, we assume $\gamma_{rc} = 0$ and two-photon resonance $\Delta_{gr} = 0$. In a first attempt, we ignore the anisotropy of the dipole-dipole interaction. Technically, this can be achieved by assuming $d_0 = 0$ or by replacing the right-hand side of Eq. (2.20) by $-C_3/R^3$. We obtain

$$\frac{\alpha_{k\ell}}{\alpha_{\rm 2level}} = \frac{1}{1+\left(\frac{R_{k\ell}}{R_b}\right)^6 e^{i\phi}}, \tag{B.29}$$

where we abbreviated the polarizability in the absence of EIT coupling light $\Omega_{\rm co} = 0$

$$\alpha_{\rm 2level} = \alpha_0\frac{i\Gamma_e}{\Gamma_e - 2i\Delta_s}, \tag{B.30}$$

$\phi = \arg(\gamma_{fc} - 2i\Delta_F) - \arg(\Gamma_e - 2i\Delta_s)$, and $R_b$ given by

$$R_b = \left|\left(\frac{2C_3}{\hbar\Omega_{\rm co}}\right)^2\frac{\Gamma_e - 2i\Delta_s}{\gamma_{fc}-2i\Delta_F}\right|^{1/6} \tag{B.31}$$

which is equivalent to Eq. (2.55) with $\gamma_F = \gamma_{fc}$. The quantity $R_b$ denotes a typical radius in the blockade problem. Hence, we refer to it as the blockade radius.

To relate this to the literature, we consider the van der Waals limit $\gamma_{fc} \ll |\Delta_F|$. We use $C_6$ from Eq. (B.28) and use our above assumption $\gamma_{rg} = 0$ to obtain

$$R_b = \left| \frac{2C_6}{\hbar \Omega_{\mathrm{co}}^2} (\Gamma_e - 2i\Delta_s) \right|^{1/6}. \tag{B.32}$$

This agrees with Ref. [47], which writes $\Omega = \Omega_{\mathrm{co}}/2$. For $|\Delta_s| \ll \Gamma_e$ Eq. (B.32) agrees with Refs. [7, 111] and for $|\Delta_s| \gg \Gamma_e$ Eq. (B.32) agrees with Refs. [33, 151].

### B.4.1 Anisotropy of the Dipole-Dipole Interaction

Next, we show that taking into account the anisotropy of the dipole-dipole interaction has little effect on the blockade physics. We assume $\gamma_{f0} = \gamma_{fc}$ and find

$$\frac{\alpha_{k\ell}}{\alpha_{\mathrm{2level}}} = \frac{1}{1 + e^{i\phi} \frac{R_{k\ell}^6}{R_b^6} (|d_{k\ell,c}|^2 + \frac{1}{4}|d_{k\ell,0}|^2)} \tag{B.33}$$

with $R_b$ from Eq. (B.31). Because of $|d_{k\ell,c}|^2 + |d_{k\ell,0}|^2 = 1$ the sum in the denominator of Eq. (B.33) is a weighted average over two terms. The anisotropy of the interaction is expressed by the fact that the two averaged terms differ by a factor of 4. It is noteworthy that the weighted average is nonzero for all values of the angle $\zeta_{k\ell}$. In other words, the interaction appearing in Eq. (B.33) has no nodal lines.

Calculating $C_k$ involves averaging $\alpha_{k\ell}$ over the index $\ell$ according to Eq. (B.25). The result depends on the index $k$, the geometry of the atomic cloud, and the wave vector of the signal light. Typically, however, the effect of the anisotropy of the interaction on $C_k$ is quite weak. In the one limiting case of the weighted average, $|d_{k\ell,c}|^2 = 1$ for all atom pairs, we recover the previous result, Eq. (B.29); in the other limiting case, $|d_{k\ell,c}|^2 = 0$ for all atom pairs, again, we obtain Eq. (B.29), but now with $R_b$ increased by a factor of $4^{1/6} \approx 1.26$. A more typical scenario is some sort of an average between the two limiting cases. Here, $R_b$ will be larger than in Eq. (B.31) but by a factor even smaller than 1.26. We conclude that the anisotropy has little effect on the blockade physics. Hence, we neglect the anisotropy of the interaction throughout the rest of this work.

### B.4.2 Dephasing of the Rydberg State

In deriving Eq. (B.29), we assumed that the dephasing rate of the Rydberg state $\gamma_{rc}$ vanishes. Now, we take this dephasing rate into account and show that it has little effect on the blockade physics for the parameters of our experiment. Ignoring the anisotropy of the interaction by considering $|d_{k\ell,c}|^2 = 1$, we obtain

$$\frac{\alpha_{k\ell}}{\alpha_{\mathrm{2level}}} = \left( 1 + \frac{e^{-i\alpha}}{G + (R_b/R_{k\ell})^6 e^{-i\beta}} \right)^{-1}, \qquad G = \left| \frac{\gamma_{rc}(\Gamma_e - 2i\Delta_s)}{\Omega_{\mathrm{co}}^2} \right|, \tag{B.34}$$

where we abbreviated $\alpha = \arg(\Gamma_e - 2i\Delta_s)$ and $\beta = \arg(\gamma_{fc} - 2i\Delta_{gf})$. For the parameters of our experiment during the target pulse, we obtain $G \approx 3 \times 10^{-3}$, see Sec. 5.2. Hence, $G$ is nonnegligible only if $R_{k\ell}/R_b \gtrsim G^{-1/6} \approx 2.6$. At such large radius, there is no blockade physics. We conclude that while $\gamma_{rc}$ can have a substantial effect on the EIT transmission and, thus, on the performance of the gate, it has negligible effect on the blockade physics for the parameters of our experiment.

## B.5 Collective Blockade Radius

The above-defined blockade radius is a quantity which depends only on the properties of an atom pair. The optical response of an atomic ensemble, however, additionally depends on the number of atoms $N$. In the following, we incorporate this dependence on $N$ in the definition of an alternative quantity, which we call the collective blockade radius.[3] For simplicity, we assume that all atoms are placed at the same distance $R_{k\ell} = R$ to the excitation $|r'\rangle$, such that $\Omega_{k\ell} = \Omega_f$, and we assume that all atoms are equally coupled to the cavity with $g_\ell = g$. Moreover, we consider $C \gg 1$, a perfectly one sided cavity $\beta = 1$ and resonant light $\Delta_c = \Delta_s = \Delta_{\mathrm{co}} = 0$. As we saw above, the anisotropy of the dipole-dipole interaction leads to only a small effect, which we neglect by setting $d_{k\ell,0} = 0$. Hence we shorten the notation to $\Omega_{k\ell,c} = \Omega_{k\ell}$, $\gamma_{fc} = \gamma_f$, and $\gamma_{rc} = \gamma_r$.

According to Eqs. (B.23), (B.25), (B.30), and (B.29), perfect blockade $R_{k\ell} = 0$ corresponds to $C_k = C$, and $\mathcal{R}_k \approx -1$, which implies $\arg(\mathcal{R}_k) \approx \pi$. Vanishing blockade $R_{k\ell} \to \infty$ corresponds to $C_k \to 0$, and $\mathcal{R}_k \approx +1$, which implies $\arg(\mathcal{R}_k) \approx 0$. Hence, we postulate

$$\mathrm{Re}(\mathcal{R}_k) = 0 \tag{B.35}$$

as a criterion for the collective blockade radius. Note that if $\mathrm{Im}(\mathcal{R}_k) \neq 0$, then this will be equivalent to $\arg(\mathcal{R}_k) = \pi/2$. We assume $|\Omega_{\mathrm{co}}|^2/\gamma_r\Gamma_e \gg C$ because otherwise the photon-photon gate would have poor performance, as discussed in Sec. 2.7. From Eq. (B.35) we find

$$R_{\mathrm{coll}} = \left| \left(\frac{2C_3}{\hbar\Omega_{\mathrm{co}}}\right)^2 \frac{\Gamma_e}{\gamma_f - 2i\Delta_F} C \right|^{1/6}. \tag{B.36}$$

Comparison with $R_b$ from Eq. (2.55) with $\Delta_s = 0$ shows that $R_{\mathrm{coll}} = R_b C^{1/6}$. As $C$ is proportional to the number of atoms, this represents a collective enhancement of $R_b$, which otherwise depends only on $C_3$ and single-atom properties.

[3] While we consider an atomic ensemble in a cavity, one can also apply a similar concept to free-space EIT. In the latter context, Ref. [114] used $R_b = (C_6/\hbar\gamma_T)^{1/6}$, where $\gamma_T$ is the measured linewidth of the EIT transmission feature, which depends on the atom number.

# Appendix C

# Fidelity and Efficiency for Pulsed Light Fields

We derive expressions for the fidelity and efficiency of the $\pi$ phase gate described in Sec. 2.6, considering quantum states of single-photon pulses

$$|\psi\rangle = \int_{-\infty}^{+\infty} d\omega \widetilde{u}(\omega) e^{-i\omega t} a^{\dagger}_{\omega,p} |\varnothing\rangle, \tag{C.1}$$

where $\widetilde{u}(\omega)$ is the pulse envelope in the frequency domain, which is normalized according to Eq. (2.40), and $a^{\dagger}_{\omega,p}$ is a bosonic creation operator for one photon in the considered spatial mode with angular frequency $\omega$ and polarization $p$, which can be $H$ or $V$, for instance. We abbreviate for the control photon

$$|H_{\omega_c}\rangle = e^{-i\omega_c t} a^{\dagger}_{\omega_c,H} |\varnothing\rangle, \qquad |V_{\omega_c}\rangle = e^{-i\omega_c t} a^{\dagger}_{\omega_c,V} |\varnothing\rangle \tag{C.2}$$

and for the target photon

$$|H_{\omega_t}\rangle = e^{-i\omega_t t} a^{\dagger}_{\omega_t,H} |\varnothing\rangle, \qquad |V_{\omega_t}\rangle = e^{-i\omega_t t} a^{\dagger}_{\omega_t,V} |\varnothing\rangle, \tag{C.3}$$

with the creation operators $a^{\dagger}_{\omega_c,H}$ and $a^{\dagger}_{\omega_c,V}$ ($a^{\dagger}_{\omega_t,H}$ and $a^{\dagger}_{\omega_t,V}$ ) for one photon in the spatial mode of the control (target) photon with polarization $H$ and $V$. We generalize the monochromatic input state $|DD\rangle$ of Eq. (2.67) to pulsed target light. Hence, the two-photon input state for an entangling gate operation reads

$$|\Psi_{\text{in}}\rangle = \frac{1}{2} \int_{-\infty}^{+\infty} d\omega_c \widetilde{u}_c(\omega_c) \left(|H_{\omega_c}\rangle + |V_{\omega_c}\rangle\right) \otimes \int_{-\infty}^{+\infty} d\omega_t \widetilde{u}_t(\omega_t) (|H_{\omega_t}\rangle + |V_{\omega_t}\rangle), \tag{C.4}$$

where $\omega_c$ ($\omega_t$) is the angular frequency of the control (target) photon and $\widetilde{u}_c(\omega_c)$ ($\widetilde{u}_t(\omega_t)$) is the pulse envelope of the incoming control (target) photon. Note that this notation is valid because the control and target photon occupy different spatial modes according to Fig. 2.3, such that the Hilbert spaces spanned by $(|H_{\omega_c}\rangle, |V_{\omega_c}\rangle)$ and $(|H_{\omega_t}\rangle, |V_{\omega_t}\rangle)$ are orthogonal. Within each Hilbert space, the state vectors have the property

$$\langle p_{\omega'} | \, q_{\omega} \rangle = e^{-i(\omega-\omega')t} \, \delta_{pq} \, \delta(\omega' - \omega), \qquad p, q \in \{H, V\}, \tag{C.5}$$

which follows from the commutation relation $\left[a_{p,\omega'}, a^\dagger_{q,\omega}\right] = \delta_{pq}\ \delta(\omega' - \omega)$.

Ideally, the output state is

$$|\Psi_{\text{Bell}}\rangle = \int_{-\infty}^{+\infty} d\omega_c \int_{-\infty}^{+\infty} \widetilde{u}_{c,\text{out}}(\omega_c)\widetilde{u}_{t,\text{out}}(\omega_t)|\psi_{\text{Bell},\omega_c,\omega_t}\rangle \tag{C.6}$$

with

$$|\psi_{\text{Bell},\omega_c,\omega_t}\rangle = \frac{1}{2}\left(|H_{\omega_c}H_{\omega_t}\rangle - |H_{\omega_c}V_{\omega_t}\rangle + |V_{\omega_c}H_{\omega_t}\rangle + |V_{\omega_c}V_{\omega_t}\rangle\right) \tag{C.7}$$

where $|H_{\omega_c}H_{\omega_t}\rangle$ is shorthand for $|H_{\omega_c}\rangle \otimes |H_{\omega_t}\rangle$, etc.

The actual time-dependent output state of the $\pi$ phase gate shown in Fig. 2.3 for pulsed target and control light is

$$\begin{aligned}|\Psi_{\text{out}}\rangle =& \sqrt{1-\eta}\ |\Psi_{\text{loss}}\rangle \\ &+ \int_{-\infty}^{+\infty} d\omega_c \int_{-\infty}^{+\infty} d\omega_t \Bigg[\widetilde{u}_{\text{retr}}(\omega_c)c_H \frac{\widetilde{u}_t(\omega_t)t_H|H_{\omega_c}H_{\omega_t}\rangle + \widetilde{u}_b(\omega_t)t_V|H_{\omega_c}V_{\omega_t}\rangle}{2} \\ &\qquad + \widetilde{u}_{\text{delay}}(\omega_c)c_V \frac{\widetilde{u}_t(\omega_t)t_H|V_{\omega_c}H_{\omega_t}\rangle + \widetilde{u}_{\mathcal{R}}(\omega_t)t_V|V_{\omega_c}V_{\omega_t}\rangle}{2}\Bigg],\end{aligned} \tag{C.8}$$

where $|\Psi_{\text{loss}}\rangle$ is the quantum state when at least one photon is lost, $\eta$ is the probability that no photon is lost, $\widetilde{u}_{\text{retr}}(\omega_c)$ ($\widetilde{u}_{\text{delay}}(\omega_c)$) is the envelope of the control pulse retrieved from the cavity (delayed in the optical fiber) normalized according to Eq. (2.40), $\widetilde{u}_{\mathcal{R}}(\omega_t)$ is the envelope of the outgoing target pulse for cavity Rydberg EIT defined in Eq. (2.41), and $\widetilde{u}_b(\omega)$ is the envelope of the outgoing target pulse for cavity Rydberg blockade defined in Eq. (2.63). Note that this state features not only the desired entanglement between the polarization degrees of freedom of the two photons, but also unwanted entanglement between the polarization of the control photon and the pulse envelope of the target photon because $\widetilde{u}_b \neq \widetilde{u}_{\mathcal{R}}$.

As a generalization of Eq. (2.69), we define the fidelity

$$F_{\text{env}} = \left|\langle \Psi_{\text{Bell}}|\ \Psi_{\text{out}}\rangle\right|^2, \tag{C.9}$$

which includes a penalty if the outgoing pulse envelopes do not match the envelopes in Eq. (C.6). Using $\langle \Psi_{\text{Bell}}|\ \Psi_{\text{loss}}\rangle = 0$ and Eq. (C.5), we simplify Eq. (C.9) under the assumptions $c_H = c_V = t_H = t_V = 1$, $\widetilde{u}_{\text{retr}}(\omega_c) = \widetilde{u}_{\text{delay}}(\omega_c) = \widetilde{u}_{c,\text{out}}(\omega_c)$, and $\widetilde{u}_t(\omega_t) = \widetilde{u}_{t,\text{out}}(\omega_t)$. We find

$$F_{\text{env}} = \left|\int_{-\infty}^{+\infty} d\omega\, |\widetilde{u}_t(\omega)|^2\, \frac{2 + \mathcal{R}(\omega) - \sum_k |\alpha_k|^2\, \mathcal{R}_k(\omega)}{4}\right|^2 \tag{C.10}$$

which is identical to the expression for the Choi-Jamiolkowski process fidelity $F_{\text{CJ}}$ for this gate in Ref. [22]. Hence, in this special case, the *state* fidelity $F_{\text{env}}$ between the ideal and actual output states for a properly chosen input state is identical to the *process* fidelity $F_{\text{CJ}}$. This identicalness is not a coincidence. Instead, it results from the fact that the

model here and the model in Ref. [22] assume that the CPHASE truth table is ideal, as discussed in Ref. [143].

In order to measure $F_{\text{env}}$ in an experiment, one would have to overlap the outgoing light pulses with suitable reference light with envelopes according to Eq. (C.6) and then perform appropriate measurements. A problem with $F_{\text{env}}$ is that different applications might require different envelopes $u_{c,\text{out}}$ and $u_{t,\text{out}}$. As long as one does not have a specific application in mind, it is unclear for which envelopes $F_{\text{env}}$ should be measured.

Hence, in our experiment we apply no reference light and we ignore the arrival time of each photon, when measuring the polarization of each photon. Ignoring the arrival time is equivalent to ignoring the frequencies $\omega_c$ and $\omega_t$. Hence, calculating the efficiency from the outcomes of these measurements yields

$$F = \langle \Psi_{\text{out}} | \mathbb{P}_F | \Psi_{\text{out}} \rangle \tag{C.11}$$

with the projector

$$\mathbb{P}_F = \int_{-\infty}^{+\infty} d\omega_c \int_{-\infty}^{+\infty} d\omega_t |\psi_{\text{Bell},\omega_c,\omega_t}\rangle\langle\psi_{\text{Bell},\omega_c,\omega_t}|. \tag{C.12}$$

Using Eq. (C.5) and the unitarity of the Fourier transform (Parseval's theorem), we obtain Eqs. (2.71)–(2.75).

It is worth comparing $F$ and $F_{\text{env}}$. First, we note that using a Cauchy-Schwarz inequality, one can show that

$$F_{\text{env}} \leq F. \tag{C.13}$$

Second, we note that in the limit of monochromatic light fields, the definitions in Eqs. (C.9) and (C.11) become identical. Third, to give a particularly striking example of the difference between $F$ and $F_{\text{env}}$, we consider the special case in which there is an envelope deformation that is identical for all outgoing control envelopes $\widetilde{u}_{\text{retr}}(\omega_c) = \widetilde{u}_{\text{delay}}(\omega_c) = \widetilde{u}_d(\omega_c)$ for all $\omega_c$ and which has the property $\int d\omega_c \widetilde{u}^*_{c,\text{out}}(\omega_c)\widetilde{u}_d(\omega_c) = 0$. This envelope deformation has no effect on $F$ and at the same time yields $F_{\text{env}} = 0$.

To describe postselection of measurement results upon the detection of both photons, we consider the orthogonal projection operator onto the subspace in which no photon was lost

$$\mathbb{P}_\eta = \int_{-\infty}^{+\infty} d\omega_c \int_{-\infty}^{+\infty} d\omega_t \sum_{\substack{p\in\{H,V\}\\ q\in\{H,V\}}} |p_{\omega_c} q_{\omega_t}\rangle\langle p_{\omega_c} q_{\omega_t}|. \tag{C.14}$$

The efficiency of the gate is

$$\eta = \langle \Psi_{\text{out}} | \mathbb{P}_\eta | \Psi_{\text{out}} \rangle. \tag{C.15}$$

Using $\mathbb{P}_\eta |\Psi_{\text{loss}}\rangle = 0$, this yields Eqs. (2.76) and (2.77). For $c_H = c_V = t_H = t_V = 1$, $\eta$ from Eqs. (2.76) and (2.77) becomes identical to $P_{\text{suc}}$ in Ref. [22].

The output state obtained after postselection upon detection of both photons is obviously $\propto \mathbb{P}_\eta |\Psi_{\text{out}}\rangle$. Proper normalization yields

$$|\Psi_{\text{post}}\rangle = \frac{\mathbb{P}_\eta |\Psi_{\text{out}}\rangle}{\sqrt{\eta}}. \tag{C.16}$$

Replacing $|\Psi_{\text{out}}\rangle$ by $|\Psi_{\text{post}}\rangle$ in Eq. (C.11), we define the postselected fidelity

$$F_{\text{post}} = \langle\Psi_{\text{post}}|\mathbb{P}_F|\Psi_{\text{post}}\rangle = \frac{F}{\eta}. \tag{C.17}$$

# Appendix D

# Polarization Convention

We use the polarization of a single photon to encode a quantum bit (qubit) of information [104]. Hence, we define the polarization convention used in this work. Assuming that the propagation direction of the light field is along the positive $z$-axis, we express the normalized polarization vector from Sec. 2.1 as $\boldsymbol{\epsilon} = c_x \boldsymbol{e}_x + c_y \boldsymbol{e}_y$, with the unit vectors along the $x$- and $y$-axis $\boldsymbol{e}_x$ and $\boldsymbol{e}_y$. The complex coefficients $c_x$ and $c_y$ fulfill $|c_x|^2 + |c_y|^2 = 1$. These coefficients are the entries of the normalized Jones vector [12, 57] $\boldsymbol{J} = (c_x, c_y)$. The following normalized Jones vectors are particularly relevant for this work [12, 57]

$$\begin{aligned} \boldsymbol{J}_H &= \begin{pmatrix} 1 \\ 0 \end{pmatrix}, & \boldsymbol{J}_D &= \frac{1}{\sqrt{2}} \begin{pmatrix} 1 \\ 1 \end{pmatrix}, & \boldsymbol{J}_R &= \frac{1}{\sqrt{2}} \begin{pmatrix} 1 \\ -\mathrm{i} \end{pmatrix}, \\ \boldsymbol{J}_V &= \begin{pmatrix} 0 \\ 1 \end{pmatrix}, & \boldsymbol{J}_A &= \frac{1}{\sqrt{2}} \begin{pmatrix} 1 \\ -1 \end{pmatrix}, & \boldsymbol{J}_L &= \frac{1}{\sqrt{2}} \begin{pmatrix} 1 \\ \mathrm{i} \end{pmatrix}. \end{aligned} \tag{D.1}$$

The indices refer to the oscillation pattern of the electric field vector, which can be horizontal ($H$), vertical ($V$), diagonal ($D$), anti-diagonal ($A$), right-handed circular ($R$) or left-handed circular ($L$).

The quantum state of a polarization qubit is

$$|\psi\rangle = c_x |H\rangle + c_y |V\rangle, \tag{D.2}$$

where $|H\rangle$ ($|V\rangle$) is the quantum state of a single photon with horizontal (vertical) polarization. In analogy to Eq. (D.1), we define single-photon quantum states for the remaining four Jones vectors

$$\begin{aligned} |D\rangle &= \frac{1}{\sqrt{2}}(|H\rangle + |V\rangle), & |R\rangle &= \frac{1}{\sqrt{2}}(|H\rangle - i|V\rangle), \\ |A\rangle &= \frac{1}{\sqrt{2}}(|H\rangle - |V\rangle), & |L\rangle &= \frac{1}{\sqrt{2}}(|H\rangle + i|V\rangle). \end{aligned} \tag{D.3}$$

# Appendix E

# Cavity Mode Matching Limit due to Astigmatism

We assume that the cavity eigenmodes are well approximated by Hermite-Gauss modes [38, 141] and express the fundamental transverse cavity mode as $m_{0,0}(\boldsymbol{x}) = m_x(x,z)m_y(y,z)$ with

$$m_\ell(\ell,z) = \frac{A_\ell}{\sqrt{q_\ell(z)}} \exp\left(i\frac{\omega}{c}\frac{\ell^2}{2q_\ell(z)}\right), \qquad \ell \in \{x,y\}, \tag{E.1}$$

where

$$q_\ell(z) = z - q_{0,\ell} \tag{E.2}$$

is the complex beam parameter with $q_{0,\ell} = z_{0,\ell} + iz_{R,\ell}$, $z_{R,\ell} = \pi w_{0,\ell}^2/\lambda$ is the Rayleigh range, $A_\ell$ is a normalization constant, $z_0$ is the position of the beam waist along the $z$-axis, which coincides with the optical axis, and $w_0$ is the beam waist. Eq. (3.2) implies $|A| = (\frac{\omega z_{R,\ell}}{c\pi})^{1/4}$.

We assume that the incoming beam is non-astigmatic, i.e. it is described by the same expression $m_{0,0}(\boldsymbol{x})$ but with $q_{0,x} = q_{0,y} = q_0$, $w_{0,x} = w_{0,y} = w_0$, $z_{R,x} = z_{R_y} = z_R$, and $z_{0,x} = z_{0,y} = z_0$. Evaluating Eqs. (3.4) and (3.5), we obtain

$$\eta_{\text{mode}} = \eta_x\eta_y \tag{E.3}$$

with

$$\eta_\ell = \frac{2\sqrt{z_R z_{R,\ell}}}{\left|q_0 - q_{0,\ell}^*\right|} = \sqrt{\frac{1}{1 + \left|q_0 - q_{0,x}\right|^2/(4z_R z_{R,\ell})}}. \tag{E.4}$$

One can show that $\eta_{\text{mode}}$ reaches a maximum of

$$\eta_{\max} = \frac{2\eta_{xy}}{1+\eta_{xy}} \tag{E.5}$$

for

$$z_{0,\max} = \frac{z_{R,y}z_{0,x} + z_{R,x}z_{0,y}}{z_{R,x} + z_{R,y}}, \qquad z_{R,\max} = \frac{z_{R,x}z_{R,y}}{z_{R,x} + z_{R,y}}\frac{2}{\eta_{xy}}, \tag{E.6}$$

where we abbreviated

$$\eta_{xy} = 2\sqrt{\frac{z_{R,x}z_{R,y}}{\left(z_{0,x} - z_{0,y}\right)^2 + \left(z_{R,x} + z_{R,y}\right)^2}}. \tag{E.7}$$

Inserting the numbers for $q_{0,x}$ and $q_{0,y}$ given in Sec. 3.2.5, we find $\eta_{\text{mode}} = 99.0\%$ ($\eta_{\text{mode}} = 99.1\%$) at $z_{0,\max} = 13.5\,\text{mm}$ and $w_{0,\max} = \sqrt{z_{R,\max}\lambda/\pi} = 31.6\,\mu\text{m}$ ($z_{0,\max} = 2.1\,\text{mm}$ and $w_{0,\max} = 132\,\mu\text{m}$) for the incoming control (target) beam.

# Bibliography


[1] C. S. Adams, J. D. Pritchard, and J. P. Shaffer. Rydberg Atom Quantum Technologies. *Journal of Physics B* **53**, 012002 (2019).

[2] G. S. Agarwal. Vacuum-Field Rabi Splittings in Microwave Absorption by Rydberg Atoms in a Cavity. *Physical Review Letters* **53**, 1732–1734 (1984).

[3] J. Altepeter, E. Jeffrey, and P. Kwiat. Photonic State Tomography. *Advances in Atomic, Molecular and Optical Physics* **52**, 105–159 (2005).

[4] B. Arora and B. K. Sahoo. State-Insensitive Trapping of Rb Atoms: Linearly Versus Circularly Polarized Light. *Physical Review A* **86**, 033416 (2012).

[5] J. B. Balewski. A Single Electron in a Bose-Einstein Condensate. PhD thesis. Universität Stuttgart, 2014.

[6] D. Barredo, S. de Léséleuc, V. Lienhard, T. Lahaye, and A. Browaeys. An Atom-By-Atom Assembler of Defect-Free Arbitrary Two-Dimensional Atomic Arrays. *Science* **354**, 1021–1023 (2016).

[7] S. Baur, D. Tiarks, G. Rempe, and S. Dürr. Single-Photon Switch Based on Rydberg-Blockade. *Physical Review Letters* **112**, 073901 (2014).

[8] S. E. Baur. A Single-Photon Switch and Transistor Based on Rydberg Blockade. PhD thesis. Technische Universität München, 2015.

[9] K. M. Beck, M. Hosseini, Y. Duan, and V. Vuletić. Large Conditional Single-Photon Cross-Phase Modulation. *Proceedings of the National Academy of Sciences* **113**, 9740–9744 (2016).

[10] S. A. Bhatti, C. L. Cromer, and W. E. Cooke. Analysis of the Rydberg Character of the $5d7d\,^1D_2$ State of Barium. *Physical Review A* **24**, 161–165 (1981).

[11] H.-J. Briegel, W. Dür, J. I. Cirac, and P. Zoller. Quantum Repeaters: The Role of Imperfect Local Operations in Quantum Communication. *Physical Review Letters* **81**, 5932–5935 (1998).

[12] C. Brosseau. Fundamentals of Polarized Light, a Statistical Optics Approach. Wiley, New York (1998).

[13] D. E. Browne and T. Rudolph. Resource-Efficient Linear Optical Quantum Computation. *Physical Review Letters* **95**, 010501 (2005).

[14] J. Calsamiglia and N. Lütkenhaus. Maximum Efficiency of a Linear-Optical Bell-State Analyzer. *Applied Physics B* **72**, 67–71 (2001).

[15] S. H. Cantu, A. V. Venkatramani, W. Xu, L. Zhou, B. Jelenković, M. D. Lukin, and V. Vuletić. Repulsive Photons in a Quantum Nonlinear Medium. *Nature Physics* **16**, 921–925 (2020).

[16] W. Chen, K. M. Beck, R. Bücker, M. Gullans, M. D. Lukin, H. Tanji-Suzuki, and V. Vuletić. All-Optical Switch and Transistor Gated by One Stored Photon. *Science* **341**, 768–770 (2013).

[17] J. I. Cirac, P. Zoller, H. J. Kimble, and H. Mabuchi. Quantum State Transfer and Entanglement Distribution among Distant Nodes in a Quantum Network. *Physical Review Letters* **78**, 3221–3224 (1997).

[18] J.-F. Clément, J.-P. Brantut, M. Robert-de-Saint-Vincent, R. A. Nyman, A. Aspect, T. Bourdel, and P. Bouyer. All-Optical Runaway Evaporation to Bose-Einstein Condensation. *Physical Review A* **79**, 061406 (2009).

[19] S. Daiss, S. Langenfeld, S. Welte, E. Distante, P. Thomas, L. Hartung, O. Morin, and G. Rempe. A Quantum-Logic Gate between Distant Quantum-Network Modules. *Science* **371**, 614–617 (2021).

[20] J. Dalibard and C. Cohen-Tannoudji. Laser Cooling Below the Doppler Limit by Polarization Gradients: Simple Theoretical Models. *Journal of the Optical Society of America B* **6**, 2023–2045 (1989).

[21] S. Das, A. Grankin, I. Iakoupov, E. Brion, J. Borregaard, R. Boddeda, I. Usmani, A. Ourjoumtsev, P. Grangier, and A. S. Sørensen. Photonic Controlled-Phase Gates Through Rydberg Blockade in Optical Cavities. 2015. URL: http://arxiv.org/abs/1506.04300v2.

[22] S. Das, A. Grankin, I. Iakoupov, E. Brion, J. Borregaard, R. Boddeda, I. Usmani, A. Ourjoumtsev, P. Grangier, and A. S. Sørensen. Photonic Controlled-Phase Gates Through Rydberg Blockade in Optical Cavities. *Physical Review A* **93**, 040303 (2016).

[23] K. Dieckmann, R. J. C. Spreeuw, M. Weidemüller, and J. T. M. Walraven. Two-Dimensional Magneto-Optical Trap as a Source of Slow Atoms. *Physical Review A* **58**, 3891–3895 (1998).

[24] D. P. DiVincenzo and D. Loss. Quantum Information is Physical. *Superlattices and Microstructures* **23**, 419–432 (1998).

[25] R. W. P. Drever, J. L. Hall, F. V. Kowalski, J. Hough, G. M. Ford, A. J. Munley, and H. Ward. Laser Phase and Frequency Stabilization using an Optical Resonator. *Applied Physics B* **31**, 97–105 (1983).

[26] L. M. Duan and H. J. Kimble. Scalable Photonic Quantum Computation Through Cavity-Assisted Interactions. *Physical Review Letters* **92**, 127902 (2004).

[27] Y. O. Dudin and A. Kuzmich. Strongly Interacting Rydberg Excitations of a Cold Atomic Gas. *Science* **336**, 887–889 (2012).

[28] A. E. Edmonds. Angular Momentum in Quantum Mechanics. Princeton University Press, New York (1974).

[29] M. Endres, H. Bernien, A. Keesling, H. Levine, E. R. Anschuetz, A. Krajenbrink, C. Senko, V. Vuletic, M. Greiner, and M. D. Lukin. Atom-By-Atom Assembly of Defect-Free One-Dimensional Cold Atom Arrays. *Science* **354**, 1024–1027 (2016).

[30] H. Euler and B. Kockel. Über die Streuung von Licht an Licht nach der Diracschen Theorie. *Naturwissenschaften* **23**, 246–247 (1935).

[31] A. Feizpour, M. Hallaji, G. Dmochowski, and A. M. Steinberg. Observation of the Nonlinear Phase Shift Due to Single Post-Selected Photons. *Nature Physics* **11**, 905–909 (2015).

[32] O. Firstenberg, C. S. Adams, and S. Hofferberth. Nonlinear Quantum Optics Mediated by Rydberg Interactions. *Journal of Physics B* **49**, 152003 (2016).

[33] O. Firstenberg, T. Peyronel, Q.-Y. Liang, A. V. Gorshkov, M. D. Lukin, and V. Vuletić. Attractive Photons in a Quantum Nonlinear Medium. *Nature* **502**, 71–75 (2013).

[34] M. Fleischhauer and M. D. Lukin. Quantum Memory for Photons: Dark-State Polaritons. *Physical Review A* **65**, 022314 (2002).

[35] M. Fleischhauer and M. D. Lukin. Dark-State Polaritons in Electromagnetically Induced Transparency. *Physical Review Letters* **84**, 5094 (2000).

[36] M. Fleischhauer and J. P. Marangos. Electromagnetically Induced Transparency: Optics in Coherent Media. *Reviews of Modern Physics* **77**, 633–673 (2005).

[37] T. Förster. Zwischenmolekulare Energiewanderung und Fluoreszenz. *Annalen der Physik* **437**, 55–75 (1948).

[38] T. Freegarde and C. Zimmermann. On the Design of Enhancement Cavities for Second Harmonic Generation. *Optics Communications* **199**, 435–446 (2001).

[39] I. Friedler, D. Petrosyan, M. Fleischhauer, and G. Kurizki. Long-Range Interactions and Entanglement of Slow Single-Photon Pulses. *Physical Review A* **72**, 043803 (2005).

[40] I. Fushman, D. Englund, A. Faraon, N. Stoltz, P. Petroff, and J. Vučković. Controlled Phase Shifts with a Single Quantum Dot. *Science* **320**, 769–772 (2008).

[41] T. F. Gallagher. Rydberg Atoms. Cambridge University Press, Cambridge (1994).

[42] A. Gilchrist, N. K. Langford, and M. A. Nielsen. Distance Measures to Compare Real and Ideal Quantum Processes. *Physical Review A* **71**, 062310 (2005).

[43] H. Gorniaczyk. Single Photon Transistor Mediated by Electrically Tunable Rydberg-Rydberg Interactions. PhD thesis. Universität Stuttgart, 2016.

[44] H. Gorniaczyk, C. Tresp, P. Bienias, A. Paris-Mandoki, W. Li, I. Mirgorodskiy, H. P. Büchler, I. Lesanovsky, and S. Hofferberth. Enhancement of Rydberg-Mediated Single-Photon Nonlinearities by Electrically Tuned Förster Resonances. *Nature Communications* **7**, 12480 (2016).

[45] H. Gorniaczyk, C. Tresp, J. Schmidt, H. Fedder, and S. Hofferberth. Single-Photon Transistor Mediated by Interstate Rydberg Interactions. *Physical Review Letters* **113**, 053601 (2014).

[46] A. V. Gorshkov, A. André, M. D. Lukin, and A. S. Sørensen. Photon Storage in Λ-Type Optically Dense Atomic Media. I. Cavity Model. *Physical Review A* **76**, 033804 (2007).

[47] A. V. Gorshkov, J. Otterbach, M. Fleischhauer, T. Pohl, and M. D. Lukin. Photon-Photon Interactions via Rydberg Blockade. *Physical Review Letters* **107**, 133602 (2011).

[48] A. V. Gorshkov, A. André, M. D. Lukin, and A. S. Sørensen. Photon Storage in Λ-Type Optically Dense Atomic Media. II. Free-Space Model. *Physical Review A* **76**, 033805 (2007).

[49] D. Gottesman and I. L. Chuang. Demonstrating the Viability of Universal Quantum Computation using Teleportation and Single-Qubit Operations. *Nature* **402**, 390–393 (1999).

[50] R. Grimm, M. Weidemüller, and Y. B. Ovchinnikov. Optical Dipole Traps for Neutral Atoms. *Advances in Atomic, Molecular and Optical Physics* **42**, 95–170 (2000).

[51] S. Guha, H. Krovi, C. A. Fuchs, Z. Dutton, J. A. Slater, C. Simon, and W. Tittel. Rate-loss Analysis of an Efficient Quantum Repeater Architecture. *Physical Review A* **92**, 022357 (2015).

[52] B. Hacker, S. Welte, S. Daiss, A. Shaukat, S. Ritter, L. Li, and G. Rempe. Deterministic Creation of Entangled Atom-Light Schrödinger-Cat States. *Nature Photonics* **13**, 110–115 (2019).

[53] B. Hacker, S. Welte, G. Rempe, and S. Ritter. A Photon-Photon Quantum Gate Based on a Single Atom in an Optical Resonator. *Nature*, 193–196 (2016).

[54] Y. M. Hao, G. W. Lin, K. Xia, X. M. Lin, Y. P. Niu, and S. Q. Gong. Quantum Controlled-Phase-Flip Gate between a Flying Optical Photon and a Rydberg Atomic Ensemble. *Scientific Reports* **5**, 10005 (2015).

[55] A. J. F. Hayes, A. Gilchrist, C. R. Myers, and T. C. Ralph. Utilizing Encoding in Scalable Linear Optics Quantum Computing. *Journal of Optics B* **6**, 533–541 (2004).

[56] B. He, A. V. Sharypov, J. Sheng, C. Simon, and M. Xiao. Two-Photon Dynamics in Coherent Rydberg Atomic Ensemble. *Physical Review Letters* **112**, 133606 (2014).

[57] E. Hecht and A. Zajac. Optics. Addison-Wesley, Reading (1980).

[58] F. A. Henkel. Photoionisation Detection of Single $^{87}$Rb-Atoms using Channel Electron Multipliers. PhD thesis. Ludwig-Maximilians-Universität München, 2011.

[59] G. Hernandez, J. Zhang, and Y. Zhu. Vacuum Rabi Splitting and Intracavity Dark State in a Cavity-Atom System. *Physical Review A* **76**, 053814 (2007).

[60] H. F. Hofmann, K. Kojima, S. Takeuchi, and K. Sasaki. Optimized Phase Switching Using a Single-Atom Nonlinearity. *Journal of Optics B* **5**, 218–221 (2003).

[61] B. Höltkemeier, J. Glässel, H. López-Carrera, and M. Weidemüller. A Dense Gas of Laser-Cooled Atoms for Hybrid Atom-Ion Trapping. *Applied Physics B* **123**, 51 (2017).

[62] Y.-F. Hsiao, P.-J. Tsai, H.-S. Chen, S.-X. Lin, C.-C. Hung, C.-H. Lee, Y.-H. Chen, Y.-F. Chen, I. A. Yu, and Y.-C. Chen. Highly Efficient Coherent Optical Memory Based on Electromagnetically Induced Transparency. *Physical Review Letters* **120**, 183602 (2018).

[63] J. Hu, A. Urvoy, Z. Vendeiro, V. Crépel, W. Chen, and V. Vuletić. Creation of a Bose-Condensed Gas of $^{87}$Rb by Laser Cooling. *Science* **358**, 1078–1080 (2017).

[64] L. Husel. Ein optischer Bow-Tie-Resonator für ein photonisches Quantengatter. Master's thesis. Ludwig-Maximilians-Universität München, 2019.

[65] L. Isenhower, E. Urban, X. L. Zhang, A. T. Gill, T. Henage, T. A. Johnson, T. G. Walker, and M. Saffman. Demonstration of a Neutral Atom Controlled-NOT Quantum Gate. *Physical Review Letters* **104**, 010503 (2010).

[66] D. Istrati, Y. Pilnyak, J. C. Loredo, C. Antón, N. Somaschi, P. Hilaire, H. Ollivier, M. Esmann, L. Cohen, L. Vidro, C. Millet, A. Lemaître, I. Sagnes, A. Harouri, L. Lanco, P. Senellart, and H. S. Eisenberg. Sequential Generation of Linear Cluster States from a Single Photon Emitter. *Nature Communications* **11**, 5501 (2020).

[67] D. Jaksch, J. I. Cirac, P. Zoller, S. L. Rolston, R. Côté, and M. D. Lukin. Fast Quantum Gates for Neutral Atoms. *Physical Review Letters* **85**, 2208–2211 (2000).

[68] S. D. Jenkins, T. Zhang, and T. A. B. Kennedy. Motional Dephasing of Atomic Clock Spin Waves in an Optical Lattice. *Journal of Physics B* **45**, 124005 (2012).

[69] N. Jia, N. Schine, A. Georgakopoulos, A. Ryou, L. W. Clark, A. Sommer, and J. Simon. A Strongly Interacting Polaritonic Quantum Dot. *Nature Physics* **14**, 550–554 (2018).

[70] N. Jia, N. Schine, A. Georgakopoulos, A. Ryou, A. Sommer, and J. Simon. Photons and Polaritons in a Broken-Time-Reversal Nonplanar Resonator. *Physical Review A* **97**, 013802 (2018).

[71] R. Jozsa. Fidelity for Mixed Quantum States. *Journal of Modern Optics* **41**, 2315–2323 (1994).

[72] M. Kasevich and S. Chu. Laser Cooling Below a Photon Recoil with Three-Level Atoms. *Physical Review Letters* **69**, 1741–1744 (1992).

[73] M. Khazali, K. Heshami, and C. Simon. Photon-Photon Gate via the Interaction between Two Collective Rydberg Excitations. *Physical Review A* **91**, 030301 (2015).

[74] K. Kieling, J. L. O'Brien, and J. Eisert. On Photonic Controlled Phase Gates. *New Journal of Physics* **12**, 013003 (2010).

[75] J.-H. Kim, S. Aghaeimeibodi, J. Carolan, D. Englund, and E. Waks. Hybrid Integration Methods for On-Chip Quantum Photonics. *Optica* **7**, 291–308 (2020).

[76] H. J. Kimble. The Quantum Internet. *Nature* **453**, 1023–1030 (2008).

[77] K. S. Kleinbach. Ions and Electrons Interacting with Ultracold Atoms. PhD thesis. Universität Stuttgart, 2018.

[78] E. Knill, R. Laflamme, and G. J. Milburn. A Scheme for Efficient Quantum Computation with Linear Optics. *Nature* **409**, 46–52 (2001).

[79] P. Kok, W. J. Munro, K. Nemoto, T. C. Ralph, J. P. Dowling, and G. J. Milburn. Linear Optical Quantum Computing with Photonic Qubits. *Reviews of Modern Physics* **79**, 135–174 (2007).

[80] T. Kraemer, J. Herbig, M. Mark, T. Weber, C. Chin, H.-C. Nägerl, and R. Grimm. Optimized Production of a Cesium Bose-Einstein Condensate. *Applied Physics B* **79**, 1013–1019 (2004).

[81] S. J. M. Kuppens, K. L. Corwin, K. W. Miller, T. E. Chupp, and C. E. Wieman. Loading an Optical Dipole Trap. *Physical Review A* **62**, 013406 (2000).

[82] O. Lahad and O. Firstenberg. Induced Cavities for Photonic Quantum Gates. *Physical Review Letters* **119**, 113601 (2017).

[83] R. H. Landau, M. J. Páez, and C. C. Bordeianu. Computational Physics: Problem Solving with Computers. Wiley-VCH, Weinheim (2007).

[84] H. J. Lee, C. S. Adams, M. Kasevich, and S. Chu. Raman Cooling of Atoms in an Optical Dipole Trap. *Physical Review Letters* **76**, 2658–2661 (1996).

[85] H. Levine, A. Keesling, A. Omran, H. Bernien, S. Schwartz, A. S. Zibrov, M. Endres, M. Greiner, V. Vuleti ć, and M. D. Lukin. High-Fidelity Control and Entanglement of Rydberg-Atom Qubits. *Physical Review Letters* **121**, 123603 (2018).

[86] J.-P. Li, X. Gu, J. Qin, D. Wu, X. You, H. Wang, C. Schneider, S. Höfling, Y.-H. Huo, C.-Y. Lu, N.-L. Liu, L. Li, and J.-W. Pan. Heralded Nondestructive Quantum Entangling Gate with Single-Photon Sources. *Physical Review Letters* **126**, 140501 (2021).

[87] W. Li, I. Mourachko, M. W. Noel, and T. F. Gallagher. Millimeter-Wave Spectroscopy of Cold Rb Rydberg Atoms in a Magneto-Optical Trap: Quantum Defects of the ns, np, and nd Series. *Physical Review A* **67**, 052502 (2003).

[88] Z. Y. Liu, Y. H. Chen, Y. C. Chen, H. Y. Lo, P. J. Tsai, I. A. Yu, Y. C. Chen, and Y. F. Chen. Large Cross-Phase Modulations at the Few-Photon Level. *Physical Review Letters* **117**, 203601 (2016).

[89] H. Y. Lo, Y. C. Chen, P. C. Su, H. C. Chen, J. X. Chen, Y. C. Chen, I. A. Yu, and Y. F. Chen. Electromagnetically-Induced-Transparency-Based Cross-Phase-Modulation at Attojoule Levels. *Physical Review A* **83**, 041804(R) (2011).

[90] C.-Y. Lu, X.-Q. Zhou, O. Gühne, W.-B. Gao, J. Zhang, Z.-S. Yuan, A. Goebel, T. Yang, and J.-W. Pan. Experimental Entanglement of Six Photons in Graph States. *Nature Physics* **3**, 91–95 (2007).

[91] M. D. Lukin, M. Fleischhauer, M. O. Scully, and V. L. Velichansky. Intracavity Electromagnetically Induced Transparency. *Optics Letters* **23**, 295–297 (1998).

[92] P. Lunt. Design and Construction of a New Ultracold Ytterbium Experiment for Rydberg Physics. Master's thesis. University of Southern Denmark, 2019.

[93] N. Lütkenhaus, J. Calsamiglia, and K.-A. Suominen. Bell Measurements for Teleportation. *Physical Review A* **59**, 3295–3300 (1999).

[94] A. Marte. Feshbach-Resonanzen bei Stößen ultrakalter Rubidiumatome. PhD thesis. Technische Universität München, 2003.

[95] N. Matsuda, R. Shimizu, Y. Mitsumori, H. Kosaka, and K. Edamatsu. Observation of Optical-Fibre Kerr Nonlinearity at the Single-Photon Level. *Nature Photonics* **3**, 95–98 (2009).

[96] H. Metcalf and P. van der Straten. Laser Cooling and Trapping. Springer, Berlin (1999).

[97] G. J. Milburn. Quantum Optical Fredkin Gate. *Physical Review Letters* **62**, 2124–2127 (1989).

[98] I. Mirgorodskiy, F. Christaller, C. Braun, A. Paris-Mandoki, C. Tresp, and S. Hofferberth. Electromagnetically Induced Transparency of Ultra-Long-Range Rydberg Molecules. *Physical Review A* **96**, 011402 (2017).

[99] T. Monz, P. Schindler, J. T. Barreiro, M. Chwalla, D. Nigg, W. A. Coish, M. Harlander, W. Hänsel, M. Hennrich, and R. Blatt. 14-Qubit Entanglement: Creation and Coherence. *Physical Review Letters* **106**, 130506 (2011).

[100] M. Moreno-Cardoner, D. Goncalves, and D. E. Chang. Quantum Nonlinear Optics Based on Two-Dimensional Rydberg Atom Arrays. *Physical Review Letters* **127**, 263602 (2021).

[101] F. Motzoi and K. Mølmer. Precise Single-Qubit Control of the Reflection Phase of a Photon Mediated by a Strongly-Coupled Ancilla–Cavity System. *New Journal of Physics* **20**, 053029 (2018).

[102] C. R. Murray and T. Pohl. Coherent Photon Manipulation in Interacting Atomic Ensembles. *Physical Review X* **7**, 031007 (2017).

[103] M. A. Nielsen. Optical Quantum Computation Using Cluster States. *Physical Review Letters* **93**, 040503 (2004).

[104] M. A. Nielsen and I. L. Chuang. Quantum Computation and Quantum Information. Cambridge University Press, Cambridge (2010).

[105] J. L. O'Brien, G. J. Pryde, A. Gilchrist, D. F. V. James, N. K. Langford, T. C. Ralph, and A. G. White. Quantum Process Tomography of a Controlled-NOT Gate. *Physical Review Letters* **93**, 080502 (2004).

[106] J. L. O'Brien, G. J. Pryde, A. G. White, T. C. Ralph, and D. Branning. Demonstration of an All-Optical Quantum Controlled-NOT Gate. *Nature* **426**, 264–267 (2003).

[107] J. L. O'Brien. Optical Quantum Computing. *Science* **318**, 1567–1570 (2007).

[108] J. Otterbach, M. Moos, D. Muth, and M. Fleischhauer. Wigner Crystallization of Single Photons in Cold Rydberg Ensembles. *Physical Review Letters* **111**, 113001 (2013).

[109] D. Paredes-Barato and C. S. Adams. All-Optical Quantum Information Processing Using Rydberg Gates. *Physical Review Letters* **112**, 040501 (2014).

[110] A. Paris-Mandoki, H. Gorniaczyk, C. Tresp, I. Mirgorodskiy, and S. Hofferberth. Tailoring Rydberg Interactions via Förster Resonances: State Combinations, Hopping and Angular Dependence. *Journal of Physics B* **49**, 164001 (2016).

[111] T. Peyronel, O. Firstenberg, Q.-Y. Liang, S. Hofferberth, A. V. Gorshkov, T. Pohl, M. D. Lukin, and V. Vuletić. Quantum Nonlinear Optics with Single Photons Enabled by Strongly Interacting Atoms. *Nature* **488**, 57–60 (2012).

[112] A. Politi, M. J. Cryan, J. G. Rarity, S. Yu, and J. L. O'Brien. Silica-on-Silicon Waveguide Quantum Circuits. *Science* **320**, 646–649 (2008).

[113] J. F. Poyatos, J. I. Cirac, and P. Zoller. Complete Characterization of a Quantum Process: The Two-Bit Quantum Gate. *Physical Review Letters* **78**, 390–393 (1997).

[114] J. D. Pritchard, D. Maxwell, A. Gauguet, K. J. Weatherill, M. P. A. Jones, and C. S. Adams. Cooperative Atom-Light Interaction in a Blockaded Rydberg Ensemble. *Physical Review Letters* **105**, 193603 (2010).

[115] X. Qiang, X. Zhou, J. Wang, C. M. Wilkes, T. Loke, S. O'Gara, L. Kling, G. D. Marshall, R. Santagati, T. C. Ralph, J. B. Wang, J. L. O'Brien, M. G. Thompson, and J. C. F. Matthews. Large-Scale Silicon Quantum Photonics Implementing Arbitrary Two-Qubit Processing. *Nature Photonics* **12**, 534–539 (2018).

[116] T. C. Ralph, A. Gilchrist, G. J. Milburn, W. J. Munro, and S. Glancy. Quantum Computation with Optical Coherent States. *Physical Review A* **68**, 042319 (2003).

[117] T. C. Ralph, A. J. F. Hayes, and A. Gilchrist. Loss-Tolerant Optical Qubits. *Physical Review Letters* **95**, 100501 (2005).

[118] R. Raussendorf and H. J. Briegel. A One-Way Quantum Computer. *Physical Review Letters* **86**, 5188–5191 (2001).

[119] S. Ravets, H. Labuhn, D. Barredo, L. Béguin, T. Lahaye, and A. Browaeys. Coherent Dipole-Dipole Coupling between Two Single Rydberg Atoms at an Electrically-Tuned Förster Resonance. *Nature Physics* **10**, 914–917 (2014).

[120] A. Reinhard, T. C. Liebisch, B. Knuffman, and G. Raithel. Level Shifts of Rubidium Rydberg States Due to Binary Interactions. *Physical Review A* **75**, 032712 (2007).

[121] A. Reiserer and G. Rempe. Cavity-Based Quantum Networks with Single Atoms and Optical Photons. *Reviews of Modern Physics* **87**, 1379–1418 (2015).

[122] K. Reuer, J.-C. Besse, L. Wernli, P. Magnard, P. Kurpiers, G. J. Norris, A. Wallraff, and C. Eichler. Realization of a Universal Quantum Gate Set for Itinerant Microwave Photons. *Physical Review X* **12**, 011008 (2022).

[123] M. Riebe, K. Kim, P. Schindler, T. Monz, P. O. Schmidt, T. K. Körber, W. Hänsel, H. Häffner, C. F. Roos, and R. Blatt. Process Tomography of Ion Trap Quantum Gates. *Physical Review Letters* **97**, 220407 (2006).

[124] S. Ritter, C. Nölleke, C. Hahn, A. Reiserer, A. Neuzner, M. Uphoff, M. Mücke, E. Figueroa, J. Bochmann, and G. Rempe. An Elementary Quantum Network of Single Atoms in Optical Cavities. *Nature* **484**, 195–200 (2012).

[125] E. Robertson, N. Šibalić, R. Potvliege, and M. Jones. ARC 3.0: An Expanded Python Toolbox for Atomic Physics Calculations. *Computer Physics Communications* **261**, 107814 (2021).

[126] B. Röhr. Ein ultrakaltes atomares Gas in einem optischen Ringresonator. Master's thesis. Technische Universität München, 2021.

[127] C. A. Sackett, D. Kielpinski, B. E. King, C. Langer, V. Meyer, C. J. Myatt, M. Rowe, Q. A. Turchette, W. M. Itano, D. J. Wineland, and C. Monroe. Experimental Entanglement of Four Particles. *Nature* **404**, 256–259 (2000).

[128] M. Saffman, T. Walker, and K. Mølmer. Quantum Information with Rydberg Atoms. *Reviews of Modern Physics* **82**, 2313–2363 (2010).

[129] T. A. Savard, K. M. O'Hara, and J. E. Thomas. Laser-Noise-Induced Heating in Far-Off Resonance Optical Traps. *Physical Review A* **56**, R1095–R1098 (1997).

[130] P. Schauß, J. Zeiher, T. Fukuhara, S. Hild, M. Cheneau, T. Macrì, T. Pohl, I. Bloch, and C. Gross. Crystallization in Ising Quantum Magnets. *Science* **347**, 1455–1458 (2015).

[131] F. Schmid, J. Weitenberg, T. W. Hänsch, T. Udem, and A. Ozawa. Simple Phase Noise Measurement Scheme for Cavity-Stabilized Laser Systems. *Optics Letters* **44**, 2709–2712 (2019).

[132] S. Schmidt-Eberle. Ein Photon-Photon-Quantengatter basierend auf Rydberg-Rydberg-Wechselwirkung. PhD thesis. Technische Universität München, 2022.

[133] S. Schmidt-Eberle, T. Stolz, G. Rempe, and S. Dürr. Dark-Time Decay of the Retrieval Efficiency of Light Stored as a Rydberg Excitation in a Noninteracting Ultracold Gas. *Physical Review A* **101**, 013421 (2020).

[134] J. Schoser, A. Batär, R. Löw, V. Schweikhard, A. Grabowski, Y. B. Ovchinnikov, and T. Pfau. Intense Source of Cold Rb Atoms from a Pure Two-Dimensional Magneto-Optical Trap. *Physical Review A* **66**, 023410 (2002).

[135] J. Schuster. Stoßlawinen in einem Bose-Einstein-Kondensat. PhD thesis. Universität Konstanz, 2002.

[136] I. Schwartz, D. Cogan, E. R. Schmidgall, Y. Don, L. Gantz, O. Kenneth, N. H. Lindner, and D. Gershoni. Deterministic Generation of a Cluster State of Entangled Photons. *Science* **354**, 434–437 (2016).

[137] S. Sevinçli, N. Henkel, C. Ates, and T. Pohl. Nonlocal Nonlinear Optics in Cold Rydberg Gases. *Physical Review Letters* **107**, 153001 (2011).

[138] B. W. Shiau, M. C. Wu, C. C. Lin, and Y. C. Chen. Low-Light-Level Cross-Phase Modulation with Double Slow Light Pulses. *Physical Review Letters* **106**, 193006 (2011).

[139] I. Shomroni, S. Rosenblum, Y. Lovsky, O. Bechler, G. Guendelman, and B. Dayan. All-Optical Routing of Single Photons by a One-Atom Switch Controlled by a Single Photon. *Science* **345**, 903–906 (2014).

[140] P. Shor. Polynomial-Time Algorithms for Prime Factorization and Discrete Logarithms on a Quantum Computer. *SIAM Journal on Computing* **26**, 1484–1509 (1997).

[141] A. E. Siegman. Lasers. University Science Books, Sausalito, California (1986).

[142] R. Simon and N. Mukunda. Minimal Three-Component SU(2) Gadget for Polarization Optics. *Physics Letters A* **143**, 165–169 (1990).

[143] T. Stolz, H. Hegels, M. Winter, B. Röhr, Y.-F. Hsiao, L. Husel, G. Rempe, and S. Dürr. Quantum-Logic Gate between Two Optical Photons with an Average Efficiency above 40%. *Physical Review X* **12**, 021035 (2022).

[144] K. Takase, J.-i. Yoshikawa, W. Asavanant, M. Endo, and A. Furusawa. Generation of Optical Schrödinger Cat States by Generalized Photon Subtraction. *Physical Review A* **103**, 013710 (2021).

[145] M. Tavis and F. W. Cummings. Exact Solution for an $N$-Molecule—Radiation-Field Hamiltonian. *Physical Review* **170**, 379–384 (1968).

[146] H. R. Telle. Absolute Measurement of Optical Frequencies. Wiley, New York (1996).

[147] P. Thomas, L. Ruscio, O. Morin, and G. Rempe. Efficient Generation of Entangled Multiphoton Graph States from a Single Atom. *Nature* **608**, 677–681 (2022).

[148] J. D. Thompson, T. L. Nicholson, Q.-Y. Liang, S. H. Cantu, A. V. Venkatramani, S. Choi, I. A. Fedorov, D. Viscor, T. Pohl, M. D. Lukin, and V. Vuletić. Symmetry-Protected Collisions between Strongly Interacting Photons. *Nature* **542**, 206–209 (2017).

[149] D. Tiarks. Quantenbits in Ensembles ultrakalter Rydberg-Atome. PhD thesis. Technische Universität München, 2019.

[150] D. Tiarks, S. Baur, K. Schneider, S. Dürr, and G. Rempe. Single-Photon Transistor Using a Förster Resonance. *Physical Review Letters* **113**, 053602 (2014).

[151] D. Tiarks, S. Schmidt-Eberle, T. Stolz, G. Rempe, and S. Dürr. A Photon-Photon Quantum Gate Based on Rydberg Interactions. *Nature Physics* **15**, 124–126 (2019).

[152] D. Tiarks, S. Schmidt, G. Rempe, and S. Dürr. Optical $\pi$ Phase Shift Created with a Single-Photon Pulse. *Science Advances* **2**, e1600036 (2016).

[153] T. G. Tiecke, J. D. Thompson, N. P. de Leon, L. R. Liu, V. Vuletić, and M. D. Lukin. Nanophotonic Quantum Phase Switch with a Single Atom. *Nature* **508**, 241–244 (2014).

[154] T. Tilma and E. C. G. Sudarshan. Generalized Euler Angle Parametrization for $SU(N)$. *Journal of Physics A* **35**, 10467–10501 (2002).

[155] D. Tong, S. M. Farooqi, J. Stanojevic, S. Krishnan, Y. P. Zhang, R. Côté, E. E. Eyler, and P. L. Gould. Local Blockade of Rydberg Excitation in an Ultracold Gas. *Physical Review Letters* **93**, 063001 (2004).

[156] A. K. Tuchman, R. Long, G. Vrijsen, J. Boudet, J. Lee, and M. A. Kasevich. Normal-Mode Splitting with Large Collective Cooperativity. *Physical Review A* **74**, 053821 (2006).

[157] Q. A. Turchette, C. J. Hood, W. Lange, H. Mabuchi, and H. J. Kimble. Measurement of Conditional Phase Shifts for Quantum Logic. *Physical Review Letters* **75**, 4710–4713 (1995).

[158] C. Turnbaugh, J. J. Axelrod, S. L. Campbell, J. Y. Dioquino, P. N. Petrov, J. Remis, O. Schwartz, Z. Yu, Y. Cheng, R. M. Glaeser, and H. Mueller. High-Power Near-Concentric Fabry–Perot Cavity for Phase Contrast Electron Microscopy. *Review of Scientific Instruments* **92**, 053005 (2021).

[159] A. Urvoy, Z. Vendeiro, J. Ramette, A. Adiyatullin, and V. Vuleti ć. Direct Laser Cooling to Bose-Einstein Condensation in a Dipole Trap. *Physical Review Letters* **122**, 203202 (2019).

[160] J. Vaneecloo, S. Garcia, and A. Ourjoumtsev. Intracavity Rydberg Superatom for Optical Quantum Engineering: Coherent Control, Single-Shot Detection, and Optical $\pi$ Phase Shift. *Physical Review X* **12**, 021034 (2022).

[161] J. Volz, M. Scheucher, C. Junge, and A. Rauschenbeutel. Nonlinear $\pi$ Phase Shift for Single Fibre-Guided Photons Interacting with a Single Resonator-Enhanced Atom. *Nature Photonics* **8**, 965–970 (2014).

[162] A. C. J. Wade, M. Mattioli, and K. Mølmer. Single-Atom Single-Photon Coupling Facilitated by Atomic-Ensemble Dark-State Mechanisms. *Physical Review A* **94**, 053830 (2016).

[163] T. G. Walker and M. Saffman. Consequences of Zeeman Degeneracy for the Van der Waals Blockade between Rydberg atoms. *Physical Review A* **77**, 032723 (2008).

[164] X.-L. Wang, L.-K. Chen, W. Li, H.-L. Huang, C. Liu, C. Chen, Y.-H. Luo, Z.-E. Su, D. Wu, Z.-D. Li, H. Lu, Y. Hu, X. Jiang, C.-Z. Peng, L. Li, N.-L. Liu, Y.-A. Chen, C.-Y. Lu, and J.-W. Pan. Experimental Ten-Photon Entanglement. *Physical Review Letters* **117**, 210502 (2016).

[165] S. Wehner, D. Elkouss, and R. Hanson. Quantum Internet: A Vision for the Road Ahead. *Science* **362**, eaam9288 (2018).

[166] S. Weyers, E. Aucouturier, C. Valentin, and N. Dimarcq. A Continuous Beam of Cold Cesium Atoms Extracted from a Two-Dimensional Magneto-Optical Trap. *Optics Communications* **143**, 30–34 (1997).

[167] T. Wilk, A. Gaëtan, C. Evellin, J. Wolters, Y. Miroshnychenko, P. Grangier, and A. Browaeys. Entanglement of Two Individual Neutral Atoms Using Rydberg Blockade. *Physical Review Letters* **104**, 010502 (2010).

[168] H. Wu, J. Gea-Banacloche, and M. Xiao. Observation of Intracavity Electromagnetically Induced Transparency and Polariton Resonances in a Doppler-Broadened Medium. *Physical Review Letters* **100**, 173602 (2008).

[169] Y. Yamamoto, M. Kitagawa, and K. Igeta. In: *Proceedings of the 3rd Asia-Pacific Physics Conference*. Ed. by Y. W. Chan, A. F. Leung, C. N. Yang, and K. Young. World Scientific, Singapore (1988), pp. 779–799.

[170] C.-W. Yang, Y. Yu, J. Li, B. Jing, X.-H. Bao, and J.-W. Pan. Sequential Generation of Multiphoton Entanglement with a Rydberg Superatom. 2021. URL: https://arxiv.org/abs/2112.09447.

[171] X.-C. Yao, T.-X. Wang, H.-Z. Chen, W.-B. Gao, A. G. Fowler, R. Raussendorf, Z.-B. Chen, N.-L. Liu, C.-Y. Lu, Y.-J. Deng, Y.-A. Chen, and J.-W. Pan. Experimental Demonstration of Topological Error Correction. *Nature* **482**, 489–494 (2012).

[172] N. Yoran and B. Reznik. Deterministic Linear Optics Quantum Computation with Single Photon Qubits. *Physical Review Letters* **91**, 037903 (2003).

[173] B. Zhao, Y.-A. Chen, X.-H. Bao, T. Strassel, C.-S. Chuu, X.-M. Jin, J. Schmiedmayer, Z.-S. Yuan, S. Chen, and J.-W. Pan. A Millisecond Quantum Memory for Scalable Quantum Networks. *Nature Physics* **5**, 95–99 (2009).

[174] H.-S. Zhong, Y. Li, W. Li, L.-C. Peng, Z.-E. Su, Y. Hu, Y.-M. He, X. Ding, W. Zhang, H. Li, L. Zhang, Z. Wang, L. You, X.-L. Wang, X. Jiang, L. Li, Y.-A. Chen, N.-L. Liu, C.-Y. Lu, and J.-W. Pan. 12-Photon Entanglement and Scalable Scattershot Boson Sampling with Optimal Entangled-Photon Pairs from Parametric Down-Conversion. *Physical Review Letters* **121**, 250505 (2018).

[175] H.-S. Zhong, H. Wang, Y.-H. Deng, M.-C. Chen, L.-C. Peng, Y.-H. Luo, J. Qin, D. Wu, X. Ding, Y. Hu, P. Hu, X.-Y. Yang, W.-J. Zhang, H. Li, Y. Li, X. Jiang, L. Gan, G. Yang, L. You, Z. Wang, L. Li, N.-L. Liu, C.-Y. Lu, and J.-W. Pan. Quantum Computational Advantage using Photons. *Science* **370**, 1460–1463 (2020).

[176] M. L. Zimmerman, M. G. Littman, M. M. Kash, and D. Kleppner. Stark Structure of the Rydberg States of Alkali-Metal Atoms. *Physical Review A* **20**, 2251–2275 (1979).

# Danksagung

Zuletzt möchte ich einigen Menschen danken.

Mein aufrichtiger Dank gilt Gerhard Rempe für die Möglichkeit zur Promotion in seiner Abteilung. Du hast mich in vielen wichtigen Belangen unterstützt und mir die Freiheit gegeben, dieses Projekt nach meinen Vorstellungen umzusetzen. Unsere Gespräche haben mir viele wertvolle Denkanstöße geliefert und mich dazu motiviert, bis an die Grenzen des Machbaren zu gehen. Ohne die von dir kultivierten Rahmenbedingungen in deiner Abteilung wäre mein Vorhaben so nicht möglich gewesen.

Von Stephan Dürr habe ich ein Maß an Unterstützung erhalten, für das ich mich nur unzureichend bedanken kann. Während meiner Zeit am MPQ habe ich unglaublich viel von dir gelernt. Für einen Besuch in deinem fast immer geöffneten Büro gab es diverse Anlässe: didaktisch hochwertige Spontantutorien in theoretischer Physik, erheiternde Fakten und Anekdoten, Strategiebesprechungen, konstruktives Feedback zu Texten und Präsentationen, sowie die nicht zu unterschätzende „allmähliche Verfertigung der Gedanken beim Reden“ nach Heinrich von Kleist. Besonders dankbar bin ich dir für deinen Rückhalt und deinen Einsatz für das Gelingen dieser Arbeit.

Ein ganz herzliches Dankeschön geht an Stephan Ritter für die Bereitschaft, diese Arbeit als Mentor zu begleiten. Bei unseren halbjährlichen Treffen in diversen Münchner Lokalen und Biergärten warst du immer ein super Gesprächspartner und hattest einige gute Tipps.

Meinem Vorgängerdoktoranden Daniel Tiarks danke ich für die Aufnahme eines gewissen Masterstudenten bei den „BEClern“ im Jahr 2014 und für die gute Zusammenarbeit in den darauffolgenden Jahren. Du hast mir viel Wichtiges über einen komplexen Laboraufbau beigebracht und das Experiment in bester Vollgas-Manier vorangetrieben, was für mich ein hilfreiches Beispiel war.

Ganz herzlich möchte ich mich auch bei meinem direkten Vorgänger und langjährigen Mitstreiter Steffen Schmidt-Eberle für die freundschaftliche Zusammenarbeit bedanken. Obwohl ein in die Jahre gekommenes Experiment alles daran gesetzt hat uns den Spaß zu verderben, haben wir unermüdlich Vacseal auf undichte Vakuumfenster gepinselt, zweckfreie Kabel entfernt und wackelig montierte Optiken festgezogen. Mir hat diese Zeit großen Spaß gemacht, denn du hast viel gute Laune verbreitet und dich am Ende erfolgreich zur Promotion gekämpft. Natürlich dürfen unsere legendären Kickerduelle gegen die QGates und die Moleküle hier nicht unerwähnt bleiben. Damit sie weiter gegen uns spielen, haben wir sie auch manchmal gewinnen lassen, was sie dank deiner meisterlich vorgespielten Verärgerung nie gemerkt haben.

Großen Spaß hat mir die Planung des neuen Experiments und das Design und Testen verschiedener Resonatoren zusammen mit Lukas Husel gemacht. In der Aufbauphase hat Bianca Röhr ein super Abbildungssystem beigesteuert und mich im Labor unterstützt. Danke euch beiden für die gute Zeit und die tolle Zusammenarbeit! Ya-Fen Hsiao danke ich herzlich für die Hilfe beim Aufbau der Vakuumkammer und der magneto-optischen Fallen. In die heiße Phase des neuen Experiments ging es zusammen mit Hendrik Hegels und Max Winter. Ihr habt es geschafft einen hochkomplizierten Aufbau erstaunlich schnell in den Griff zu bekommen und sogar noch wesentliche Verbesserungen in Rekordzeit hinzugefügt. Ohne euch und euren Einsatz wären die Ergebnisse nicht so gut geworden und es hätte nicht halb so viel Spaß gemacht. Vielen Dank dafür, ihr wart beide wirklich super!

Den Technikern unserer Abteilung Florian Furchtsam, Johannes Siegl, Tobias Urban und Thomas Wiesmeier, sowie dem Team der Zentralwerkstatt danke ich für die vielen guten Ideen und die schnelle, unkomplizierte Hilfe bei meinen diversen Anfragen. Besonders hervorheben möchte ich Tobis ausgezeichnete Arbeit beim mechanischen Design des neuen Experiments und seine unschätzbare Unterstützung beim Aufbau des Vakuumsystems. Außerdem danke ich unserer Abteilungssekretärin Iris Anneser für die nette Hilfe bei zahlreichen Anliegen.

Ein großes Dankeschön geht an Thomas Pohl und seine Theoriegruppe in Aarhus, insbesondere an Valentin Walther und Callum Murray, für ihre Gastfreundschaft im März 2018 und für den theoretischen Input als „Initialzündung“ zu meiner Arbeit. Für besonders hilfreiche Gespräche und Tipps zu wissenschaftlichen oder technischen Themen im Zusammenhang mit dieser Arbeit bedanke ich mich außerdem bei Alban Urvoy, Andreas Reiserer, Dominik Niemietz, Emanuele Distante, Fabian Schmid, Florian Meinert, Jonathan Simon, Lothar Maisenbacher, Martin Zeppenfeld, Manuel Koller, Nathan Schine, Olivier Morin, Pau Farrera, Philip Thomas, Richard Schmidt, Robert Löw, Severin Daiß, Stefan Ernst, Stephan Welte, Thomas Dieterle und Tilman Pfau. Der Studienstiftung des deutschen Volkes danke ich für das Promotionsstipendium.

Darüber hinaus hat diese Arbeit auch erheblich von dem Umfeld profitiert, in dem sie entstehen durfte. Den Teams der anderen Experimente unserer Abteilung danke ich für den offenen Austausch und die nette und lockere Atmosphäre. Gerne erinnere ich mich an zahlreiche lustige Momente im Nachbarbüro, am Kickertisch, auf Konferenzen und bei verschiedenen Feiern.

Ganz zuletzt gilt mein besonderer Dank meiner Familie. Isabella, ich danke dir von Herzen für all deine Unterstützung. Du hast sämtliche Höhen und Tiefen meiner Doktorarbeit mit mir durchlebt und warst gerade in den schwierigen Phasen immer für mich da. Vielen lieben Dank meinen Eltern Marlies und Eugen für alles. Und schließlich danke ich Felix. Du hast das Zusammenschreiben persönlich beaufsichtigt und mich auf deine charmante Art darauf aufmerksam gemacht, dass manches zu Ende gebracht werden muss, damit anderes neu beginnen kann.